

edited by Aleksander Gurlo

**Maria Colmenares**

# Ordered Mesoporous Silica COK-12: Mesoscale Tailoring, Upscaling, Continuous Synthesis and Application in the Oxidative Coupling of Methane





Maria Colmenares

**Ordered Mesoporous Silica COK-12: Mesoscale Tailoring, Upscaling, Continuous Synthesis and Application in the Oxidative Coupling of Methane**

The scientific series *Advanced Ceramic Materials* is edited by:  
Prof. Dr. Aleksander Gurlo.

Maria Colmenares

**Ordered Mesoporous Silica COK-12: Mesoscale Tailoring, Upscaling, Continuous Synthesis and Application in the Oxidative Coupling of Methane**

**Bibliographic information published by the Deutsche Nationalbibliothek**

The Deutsche Nationalbibliothek lists this publication in the Deutsche Nationalbibliografie; detailed bibliographic data are available on the Internet at <http://dnb.dnb.de>.

**Universitätsverlag der TU Berlin, 2018**

<http://verlag.tu-berlin.de>

Fasanenstr. 88, 10623 Berlin  
Tel.: +49 (0)30 314 76131 / Fax: -76133  
E-Mail: [publikationen@ub.tu-berlin.de](mailto:publikationen@ub.tu-berlin.de)

Zugl.: Berlin, Techn. Univ., Diss., 2016  
Gutachter: Prof. Dr. Aleksander Gurlo  
Gutachter: Prof. Dr. Arne Thomas  
Gutachter: Prof. Dr. Reyes Mallada (University of Zaragoza, Spain)  
Die Arbeit wurde am 15. Dezember 2016 an der Fakultät III unter  
Vorsitz von Prof. Dr. Aleksander Gurlo erfolgreich verteidigt.

The manuscript is protected by copyright.

Cover image:  
David Karl | Segerkegel | 2017

Print: Pro BUSINESS  
Layout/Typesetting: Maria Colmenares

**ISBN 978-3-7983-2988-1 (print)**  
**ISBN 978-3-7983-2989-8 (online)**

**ISSN 2569-8303 (print)**  
**ISSN 2569-8338 (online)**

Published online on the institutional repository of the  
Technische Universität Berlin:  
DOI [10.14279/depositonce-6744](https://doi.org/10.14279/depositonce-6744)  
<http://dx.doi.org/10.14279/depositonce-6744>

Dedicated to my parents,  
Gerardo and Georgina

Dedicado a mis padres,  
Gerardo y Georgina



# Acknowledgements

I would like to express my deepest gratitude to those who contributed to the completion of this thesis, in one way or another.

To the Chair of Advanced Ceramics: Prof. Dr. Aleksander Gurlo, Ulla, Franzi, Oliver, David, Xifan, Maged, Lukas, Delf, Sara, Artur, Kai, Harald, Peter, Heinz, Anne-Claude and my students Shirin and Oscar. I could not have asked for a better group to work with. I hope my time here has had a positive impact on your work and lives, as you have had on mine. Thank you all so much.

To the Functional Materials Group: Prof. Dr. Arne Thomas, Caren, Maria, Christina and Johannes. Thank you for all the fruitful discussions and endless sample characterization.

To the Chemical Reaction Engineering Group: Prof. Dr. Reinhard Schomäcker, Samira and Mahmut and to BasCat: Dr. Frank Rosowski and Dr. Michael Geske. Thank you for the interesting conversations and catalytic testing.

To UniCat and the BIG-NSE: Dr. Jean-Phillipe Lonjaret, Nina, Johanna, Inés, Tomos, Matthias, Daniel, Paddy, Moritz, Johannes, Jonas, and the rest of my batchmates and friends.

To my German family: Laura, Manu, Rio, Maria and beautiful Rita. Your support during my time in Germany has been beyond valuable and I am forever grateful and proud to be a part of the family.

To my urban family: Laura Carolina, Seti, Andreas, Leo, Javier and my dear Albert. Without your support, this endeavor would have been impossible. Thank you a million times.

To my Venezuelan family: Mami, Papi, Vero, Anto, Alma, Loren, Chris, Mamiña, Marta, Maru, Mari, Virginia, Carla, Elisa, Flor,

Victoria, Carla Inés, Cleiba, Sam and the rest of the enormous lot. You are my roots, thank you for keeping me grounded and optimistic. This is for you.

To my love Michael, what do you call them? Oh, feet. Thank you for your love, support and understanding, in the good and not so good times. And for all the pizza.

To all of you, this achievement is as much yours as it is mine. Thank you.

# Abstract

Ordered mesoporous silica (OMS) materials are a family of silica nanomaterials with pores ranging in size from 2 to 50 nm which are arranged periodically within the silica matrix. They have expanding applications in various fields of research, such as drug delivery, adsorption, separation and catalysis. COK-12 is an OMS produced by the soft-templating method, using the block copolymer P123 as a structure-directing agent. The synthesis takes place at room temperature under mild reaction conditions. In comparison with the most widely known OMS, the synthesis of COK-12 is more time efficient, inexpensive and environmentally friendly, yielding a material analogous to the well-known SBA-15.

This thesis encompasses investigations regarding the production of the ordered mesoporous silica material (OMS) known as COK-12, in terms of upscaling of the synthesis and tailoring of the size and shape of its characteristic hexagonal pore structure. Batch upscaling of the synthesis yielded a material with nearly identical properties to that of the original COK-12. Upscaling of the COK-12 synthesis was also studied in continuous mode. The installation and operation of a continuous COK-12 production unit was carried out with the aim to determine the possibility of large-scale production of COK-12 with consistent material properties. COK-12 was produced in continuous mode by varying the time of aging of the COK-12 slurry and the flow rate of the feed streams, yielding materials with properties nearly identical to those of the original COK-12.

COK-12 was used as a support for the  $\text{Na}_2\text{WO}_4\text{-Mn/SiO}_2$  catalyst for the oxidative coupling of methane reaction in various forms (powder, granular produced by pressing and monolithic), showing promising results comparable to the enhanced activity of the catalyst supported on the SBA-15. The advantage of using COK-12 over other OMS materials is that the facile nature of COK-12 synthesis makes it a viable candidate for industrial

production of the  $\text{Na}_2\text{WO}_4\text{-Mn/SiO}_2$  catalyst, if paired with appropriate pelletizing and preparation method.

The introduction of hexane and polypropylene glycol (PPG) as micellar swelling agents into the original COK-12 synthesis was studied in order to tailor the mesoporous structure of the system. Hexane was used as a micelle expander and as an agent to produce silica mesocellular foams, with “ink-bottle” shaped pores with a larger diameter than that of the original COK-12. By adding PPG into the synthesis, the shift of the mesostructure of COK-12 from 2D hexagonal to a multilamellar vesicular configuration was studied, resulting in the progressive formation of this type of material with increasing concentration of PPG.

The flexibility of the COK-12 synthesis in terms of upscaling and tailoring of the mesostructure was examined throughout this work, with an aim to contribute to the existing and expanding knowledge regarding more versatile, sustainable and possibly industrial OMS production.

# Kurzfassung

Ordered Mesoporous Silica (OMS) gehört zu der Familie der Silica-Nanomaterialien mit periodisch angeordneten Mesoporen im Größenbereich zwischen 2 und 50 nm. Diese werden zunehmend in unterschiedlichen Forschungsfeldern wie Medikamentenfreisetzung, Adsorption, Separation und Katalyse eingesetzt. COK-12 ist ein OMS, das über eine Soft-Templating-Methode unter Nutzung des Blockcopolymers P123 als strukturbestimmenden Zusatz erzeugt wird. Die Synthese erfolgt bei Raumtemperatur unter milden Reaktionsbedingungen. Im Vergleich zu den am weitesten bekannten OMS-Materialien ist die Synthese von COK-12 zeiteffizient, günstig und umweltfreundlich. Dabei wird ein OMS-Material analog zu dem bereits etablierten SBA-15 erzeugt.

Die vorliegende Dissertation umfasst die Synthese eines als COK-12 bekannten OMS-Materials, dem Scale-Up der Synthese sowie die Anpassung und Modifizierung der ursprünglich hexagonal-angeordneten Mesoporen bezüglich Porengrößen und Porenform. Das diskontinuierliche Scale-Up im Batchprozess führt zu nahezu identischen Materialeigenschaften im Vergleich zu dem ursprünglichen COK-12. Ein Scale-Up der COK-12-Synthese wurde zusätzlich im kontinuierlichen Prozess erprobt. Dessen Installation und Operation wurde mit dem Ziel durchgeführt, um die Möglichkeit einer Produktion von großen Mengen an COK-12 mit einheitlichen Materialeigenschaften zu validieren. Durch eine Variation der Alterungszeit als auch der Fließrate der Lösungen konnte COK-12 im kontinuierlichen Prozess mit nahezu identischen Eigenschaften wie das ursprüngliche COK-12 erzeugt werden.

COK-12 wurde erfolgreich in verschiedenen Formen (Pulver, Pressgranulate und Monolithe) als Trägermaterial für  $\text{Na}_2\text{WO}_4\text{-Mn/SiO}_2$ -Katalysatoren für die Oxidative Kopplung von Methan eingesetzt. Die resultierenden Aktivitäten sind vergleichbar mit denen des auf SBA-15-geträgerten Katalysators Der

Vorteil der Nutzung von COK-12 im Vergleich zu anderen OMS-Materialien liegt in der vergleichsweise simplen COK-12-Synthese, weshalb es ein interessanter Kandidat für eine mögliche industrielle Produktion des  $\text{Na}_2\text{WO}_4\text{-Mn/SiO}_2$ -Katalysators ist, wenn geeignete Pelletierungs- und Herstellungsmethoden angewendet werden.

Die Zugabe von Hexan und Polypropylenglykol (PPG) zur Aufweitung der Mizellen in der ursprünglichen COK-12-Synthese wurde untersucht, um die mesoporöse Struktur des Systems zu variieren. Hexan wurde eingesetzt zur Aufweitung der Mizellen und als Hilfsmittel zur Produktion mesozellulärer Silica-Schäume mit „ink-bottle“-förmigen Poren sowie vergrößertem Porendurchmesser im Vergleich zu denen des ursprünglichen COK-12. Durch die Zugabe von PPG in die Synthese verändert sich die Mesoporenstruktur der ursprünglichen hexagonalen 2D-Struktur zu einer multilamellaren vesikulären Anordnung, die mit zunehmender PPG-Konzentration verstärkt wird.

Die Flexibilität der COK-12-Synthese wurde in dieser Arbeit in Bezug auf ein Scale-Up und eine Porenmodifikation weitreichend untersucht, mit dem Ziel das existierende Wissen in Bezug auf eine vielseitige, nachhaltige sowie eine potentielle Industrieproduktion der COK-12-Synthese zu entwickeln.

# Table of contents

Acknowledgments	vii	
Abstract	ix	
Kurzfassung	xi	
Introduction	xvii	
<b>1</b>	<b>Literature review</b>	<b>1</b>
1.1	General considerations on porous solids	1
1.2	Ordered mesoporous silica materials	2
1.3	Synthesis of ordered mesoporous silica	6
1.3.1	Synthesis mechanism and pathway	6
1.3.1.1	Processes involved in ordered mesoporous silica synthesis	8
1.3.2	Self-assembly of block copolymers used as structure-directing agents	11
1.3.2.1	The packing parameter	14
1.3.2.2	The hydrophilic/hydrophobic volume ratio	15
1.3.3	Pore size control: micellar swelling agents	16
1.3.3.1	Silica mesocellular foam	18
1.3.4	Pore shape control: tailoring the mesostructure	21
1.3.4.1	Multilamellar vesicular silica	22
1.3.5	Synthesis of COK-12	23
1.3.6	Upscaling and continuous synthesis of ordered mesoporous silica	25
1.4	Ordered mesoporous silica as a catalyst support	26
1.4.1	Ordered mesoporous silica as a catalyst support: advantages and drawbacks	26

1.4.2	Oxidative coupling of methane	27
1.4.2.1	Na <sub>2</sub> WO <sub>4</sub> -Mn/SiO <sub>2</sub> catalyst for the oxidative coupling of methane	30
1.4.2.2	Na <sub>2</sub> WO <sub>4</sub> -Mn/SiO <sub>2</sub> catalyst supported on SBA-15	31
1.5	Summary and open questions	32
<b>2</b>	<b>Characterization methods</b>	<b>34</b>
2.1	Small-angle X-ray diffraction	35
2.2	Nitrogen sorption	37
2.3	Scanning electron microscopy	43
2.4	Transmission electron microscopy	43
2.5	Powder X-ray diffraction	44
2.6	Inductively coupled plasma – optical emission spectroscopy	44
2.7	Gas pycnometry	45
2.8	Energy-dispersive X-ray spectroscopy	46
<b>3</b>	<b>Batch synthesis of COK-12</b>	<b>47</b>
3.1	Experimental	48
3.1.1	Reference material synthesis: powder COK-12	48
3.1.2	Monolithic COK-12 synthesis	49
3.1.3	Upscaling of powder and monolithic COK-12 synthesis	50
3.1.4	Catalyst preparation and performance studies	50
3.1.4.1	Catalyst support preparation	50
3.1.4.2	Catalyst preparation	51
3.1.4.3	Catalytic performance tests	52
3.2	Mesostructure and porosity of powder COK-12	53

3.2.1	Mesostructure and porosity of powder COK-12: single batch synthesis	53
3.2.2	Mesostructure and porosity of powder COK-12: upscaled batch synthesis	60
3.3	Mesostructure and porosity of monolithic COK-12	65
3.4	COK-12 as a catalyst support for the oxidative coupling of methane	74
3.4.1	Catalyst composition and structure	75
3.4.1.1	Catalyst structure before OCM	75
3.4.1.2	Catalyst structure after OCM	85
3.4.2	Catalyst performance in the oxidative coupling of methane	89
3.4.2.1	Catalytic performance at standard OCM conditions	89
3.4.2.2	Catalytic performance at lower reaction temperature	92
3.4.2.3	Catalyst stability after prolonged time on stream	93
3.5	Conclusions and outlook	95
<b>4</b>	<b>Tailoring the mesostructure of COK-12</b>	97
4.1	Materials synthesis	98
4.2	Hexane as a swelling agent: synthesis of a silica mesocellular foam	100
4.3	Polypropylene glycol as a swelling agent: synthesis of multilamellar vesicular silica	110
4.4	Conclusions and outlook	120
<b>5</b>	<b>Continuous synthesis of COK-12</b>	122
5.1	Conceptual and basic process design and installation	123
5.2	Continuous production: materials synthesis	126
5.2.1	Variation of the aging time	127
5.2.2	Variation of the feed stream flow rate	128

5.3	Influence of variation of operation parameters	131
5.3.1	Influence of the variation of the aging time on COK-12 mesostructure	132
5.3.2	Influence of the variation of the flow rate on COK-12 mesostructure	138
5.4	Conclusions and outlook	142
<b>6</b>	<b>Conclusions and outlook</b>	144
<b>7</b>	<b>References</b>	148
	Symbols and abbreviations	165
	List of figures	167
	List of tables	178

# Introduction

Ordered mesoporous silica materials (OMS) have been in development since their discovery in the early 1990s. These materials exhibit unique properties, specifically large surface areas and well-defined ordered pores of controlled size, usually ranging from 2 to 20 nm, that are the result of templating with organic molecules. Given their particular properties, OMS materials have found application in fields such as catalysis, separation, adsorption, chromatography and drug delivery, among others. Part of the ongoing research is aimed at improving the sustainability of the synthesis of these materials. Furthermore, studies regarding the tailoring of these materials to yield distinct mesostructures have demonstrated numerous possibilities of unique OMS materials production.

The novel OMS denoted as COK-12, discovered in 2011, is an excellent candidate for OMS materials research. This material has properties analogous to the well-known SBA-15, exhibiting a mesostructure consisting of cylindrical pores 5 to 6 nm in size, arranged in a 2-dimensional hexagonal stacking. Similar to SBA-15, COK-12 is templated with the triblock copolymer P123. However, in contrast to SBA-15 the synthesis of COK-12 is carried out at room temperature and quasi neutral pH using an inexpensive silica precursor, affording a much more environmentally friendly and cost-effective synthesis. Furthermore, the almost immediate formation of the material, in contrast to SBA-15 which requires prolonged hydrothermal treatment, allows for potential continuous production.

The work presented here is based on the synthesis of COK-12, in terms of upscaling of the synthesis and tailoring of the material mesostructure. Given the myriad of applications of OMS, studies regarding large-scale production can pave the way for future industrial use of these materials. In this work, upscaling was studied in batch and continuous mode. Moreover, the flexibility of the

COK-12 synthesis to yield materials with a different mesostructure was studied by incorporation of micellar swelling agents into the synthesis. In this context, two new COK-12 mesophases were identified, namely mesocellular foam and multilamellar vesicular silica. These two phases exhibit enlarged pores which further broaden the spectrum of application of COK-12. Furthermore, investigations regarding the use of COK-12 as a catalyst support for the oxidative coupling of methane are presented, using COK-12 in powder and granular form. The latter is produced either by direct synthesis of monolithic COK-12 or by pressing of powder COK-12.

**The first part** of this thesis deals with the synthesis and batch upscaling of COK-12 (Chapter 3). Large-scale production of OMS is largely uninvestigated, given the harsh synthesis conditions typically required. To date there are only a few reports on the large-scale production of OMS, resulting in the synthesis of less than 30 g per batch. Large-scale production of OMS materials is convenient for experimental work that requires a large amount of OMS with consistent properties, as well as for potential commercial application. Additionally, the use of COK-12 as a support for the  $\text{Na}_2\text{WO}_4\text{-Mn/SiO}_2$  catalyst for the oxidative coupling of methane (OCM) is studied. Recently, the use of the analogous SBA-15 as a support for the  $\text{Na}_2\text{WO}_4\text{-Mn/SiO}_2$  catalyst for OCM resulted in an exceptional performance in comparison to other silica supports.

In this context, *the first goal* of this work is to synthesize and characterize powder COK-12, and subsequently upscale the synthesis to produce larger quantities of the same material while maintaining its characteristic mesostructure. The acidification of the COK-12 synthesis with the aim to produce granules in a size range suitable for use as a catalyst support in potential industrial applications is studied, as well as the upscaling of this monolithic synthesis approach. Both powder and monolithic COK-12 materials are used as catalyst supports for the  $\text{Na}_2\text{WO}_4\text{-Mn/SiO}_2$  catalyst and their activity in the OCM reaction are determined.

**The second part** of this thesis encompasses tailoring the COK-12 mesostructure by incorporation of micellar swelling agents

(Chapter 4). One of the most versatile characteristics of OMS synthesis has to do with the ability to tailor the mesostructure with the use of selected organic templating agents that form micellar superstructures, which in turn can be tailored by the use of micellar swelling agents. Depending on the templating agent selected for OMS synthesis, micellar swelling agents that solubilize within the micelle cores can be used to expand the size of the micelles, resulting in materials with larger pores and different pore shapes. This versatility further expands the potential application of OMS materials.

Under this framework, *the second goal* of this work is to study the effect of the use of micellar swelling agents in the COK-12 synthesis, namely hexane and polypropylene glycol (PPG). The main motivation behind the selection of these swelling agents is to produce pore enlargement. Interestingly, an increase in the pore size was not the only phenomenon observed, but also a mesophase change in COK-12. The use of hexane, which has been previously reported to produce materials with enlarged pores, resulted in the formation of mesocellular foam (MCF). The use of PPG produced a mesophase change from hexagonal to multilamellar vesicular (MLV).

**The third part** of this thesis comprises studies regarding the continuous production of COK-12 (Chapter 5). As was previously discussed, there is a lack of research regarding large-scale production of OMS materials. The continuous synthesis of COK-12 has been previously demonstrated using perfusion pumps to feed the reagent streams and produce a quality material with consistent properties.

Therefore, *the third goal* of this work is to design, install and operate a continuous COK-12 production unit, with the aim to produce the largest quantities reported of any OMS. The materials produced will be characterized and compared to the original COK-12 materials in order to demonstrate the possibility of large-scale continuous production.

This thesis is organized as follows:

*Chapter 1* includes a historical overview of OMS materials and typical synthesis methods, a summary of the methods available for tailoring the mesostructure of OMS materials, and a short look at the OCM reaction and the applicability of OMS materials as a catalyst support.

*Chapter 2* presents the characterization methods used throughout this work.

*Chapter 3* includes the synthesis and upscaling of powder and monolithic COK-12, and the application of COK-12 as a catalyst support for the  $\text{Na}_2\text{WO}_4\text{-Mn/SiO}_2$  catalyst in the OCM reaction.

*Chapter 4* describes the changes that occur in the mesostructure of COK-12 when micellar swelling agents are incorporated into the synthesis, namely hexane and PPG.

*Chapter 5* presents the basic design and operation of a continuous COK-12 production unit, along with experiments regarding variations in the time of aging of the COK-12 slurry and the flow rate of the feed streams, to determine the optimal conditions to produce a material with properties as close to the original COK-12 material as possible.

*Chapter 6* summarizes the main results of this study and highlights future perspectives for this work.

# 1 Literature review

## 1.1 General considerations on porous solids

Most solid materials are porous to some extent. A porous solid is a solid that contains cavities, channels or interstices which are deeper than they are wide. These cavities, or pores, are classified as described in Table 1.1<sup>1</sup>.

Table 1.1 Classification of pores according to the IUPAC.

Classification according to	Type of pore	Description
Size	Microporous	< 2 nm
	Mesoporous	2-50 nm
	Macroporous	> 50 nm
Availability to an external fluid	Closed pores	Completely isolated pores (Figure 1.1 a)
	Open pores	Continuous channel of communication with external surface (Figure 1.1 b, c, d, e, f)
	Blind pores	Open on one end (Figure 1.1 b, f)
	Through pores	Open on two ends (Figure 1.1 e)
Shape	Cylindrical	Either open (Figure 1.1 c) or blind (Figure 1.1 f)
	Ink-bottle	Figure 1.1 b
	Funnel-shaped	Figure 1.1 d
	Slit-shaped	Figure 1.1 c

## 1.2 Ordered mesoporous silica materials

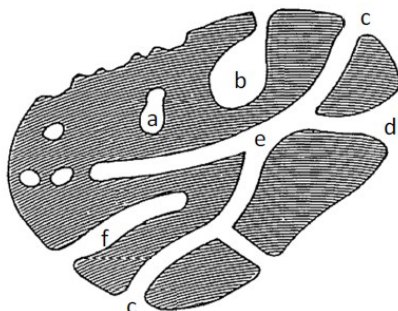


Figure 1.1 Illustrative cross-section of a porous solid<sup>1</sup>. For details see Table 1.1.

## 1.2 Ordered mesoporous silica materials

Ordered mesoporous silica (OMS) materials are a family of silica nanomaterials with pores ranging in size from 2 to 50 nm and amorphous silica walls. Uniform OMS pores periodically aligned in 2- or 3-dimensional structures. OMS are generally prepared via soft-templating with surfactants that self-assemble into micelles, around which silica condenses. Upon removal of the templating surfactant, a hydrothermally stable silica material with a highly-ordered pore structure that mimics the micellar arrangement is obtained (Table 1.2).

Since the initial development of ordered mesoporous materials in the early 1990s, OMS has gained widespread attention in various fields of research. With applications in areas such as drug delivery<sup>2</sup>, electrochemistry<sup>3</sup>, sensing<sup>4</sup>, bioadsorption<sup>5</sup>, separation<sup>6</sup> and catalysis<sup>7-12</sup>, OMS research has boomed in the past 20 years, resulting in a huge expansion of knowledge and skills in the field.

Inspired by the promising catalytic and adsorptive capacity of zeolites, as well as their limitations due to the dimension of their pores, research concerning the synthesis of silica materials with an

ordered uniform pore structure in a higher pore size range led to the discovery of the revolutionary M41S type materials by Mobil scientists<sup>13</sup>. These silica materials were the first to exhibit a uniform array of pores. However, evidence of synthesis of OMS dates as far back as 1969, when Chiola, et. al. patented a material then known as “low-bulk density silica”<sup>14</sup>. The porous network of this material was not specified due to the lack of detailed characterization, but more recent attempts to reproduce this synthesis suggested that it is an OMS similar to those of the M41S family of materials<sup>15</sup>.

In 1990, Yanagisawa, et. al. reported the use of cationic surfactants to produce alkyltrimethylammonium-kanemite complexes and their conversion to “microporous materials”, when in fact they had effectively produced a silica material with uniform mesoporosity templated by a surfactant, but failed to recognize it as such<sup>16</sup>.

The discovery of MCM-41 by Mobil scientists came two years later and is widely known as the beginning of studies on the template effect of micelles<sup>17</sup>. The most important findings of this work were, on one hand, the high degree of order that could be achieved in the array of pores, and on the other hand, the identification of the critical connection between the porous nature of the material and the nature of the surfactant used as a templating agent.

Since this discovery, the use of the so-called “soft-templating method” has been widely applied for ordered mesoporous materials synthesis. A key breakthrough occurred in 1998 with the discovery of SBA-15 by Zhao, et. al. SBA-15 is a combined micro- and mesoporous material synthesized under acidic conditions and templated with the commercially available amphiphilic non-ionic triblock copolymer P123, resulting in a material with hexagonally ordered uniform mesopores that can be tuned in size from 4 to 14 nm<sup>18</sup>. The thick microporous silica walls of this material are responsible for the high thermal stability that this material exhibits in comparison to its M41S analog, MCM-41. The use of a block copolymer as a soft-templating agent opened a

## 1.2 Ordered mesoporous silica materials

myriad of possibilities in OMS research, given that the properties of block copolymers can be tuned by manipulating their composition, molecular weight, or architecture.

In 2003, Ryoo, et. al. reported the synthesis of KIT-6, a large-pore OMS with a cubic pore structure analogous to MCM-48 of the M41S type materials, by using butanol to tailor the mesostructure of the templating agent P123<sup>19</sup>. The addition of butanol to the material synthesis led to the formation of micellar aggregates with a decreased curvature, which in turn produced an evolution from a hexagonal pore structure to a cubic mesophase. This was the first demonstration of this phenomenon for non-ionic triblock copolymer OMS synthesis.

More recently, Jammaer, et. al. have established the synthesis of the SBA-15 analog denoted as COK-12<sup>20</sup>. Templating of COK-12 is achieved by using P123 as the structure-directing agent, and the synthesis is quick, takes place at room temperature and quasi-neutral conditions. The synthesis of COK-12 is more environmentally friendly than that of its analogs, paving the way for possible mass production of this type of OMS.

Table 1.2 Ordered mesoporous silica materials, mesostructure and surfactant used<sup>21</sup>.

OMS label	Origin of label	Surfactant used	Mesostructure	Synthesis conditions
MCM-41	Mobil Composition of Matter	Alkyltrimethyl ammonium $C_nH_{2n+1}N^+(CH_3)_3X^-$ (with $n = 12, 14, 16,$ $18$ and $X = Cl$ or $Br$ )	Hexagonal $p6m$ 2-dimensional	Basic
MCM-48	Mobil Composition of Matter	Alkyltrimethyl ammonium $C_nH_{2n+1}N^+(CH_3)_3X^-$ (with $n = 12, 14, 16,$ $18$ and $X = X$ or $Br$ )	Cubic (bicontinuous gyroid) $la3d$ 3-dimensional	Basic

OMS label	Origin of label	Surfactant used	Mesostructure	Synthesis conditions
FSM-16	Folder Sheet Mesoporous	Alkyltrimethyl ammonium $C_nH_{2n+1}N^+(CH_3)_3X^-$ (with $n = 12, 14, 16$ or 18 and $X = X$ or Br)	Hexagonal $p6m$ 2-dimensional	Basic
HMS	Hexagonal Mesoporous Silica	Non-ionic amine surfactant $C_nH_{2n+1}NH_2$	Wormhole framework structure	Neutral
SBA-15	Santa Barbara Amorphous	Pluronic P123	Hexagonal $p6m$ 2-dimensional	Acidic
SBA-16	Santa Barbara Amorphous	Pluronic F127	Body-centered cubic $Im3m$ 3-dimensional	Acidic
KIT-6	Korea Advanced Institute of Science and Technology	Pluronic P123	Cubic (bicontinuous gyroid) $Ia3d$ 3-dimensional	Acidic
FDU-12	FuDan University	Non-ionic triblock copolymer B50-6600, Dow Chemicals	Face-centered cubic $Fm3m$ 3-dimensional	Basic
COK-12	Centrum voor Oppervlaktechnie & Katalyse	Pluronic P123	Hexagonal $p6m$ 2-dimensional	Quasi-neutral, room T

## 1.3 Synthesis of ordered mesoporous silica

### 1.3.1 Synthesis mechanism and pathway

The synthesis of OMS is based on the co-assembly of silica and surfactant molecules, and is referred to as *soft-templating* (as opposed to *hard-templating*, in which the structure-directing agent is a structured solid). Different mechanisms have been proposed for the soft-templating of OMS: in the *true liquid crystal templating* mechanism, a high concentration of the templating surfactant leads to the formation of mesophases prior to the addition of silica, while in the *cooperative self-assembly* mechanism, the process of self-assembly occurs even at low surfactant concentrations guided by the interactions between surfactant and silica<sup>22</sup>. The cooperative self-assembly mechanism has been widely accepted.

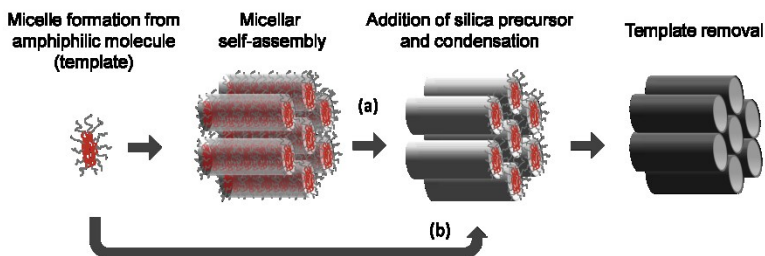


Figure 1.2 True liquid crystal templating mechanism (a) and the cooperative self-assembly mechanism (b). In the true liquid templating mechanism, the formation of a mesophase occurs prior to the addition of silica due to a high concentration of the templating molecule. In cooperative self-assembly, the silica-surfactant interactions guide self-assembly even at low surfactant concentrations.

#### *Cooperative self-assembly mechanism*

The cooperative self-assembly mechanism was first introduced by Chmelka et. al., concerning the use of cationic surfactants templates.

It proposes that anionic silicate oligomers interact with the positively charged heads of the surfactant molecules, driven by Coulomb forces. Silicate oligomers bind to the surfactant molecules, causing the interface to quickly become populated by tightly held silicate oligomers which consequently polymerize further. Polymerization of silicate is favored in the interface because (i) the silicate concentration is high and (ii) the negative charges of the silicate oligomers are partially screened by the surfactant. The reaction proceeds until the lowest interface energy is achieved, resulting in the final 3D mesophase. The assembly process is governed by the matching of the charge density at the interface<sup>22</sup>. This mechanism can be interpolated to many systems that have since then been studied – the driving forces are covalent bonding (in the case of surfactants which contain silicate species) or hydrogen bonding (when non-ionic surfactants are used), for example. Table 1.3 lists the main synthesis routes of OMS, along with the interactions that govern the synthesis process.

Table 1.3 Main synthesis routes for mesoporous materials with corresponding surfactants and main products<sup>24</sup>.

Route	Interactions	Symbols	Remark	Typical products
S-I-	Electrostatic Coulomb force	S <sup>+</sup> : cationic surfactants I <sup>-</sup> : anionic silicate species	Under basic media	MCM-41, MCM-48, MCM-50, SBA-6, SBA-8, FDU-11, FDU-13, etc.
S-I+	Electrostatic Coulomb force	S <sup>-</sup> : anionic surfactants I <sup>+</sup> : transition metal ions	Under aqueous condition	Mesoporous alumina
S <sup>+</sup> X-I <sup>+</sup>	Electrostatic Coulomb force, double layer H bond	S <sup>+</sup> : cationic surfactants X: Cl <sup>-</sup> , Br <sup>-</sup> , I <sup>-</sup> , SO <sub>4</sub> <sup>2-</sup> , NO <sub>3</sub> <sup>-</sup> I <sup>+</sup> : silicate species	Under acidic media	SBA-1, SBA-2, SBA-3

### 1.3 Synthesis of ordered mesoporous silica

Route	Interactions	Symbols	Remark	Typical products
S <sup>-</sup> N <sup>+</sup> -I <sup>-</sup>	Electrostatic Coulomb force	S <sup>-</sup> : anionic surfactants (lab- made) N <sup>+</sup> : cationic amino group of TMAPS or APS I <sup>-</sup> : anionic silicate species	Under basic condition	AMS-n
S <sup>-</sup> X <sup>+</sup> I <sup>-</sup>	Electrostatic Coulomb force, double layer H bond	S <sup>-</sup> : anionic phosphate surfactants X <sup>+</sup> : Na <sup>+</sup> , K <sup>+</sup> , Cr <sup>3+</sup> , etc. I <sup>-</sup> : transition metal ions	Under basic condition	W, Mo oxides
S <sup>0</sup> I <sup>0</sup> (N <sup>0</sup> I <sup>0</sup> )	H bond	S <sup>0</sup> : non-ionic surfactants I <sup>0</sup> : silicate species N <sup>0</sup> : organic amines	Under neutral condition	HMS, MSU, disordered wormlike mesoporous silicates
S <sup>0</sup> H <sup>+</sup> X <sup>-</sup> I <sup>-</sup>	Electrostatic Coulomb force, double layer H bond	S <sup>0</sup> : non-ionic surfactants X <sup>-</sup> : Cl <sup>-</sup> , Br <sup>-</sup> , I <sup>-</sup> , SO <sub>4</sub> <sup>2-</sup> , NO <sub>3</sub> <sup>-</sup> I <sup>-</sup> : silicate species	Under acidic condition pH <2	SBA-11, SBA-12, SBA-15, SBA-16, FDU-1, FDU-5, FDU-12, KIT-5, KIT-6
S <sup>+</sup> -I <sup>-</sup>	Covalent bond	S <sup>+</sup> : cationic surfactants containing silicates I <sup>-</sup> : silicate species	Under basic condition	Mesoporous silica

#### 1.3.1.1 Processes involved in ordered mesoporous silica synthesis

Various processes have been established for the synthesis of OMS, such as hydrothermal synthesis, non-aqueous process and aqueous process (also referred to as precipitation synthesis). The synthesis protocol used throughout this work corresponds to the precipitation

synthesis, which involves five steps: (1) reaction (usually in the liquid phase), (2) solid recovery, (3) washing, (4) drying and (5) template removal<sup>21</sup>.

### *Reaction*

The reaction step consists of two sub-steps: reaction and aging or maturation. In the reaction step, reactants are mixed, left to react, and the solid phase precipitates. Depending on the parameters of the synthesis, precipitation can be faster or slower. For syntheses that adopt sodium silicate as the silica precursor, the precipitation time tends to be short and therefore condensation is difficult to control. The opposite is true for syntheses using alkoxysilanes as silica precursors – condensation is easier to control because precipitation time is longer. Stirring is often required during this stage, for reactant mixing, and in some cases, for morphological control of the final OMS particles<sup>25</sup>. Mixing is usually a crucial parameter in OMS synthesis, resulting in difficulty to upscale the process.

After the formation of the solid, an aging step is often implemented, to consolidate the silica walls by increasing the degree of condensation. This step usually takes place under static conditions and at high temperatures. In the cases in which non-ionic surfactants are used as templating agents, the aggregation of the block copolymers depends mainly on the temperature – high temperatures (up to 150°C) and long aging times (up to 48 h) are usually required to obtain a quality material.

### *Solid recovery*

Filtering is usually used to separate the solid organic-inorganic hybrid from the solvent, specifically vacuum filtration. This step, although not frequently studied, is important if the synthesis is intended to be produced on a scale larger than laboratory scale.

### *1.3 Synthesis of ordered mesoporous silica*

#### *Washing*

Washing of the recovered solid is necessary to remove by-products and other unwanted components. The effect of washing on the resulting material has been seldom studied. Two things should be considered: (i) the washing method can have an effect on the final material properties<sup>26</sup> and (ii) the washing step can aid in the removal of the templating agent, which would reduce the amount of energy required for the final step of the synthesis process.

#### *Drying*

This step in the OMS synthesis process is highly important, given that depending on the initial reaction conditions, changes in the mesophase can occur. The drying step takes place at moderately high temperatures (50-80°C) and is considered as a supplementary reaction step, in which structural and textural changes can take place. Transformations that occur during the drying step depend on the flexibility of the silica network. It has been reported that a short reaction time can lead to a flexible silica network, which upon drying can lose ordering of the porous structure. For these reasons, the reaction time and the drying temperature should be adjusted to control the structural and textural properties of the final material.

#### *Template removal*

The removal of the organic template for the inorganic framework results in the final mesoporous material. The most common methods of template removal are calcination and chemical extraction.

Calcination temperature is chosen based on the molecule used as a template. Higher temperatures guarantee that the template will be fully removed, but can have an impact on the textural properties of the material because shrinkage can occur. This can be avoided by using longer calcination times as opposed to higher

temperatures. Additionally, the calcination atmosphere can be adjusted in order to control the final chemical composition of the surface of the OMS. Calcination is the most efficient way to remove the template, but is ultimately a wasteful process because the template is destroyed and has no possibility of being reused.

This can be avoided by removing the template via chemical extraction, which is performed in liquid and requires additional synthesis steps of washing, solid recovery and drying. This method is highly efficient for the removal of the template, but requires several extraction runs. The advantage of this method is that the template can be recovered and reused. However, large quantities of solvent are usually necessary and the time scale is considerably increased when this method of template removal is applied.

New methods of template removal have been recently studied and include shorter-time calcination, microwave digestion of the template and ultrasonic template removal, amongst others<sup>21</sup>.

### 1.3.2 Self-assembly of block copolymers used as structure-directing agents

The porous structure of OMS is obtained by templating with a surfactant that functions as a structure-directing agent, also known as templating agents. In this section, the structure-directing agents typically used in OMS synthesis are reviewed, with an emphasis on the non-ionic amphiphilic triblock copolymer commercially known as P123, which is the templating agent used throughout this work.

Surfactants are amphiphilic compounds, meaning they contain a hydrophilic or polar group, and a hydrophobic or non-polar group in their structure. Given their nature, in solution they can self-assemble into discrete aggregates called micelles at the critical micelle concentration (CMC). At concentrations higher than the CMC, further aggregation leads to the formation of spherical or cylindrical micelles, and at even higher concentrations, they form

### *1.3 Synthesis of ordered mesoporous silica*

thermodynamically stable 2D or 3D ordered mesostructures with long-range order.

The resulting mesophase depends not only on surfactant concentration, but also on the OMS synthesis conditions: incorporation of additives and variations in temperature and pH produce different mesophases. Properties such as the length of the hydrophobic groups and the hydrophobic/hydrophilic volume ratio also play a role in the final mesostructure of the material. This flexibility and versatility allows for many possibilities regarding the design and engineering of the porous structure of OMS<sup>23</sup>. More details on micellar self-assembly and mesostructure tailoring is found in section 1.3.2.

To illustrate the variety of mesophases that can be obtained via templating OMS with different surfactants, a summary of well-known OMS materials and their final structure is shown in Table 1.2.

Surfactants used for OMS synthesis are generally classified according to the nature of the interaction between their polar group and the silica precursor used for synthesis. Anionic surfactant heads carry a net positive charge, as opposed to cationic surfactants which have a net negative charge. Non-ionic surfactants have no net charge. It's important to point out that non-ionic surfactants, especially block copolymers based on polyethylene oxide, are particularly attractive for use in OMS production because they are less expensive than ionic surfactants, and more importantly, are non-toxic and biodegradable<sup>24</sup>.

Block copolymers consist of blocks of one of homopolymer attached sequentially to blocks of a different homopolymer. The different chemical nature of the homopolymers - one is hydrophilic and the other is hydrophobic - result in an amphiphilic macromolecule. This allows block copolymers to self-assemble into a number of ordered mesostructures, driven by long-range repulsive (chemical incompatibility of the blocks) and short range attractive (covalent bond of the blocks) forces<sup>23</sup>.

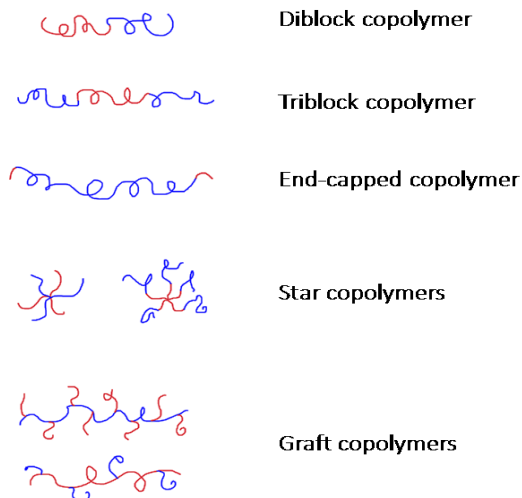


Figure 1.3 Schematic of various block copolymer architectures. Red and blue blocks represent the hydrophobic and hydrophilic blocks.

Since their first use by Zhao et. al., commercial amphiphilic block copolymers gained much attention as structure-directing agents for large-pore OMS preparation. In particular, the use of the commercial Pluronic® family of surfactants paved the way for ample research concerning design and tailoring of the mesostructure of OMS. These surfactants, generally known as Poloxamers, are non-ionic triblock copolymers composed of a central hydrophobic chain of poly (propylene oxide) (PPO) flanked by two hydrophilic chains of poly (ethylene oxide) (PEO)<sup>28</sup>.

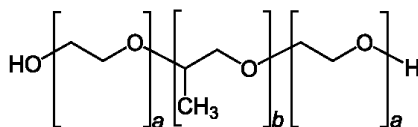


Figure 1.4 General structure of Poloxamers. A hydrophobic polypropylene oxide (PPO) block (center) is flanked by two hydrophilic polyethylene oxide (PEO) blocks. Variations in the chain lengths of the PPO and PEO blocks give rise to different mesostructures upon self-assembly.

### 1.3 *Synthesis of ordered mesoporous silica*

For Pluronic, the name of the copolymer reflects its properties. The first character in the name is a letter, and it defines its physical form at room temperature (L for liquid, P for paste and F for flake). The letter is followed by two or three digits. The first digit (or the first 2 digits, in a 3-digit number), multiplied by 300, indicates the approximate molecular weight of the PPO block. The last digit multiplied by 10 indicates the weight percentage of PEO block. Following this, P123 is a paste with a PPO molecular weight of 3600 Da and 30 % wt PEO. Its chemical formula is  $\text{H}(\text{OC}_2\text{H}_4)_{20}(\text{OC}_3\text{H}_6)_{70}(\text{OC}_2\text{H}_4)_{20}\text{OH}$ .

P123 can self-assemble at interfaces and in solution, and in OMS synthesis can self-assemble in a cooperative manner with the silica precursor required for synthesis. More details on this can be seen in section 1.3.5.

One of the main advantages of soft templating of mesoporous materials is that the mesopore structure, shape and size can be adjusted in various ways: by controlling the synthesis conditions (temperature, pH, etc.), by manipulating the properties of the structure-directing agent (such as hydrophobic/hydrophilic ratio, hydrophobic chain length, or by incorporation of micellar swelling agents), by using mixed surfactants, amongst others. This work encompasses the use of micellar swelling agents in the synthesis of COK-12 to increase the size of the pores and generate new mesophases.

#### 1.3.2.1 The packing parameter

As was briefly mentioned in section 1.3.2, self-assembly to ordered structures requires the simultaneous action of long-range repulsive and short-range attractive forces. In the case of block copolymers, the long-range repulsive force is the incompatibility (phase separation) of the hydrophilic and hydrophobic block, and the short-range attractive force is the covalent binding of the blocks.

The curvature of the interface can be described by the packing parameter  $g$ , which is given by<sup>29</sup>:

$$g = \frac{v}{l} x \frac{1}{a} \quad (1)$$

In which (for block copolymer micelles in aqueous solution):

$v$ : total volume of the hydrophobic chains plus any cosolvent (organic molecules) between the chains

$a$ : effective hydrophilic headgroup area at the aqueous/micelle surface

$l$ : kinetic hydrophobic tail length

The most simple shapes are spheres ( $g = 1/3$ ), cylinders ( $g = 1/2$ ) and planar surfaces or bilayers ( $g = 1$ ). The expected mesophase sequence as a function of  $g$  value is (i) close-packed cubic ( $Fm\bar{3}m$ ,  $Im\bar{3}m$ , etc.) for  $g < 1/3$ , (ii) 2D hexagonal ( $p6m$ ) for  $1/3 < g < 1/2$ , (iii) loose-packed cubic ( $Ia\bar{3}d$ ) for  $1/2 < g < 1$  and (iv) lamellar for  $g = 1$ <sup>24</sup>.

### 1.3.2.2 The hydrophilic/hydrophobic volume ratio

For nonionic structure-directing agents, the hydrophilic/hydrophobic volume ratio ( $V_H/V_L$ ) is especially useful in describing the formation of different mesophases. Block copolymers with high  $V_H/V_L$  ratios can direct the synthesis of cage-type cubic mesoporous materials, while block copolymers with medium  $V_H/V_L$  favor the formation of mesostructures with medium curvatures such as 2D hexagonal or 3D bicontinuous cubic structures<sup>24</sup>.

Micellization can be controlled in various ways. Incorporation of salts into aqueous solutions of block copolymer micelles effectively decrease the critical micellar concentration and critical micellar temperature, making it possible to produce ordered

### 1.3 *Synthesis of ordered mesoporous silica*

superstructures even at low micellar concentrations (known as the “salting-out” effect). Addition of ionic surfactants to the block copolymer solution may lead to the formation of hybrid aggregates or hierarchical pores. Addition of organic species increases the hydrophobic volume, decreasing the high  $V_H/V_L$  ratio and therefore shifting the superstructure to more loose-packed structures (2D hexagonal to 3D bicontinuous, for example)<sup>24</sup>. The addition of organic species will be reviewed in more detail in sections 1.3.3 and 1.3.4.

#### 1.3.3 Pore size control: micellar swelling agents

As much as the need for larger pores for practical applications led to the search for ordered mesoporous materials when only zeolites were available, materials with even larger pores offer additional benefits for various applications.

The pore size of OMS can be controlled by various methods, such as adjusting synthesis parameters (temperature, time, etc.)<sup>18,31–33</sup>, by selection of templating agents that yield larger pores<sup>17,34</sup> or by incorporation of species that increase the dimensions of the micelles, namely micellar swelling agents<sup>35–38</sup> (see Figure 1.5).

Given that the size of the mesopores depends mainly on the size of the hydrophobic group of the templating agent<sup>40</sup>, an increase in the size of the PPO block of typical PEO-PPO-PEO surfactants used in OMS synthesis will yield a material with larger pores. By incorporating organic molecules that can solubilize inside the hydrophobic region of the micelles, it is possible to effectively increase their size, and thus, the size of the pores (Figure 1.5, bottom). The use of micellar swelling agents was proven to be effective in increasing the pore size; however accompanied by a transition to another mesostructure<sup>41</sup> or a loss of ordering<sup>35</sup>. Synthesis at lower temperatures was effective in yielding ordered materials with larger pores<sup>42</sup>. Incorporation of inorganic salts allowed for lower temperature synthesis while also yielding ordered

materials<sup>37</sup>. More recently, mesocellular foams (MCF) with spherical pores connected by a window (also known as “ink-bottle” pores) have been synthesized using an inexpensive silica precursor via partitioned cooperative self-assembly<sup>43</sup>.

Table 1.4 summarizes some of the most relevant mesoporous silica materials produced by incorporation of swelling agents.

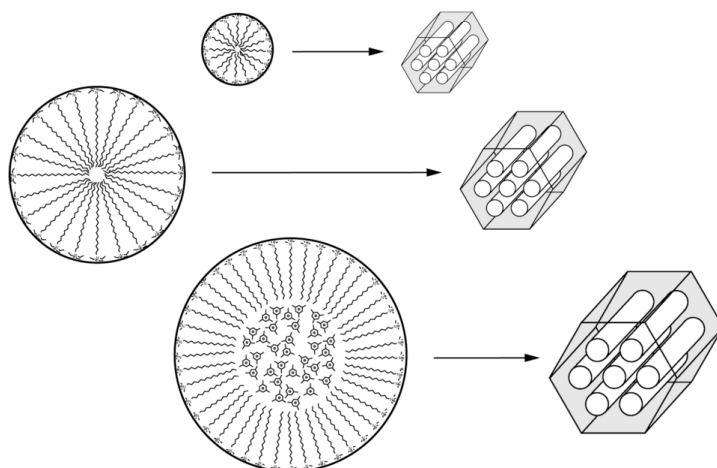


Figure 1.5 Adjustment of pore size of ordered mesoporous materials by adjusting the dimensions of the hydrophobic block through surfactant selection (top and middle) and by incorporation of micellar swelling agents (bottom)<sup>39</sup>. Reprinted with permission from M. Kruk: ‘Access to Ultralarge-Pore Ordered Mesoporous Materials through Selection of Surfactant/Swelling-Agent Micellar Templates’, *Acc. Chem. Res.*, 2012, **45**(10), 1678-1687. Copyright 2012 American Chemical Society.

Part of this work encompasses studies regarding the facile synthesis of a silica mesocellular foam (MCF) using hexane as a swelling agent and P123 as a templating agent, at room temperature and quasi-neutral synthesis conditions (see section 4.2).

### 1.3 Synthesis of ordered mesoporous silica

Table 1.4 Mesoporous silica materials produced by incorporation of swelling agents

Material	Templating agent	Swelling agent	Mesostructure	Pore size [nm]
SBA-15-based <sup>41</sup>	P123	1,3,5-TMB	Mesocellular foam (MCF), spherical “ink-bottle” pores	32
LP-FDU-12 <sup>33</sup>	F127	1,3,5-TMB	3D face-centered cubic, spherical pores	27
SBA-15-based <sup>42</sup>	P123	Hexane	2D hexagonal, cylindrical pores	15
SBA-15-based <sup>44</sup>	P123	1,3,5-TIPB	2D hexagonal, cylindrical pores	26
ULP-FDU-12 <sup>45</sup>	F127	Ethylbenzene	3D face-centered cubic, spherical pores	36
SBA-15-based <sup>46</sup>	P123	1,3,5-TIPB	2D hexagonal, cylindrical pores	18
LP-SBA-15 <sup>47</sup>	F127	Toluene	2D hexagonal, cylindrical pores	20
SBA-15-based <sup>43</sup>	P123	Hexane	Mesocellular foam (MCF), spherical “ink-bottle” pores	24

#### 1.3.3.1 Silica mesocellular foam

Mesocellular foams (MCF) are composed of uniformly sized large spherical cells that are connected by uniform windows, creating an interconnected 3-D pore system (Figure 1.6). The synthesis of silica MCFs was first reported by Stucky, et. al. using P123 as a structure-directing agent and 1,3,5-trimethylbenzene (TMB) as an organic

cosolvent, which acted as a micellar swelling agent<sup>41</sup>. The formation mechanism proposed in this study argues that adding TMB to the P123 solution produces uniform droplets of TMB/P123 in water, forming a microemulsion. The subsequently added silica source, in this case the commonly use tetraethyl orthosilicate (TEOS), hydrolyzes at the surface of the TMB/P123 droplets and then polymerizes, resulting in a composite material with interconnected spherical cells. The size of the cells corresponds to the size of the TMB/P123 droplets, and the windows between the cells form as a result of adjacent droplets coming into contact.

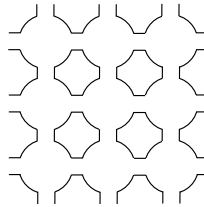


Figure 1.6 Schematic representation of a cross-section of MCF mesostructure, with “ink-bottle” or cage-like pores consisting of large spherical cells connected by narrow windows.

Further studies into the formation mechanism revealed that the cage-like or “ink-bottle” MCF structure can result from a phase transition from hexagonal to MCF upon increasing addition of TMB<sup>48</sup>. The transition is characterized by a sharp increase in the pore size, even though the 2D hexagonal symmetry was still observed in SAXS patterns. They proposed that a change in morphology without an accompanying change in the SAXS pattern could be the result of the formation of a noded structure in the cylindrical pores, which maintained their hexagonal packing. Upon increasing TMB addition, the nodes separate into spherical micelles and aggregate to form the MCF (Figure 1.7).

### 1.3 Synthesis of ordered mesoporous silica

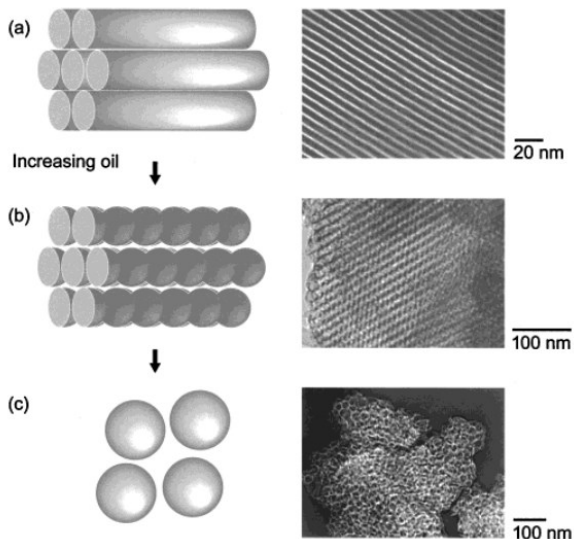


Figure 1.7 Progression of the morphological transition in P123 materials swollen by 1,3,5-trimethylbenzene ("oil")<sup>48</sup>. Increasing oil concentration produced enlargement of the pore size until the hexagonal mesostructure was lost and interconnected spherical micelles were formed. Reprinted with permission from J.S. Lettow, Y.J. Han, P. Schmidt-winkel, P. Yang, D. Zhao, G.D. Stucky, and J.Y. Ying: 'Hexagonal to Mesocellular Foam Phase Transition in Polymer-Templated Mesoporous Silicas', *Langmuir*, 2000, **16**(22), 8291-8295. Copyright 2000 American Chemical Society.

Recently, the synthesis of MCFs via partitioned cooperative self-assembly (PCSA) using sodium silicate as the silica precursor and P123 as the structure-directing agent has been reported<sup>43,49</sup>. In these studies, as opposed to the conventional method of adjusting the hydrophobic volume  $V_L$  with an aim to reduce the micellar curvature and therefore change the mesostructure, the hydrophilic volume  $V_H$  is also manipulated, resulting in materials with a bimodal pore structure. The swelling agents TMB and hexane are used to adjust  $V_L$  and PCSA is used to manipulate the PEO shell, which can be tailored by incorporating the silica precursor at different times and in varying quantities in the synthesis. The synthesis of MCF

silica based on the synthesis of COK-12 and using hexane as a micellar swelling agent is addressed in the present work.

### 1.3.4 Pore shape control: tailoring the mesostructure

The final mesophase structure depends on the liquid crystal phases of the templating agent. The selection of the templating agent, the use of mixed surfactants, the addition of organic agents and the synthesis conditions (temperature, presence of salts, etc.) all play a role in defining the mesostructure of the material. Below is a summary and description of liquid crystal mesophases formed by self-assembly of surfactants that have been observed in the synthesis of OMS<sup>50</sup>

#### *Columnar mesophases*

The most common columnar mesophase observed is the 2D hexagonal mesophase, which forms after the discontinuous cubic phase in which spherical micelles exist in solution but are not in contact with each other. The discontinuous spherical micelles merge to form cylindrical micelles that aggregate into a 2D hexagonal mesophase with  $p6m$  symmetry. SBA-15<sup>18</sup> and MCM-41<sup>17</sup> are the most well-known examples of materials with a 2D hexagonal mesostructure.

#### *Lamellar mesophases*

Lamellar mesophases are parallel stacks of amphiphilic bilayers. They have the lowest curvature energy (packing parameter  $g=1$ ). Lamellar mesophases form after 2D hexagonal mesophase. Multilamellar vesicular (MLV) silica materials have been prepared that exhibit this type of mesophase<sup>51</sup>.

### *1.3 Synthesis of ordered mesoporous silica*

#### *Bicontinuous mesophases*

Bicontinuous mesophases can be traversed in any direction, and exhibit long-range order. Examples of OMS materials that exhibit a bicontinuous mesophase include the well-known MCM-48 and KIT-6 with a bicontinuous cubic or bicontinuous gyroid symmetry, SBA-16 with a body-centered cubic mesostructure and FDU-12, with a face-centered cubic mesostructure.

Part of this work studies the shift from a 2D hexagonal mesophase to a multilamellar vesicular (MLV) mesophase of a mesoporous silica material by incorporation of polypropylene glycol (PPG), at room temperature and quasi-neutral synthesis conditions (see section 4.3).

#### 1.3.4.1 Multilamellar vesicular silica

Multilamellar vesicular silica (MLV) structures consist of concentric silica shells and voids in alternation (Figure 1.8). Initial reports on multilamellar vesicular silica came shortly after the discovery of MCM-41 by Tanev et.al. in the form of siliceous MLV prepared by a biomimetic approach, using a neutral diamine bolaamphiphile MLV as a template<sup>54</sup>. Siliceous MLVs with higher thermal and hydrothermal stability produced using an ionic gemini surfactant and TEOS as the silica precursors coined MSU-G were reported by Kim et.al., the same year that OMS templated by nonionic block copolymers were discovered<sup>55</sup>. Stable MLVs were also obtained using PEO-PPO-PEO type surfactants with a shortened PEO block in comparison to P123<sup>56</sup>. Following the discovery of SBA-15, the formation of MLVs via aerosol-assisted evaporation induced self-assembly (EISA) using TEOS and the nonionic triblock copolymer P123 as a structure directing was studied, yielding MLVs in the absence of cosurfactants and cotemplates<sup>57</sup>. After these initial studies, numerous reports regarding the synthesis of siliceous MLVs with P123 as a structure directing, TEOS as a silica source and

various cotemplates and cosurfactants have been published. Additives commonly used as micellar swelling agents have been useful in the preparation of MLVs, such as hexane<sup>58</sup>, 1,3,5 triisopropylbenzene (TIPB)<sup>51</sup>, perfluorooctanoic acid (PFOA)<sup>59</sup>, 1,3,5 trimethylbenzene (TMB)<sup>60</sup> and more recently, the amphiphilic comb-like polymer with a siloxane skeleton PSPE<sup>61</sup>. A study based on sodium silicate as a silica precursor and the electrically neutral  $\alpha,\omega$ -diamine surfactant Jeffamine D2000, similar to that used by Tanev, et.al., yielded MLV silica and materials with an “onion-like” morphology controlled by varying the synthesis temperature<sup>62</sup>. The synthesis of MLV silica based on the synthesis of COK-12 and using polypropylene glycol as a micellar swelling agent is addressed in the present work.

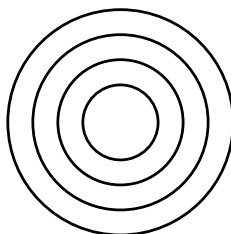


Figure 1.8 Schematic representation of a MLV pore mesostructure, consisting of concentric silica shells and voids in alternation.

### 1.3.5 Synthesis of COK-12

As was previously mentioned, COK-12 is a recently discovered OMS which is produced in a faster, inexpensive and more environmentally-friendly way in comparison to other OMS materials. COK-12 is prepared at room temperature by incorporating a solution of sodium silicate to a buffered (pH = 4-5) aqueous solution of spherical P123 micelles (for details on the preparation of COK-12, see section 3.1.1). The following is a formation mechanism proposed by Jammaer, et. al., as studied by small-angle X-ray scattering (SAXS), by incorporating increasing aliquots of silica precursor into the synthesis<sup>63</sup>.

### 1.3 Synthesis of ordered mesoporous silica

Silica is present in the sodium silicate solution as two times dissociated orthosilicic acid,  $\text{SiO}_2(\text{OH})_2^{2-}$ , which upon addition to the buffered P123 solution is neutralized to orthosilicic acid,  $\text{Si}(\text{OH})_4$ . At the buffer pH,  $\text{Si}(\text{OH})_4$  oligomerizes quickly. Silicate oligomers present a strong attractive interaction with the PEO blocks of the spherical P123 micelles, which limits the degree of crosslinking of the silicate network<sup>64</sup> and enriches the silica content in the PEO layer. With increasing silica content, the size of the micelles remains the same until 15 % of the nominal silicate amount used in COK-12 synthesis is reached. At 15 % silicate, the spherical micelles begin to aggregate and form cylindrical micelles – the PPO cores merge to form the core of the cylinder and the silica-enriched PEO shell makes up a mantle (Figure 1.9, c). The limited degree of cross-linking of the silicate network in the PEO block results in micelles that are flexible, hence the progression from spheres to cylinders.

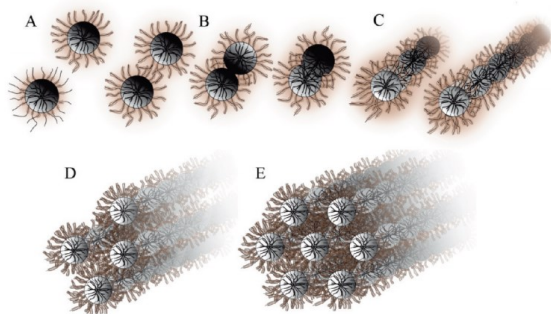


Figure 1.9 Schematic representation of the stages of formation of COK-12. (a) Silica species precipitate on the PEO blocks of the spherical P123 micelles which are in solution. (b) At a critical silica concentration, steric stabilization is lifted and (c,d) spherical micelles coalesce into cylinders that increase in size. (e) Further addition of silica species leads to the aggregation of the cylinders and eventually to the formation of a 2-dimensional hexagonally ordered mesostructure<sup>63</sup>. Reprinted with permission from J.

Jammaer, T.S. van Erp, A. Aerts, C.E.A. Kirschhock, and J.A. Martens: 'Continuous Synthesis Process of Hexagonal Nanoplates of P6m Ordered Mesoporous Silica', *J. Am. Chem. Soc.*, 2011, **133**(34), 13737-13745. Copyright 2011 American Chemical Society.

Further addition of silica promotes the growth of the cylinders and they begin to aggregate into a hexagonal pattern. The development of an ordered mesophase proceeds faster at higher concentrations of silicate, as was demonstrated by Jammaer, et. al.<sup>63</sup>. An increase in silica content eliminates the steric stabilization of the cylinders, enabling fast aggregation. Cylindrical micelles that are insufficiently coated with silica will not participate in aggregation until they reach the critical silica content. This ease of synthesis implies that the mixing conditions in COK-12 preparation are less critical. Likewise, the aging step of COK-12 synthesis is also less critical – a well-ordered material is obtained almost immediately after mixing.

### 1.3.6 Upscaling and continuous synthesis of ordered mesoporous silica

Given the harsh synthesis environment, OMS synthesis upscaling can be problematic, mainly due to issues concerning maintaining isothermal conditions. Common OMS syntheses also require long synthesis and aging times at elevated temperatures, which leads to time and energy consumption. Up until now, the synthesis of SBA-15 has been successfully upscaled to yield 24 to 27 g per batch<sup>26,65</sup>.

An alternative to batch upscaling is continuous production. Continuous production of OMS is desired not only to reduce the amount of steps required in the OMS synthesis process for potential industrial production, but also to allow for a more ecological synthesis of the material. A continuous synthesis process would reduce production costs and energy consumption, and would facilitate large-scale production with controlled material properties, avoiding reproducibility issues that may arise due to batch synthesis.

With the aim of studying the kinetics of formation of MCM-41 type materials, Linden et. al. reported a continuous synthesis process in a tubular reactor, in which the feed consisted of two streams: an aqueous solution of the templating agent and a

## 1.4 Ordered mesoporous silica as a catalyst support

solution of the silica precursor<sup>66</sup>. After initial mixing of the solutions, an ultrasonic bath was used for homogenization and then further mixing was carried out by static mixers. Although a continuous process was used for this study, its purpose was not to establish a continuous production process.

A study by Pitchumani et. al. regarding continuous production of mesoporous silica reports a simple preparation route by spray-drying<sup>67</sup>. A solution of colloidal silica was used as the silica source and P123 was used as the templating agent. Although a stable material was produced, the work was not focused on obtaining a highly-ordered material, and a material with a broad pore size distribution was obtained.

Recently, Jammaer et. al. have reported the synthesis of COK-12 in a continuous synthesis process<sup>63</sup>. The synthesis takes place at room temperature and near neutral pH and yields a highly-ordered material with the same properties as COK-12 prepared by batch synthesis. In this study, two different continuous synthesis setups were installed, a small-scale setup that relied on syringe pumping and a larger-scale setup in which pumping was carried out by hose pumps. The former resulted in a production rate of COK-12 of approximately 0.075 g/min and the latter 30 g/min. Although the synthesis step was carried out in continuous mode, subsequent steps (filtration, washing, drying, and calcination) were batch processes.

## 1.4 Ordered mesoporous silica as a catalyst support

### 1.4.1 Ordered mesoporous silica as a catalyst support: advantages and drawbacks

Ordered mesoporous silica materials (OMS) are very attractive for the preparation of highly dispersed metal and metal oxide supported catalysts in comparison to conventional support materials. Due to

their intrinsic properties, such as high surface area and uniform pore structure, the catalyst active species can be evenly dispersed, with uniform size and high concentration of active sites per mass of OMS support material. For metal and metal oxide supported catalysts, the need for large amounts of expensive and rare noble metals, when compared to the use of bulk materials, can be minimized<sup>68</sup>. The mesoporous structure of the support also plays an important role in catalytic activity. For example, in the transformation of levulinic acid (LA) to  $\gamma$ -valerolactone (GVL), it was demonstrated the yield increased with the use of OMS supports for the nanoparticulate Ni catalyst, and that the catalyst supported on COK-12 (as opposed to materials with a three-dimensional cubic pore structure, SBA-16 and KIT-6) produced the highest yield, due to the spatial distribution of Ni<sup>69</sup>. In spite of the many advantages of using OMS as a catalyst support, however, industrial application is still not viable given that the synthesis of OMS in large scale has not been sufficiently studied thus far and large-scale OMS production processes do not exist at an industrial level.

## 1.4.2 Oxidative coupling of methane

Natural gas is combustible gas that occurs in porous rocks of the earth's crust and is found with or near crude oil reserves. The methane content of natural gas can reach up to 98 %, depending on where it is produced, geographically<sup>70</sup>. Natural gas reserves throughout the world were estimated in 2014 at  $187 \times 10^{12}$  m<sup>3</sup>, which is the equivalent of  $169 \times 10^9$  tons of oil<sup>71</sup>. Much of the natural gas exists in remote regions, making transportation via pipelines unfeasible, and transportation by liquefaction and then shipping is very expensive. Natural gas is often reinjected and around 4 % is flared or vented, contributing to the greenhouse effect<sup>72</sup>. Furthermore, methane is the main component of biogas, formed by anaerobic digestion of energy crops, residues and wastes, with the methane concentration of biogas reaching up to 70 %<sup>73</sup>. Up to  $1.1 \times 10^{10}$  m<sup>3</sup> equivalent of natural gas was produced in the form of

#### 1.4 Ordered mesoporous silica as a catalyst support

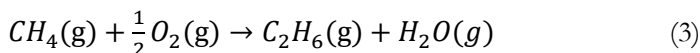
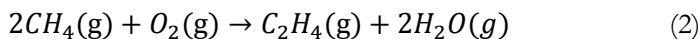
biogas in the European Union in 2010<sup>74</sup>. The vast quantities of methane available could serve as a feedstock for the production of chemicals and as a source of energy for the future.

Currently, the main use of methane is for heating purposes and for generation of electrical power, and the only important use in the chemical industry is for the production of synthesis gas (syngas, a mixture of H<sub>2</sub> and CO) through steam reforming. Utilization of methane would require its conversion either to a transportation fuel or to high volume chemicals such as methanol or ethylene<sup>72</sup>. However, the potential for the production of ethylene or liquid hydrocarbon fuels has not been fully realized, mostly because the conversion and/or selectivities of the feasible conversion processes are insufficiently high to be of interest for commercial application.

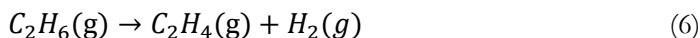
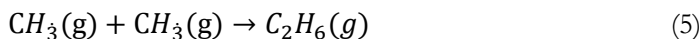
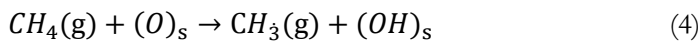
Generally two routes exist for the conversion of methane into useful products: direct and indirect. Indirect processes are two-step processes in which natural gas is converted initially into syngas which is then converted into the desired product. Direct routes are one-step processes in which methane reacts with oxygen (or another oxidizing species) to yield the desired product directly<sup>70</sup>, thus eliminating the costs of intermediate syngas generation.

The direct conversion of methane, however, is hindered by the difficulty to activate the stable methane molecule. Common issues associated with the direct conversion of methane come from kinetics and thermodynamics. High temperatures are required for methane activation, and at these conditions radical reactions in the gas phase are dominating. The strength of the C-H bond is stronger than the possible products, meaning that the products will be more reactive than the methane itself<sup>75</sup>. The activation of the inert methane molecule can be achieved, but will be accompanied by the activation of more reactive target molecules<sup>74</sup>. The challenge in methane conversion therefore lies mainly in the selectivity of the process, not the reactivity. Processes concerning the direct conversion of methane are still at the research stage, with catalysis playing an important role in their development.

One approach that has been proposed and tested to avoid these issues, based on catalysis and reaction engineering, is the oxidative coupling of methane (OCM) (equations 2 and 3) for the direct conversion of methane to ethylene and ethane, first proposed by Keller and Bhasin in the early 1980s<sup>76</sup>.



OCM occurs via a heterogeneous-homogeneous mechanism, with the reaction beginning on the catalyst surface with the generation of methyl radicals and continuing in the gas phase. The initial cleavage of the C-H bond of methane was proven as a crucial step of the OCM reaction, and the most widely accepted mechanism is homolytic breakage, in which methyl radicals are formed directly (equation 4). Once formed, the methyl radicals participate in gas phase and heterogeneous reactions, yielding various products: the recombination of two methyl radicals in the gas phase form ethane (equation 5), ethane dehydrogenation results on the formation of ethylene (equation 6), and carbon oxides are formed from the combustion of methane as well as the consecutive oxidation of C<sub>2</sub> products (see Figure 1.10)<sup>77</sup>.



One of the main challenges of OCM is finding a catalyst that can participate in the activation of the methane molecule, while suppressing unwanted secondary reactions. Catalysts so far tested for OCM exhibit insufficient selectivity at industrially relevant

### 1.4 Ordered mesoporous silica as a catalyst support

conversion levels, with maximum C<sub>2</sub> (ethane + ethylene) selectivity reaching about 80 %, with a single-pass yield of C<sub>2</sub> products of about 25 %. An “upper bound” or yield limit of 28 % has been predicted for OCM<sup>78</sup>. This yield limit, taken from the extensive review of OCM catalysts by Zavyalova et. al.<sup>79</sup>, shows a decrease in C<sub>2</sub> selectivity with increasing methane conversion within a virtual one pass yield limit between 25 and 30 %.

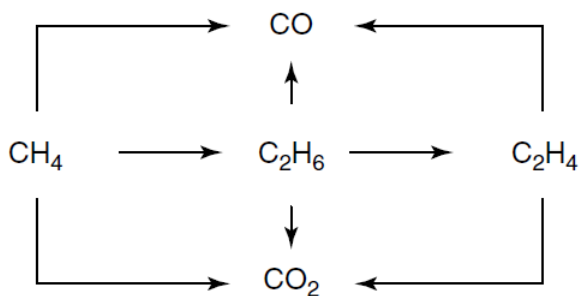


Figure 1.10 Simplified scheme of the OCM reaction<sup>77</sup>.

Although intensive efforts have been put into investigations regarding catalyst design, reaction engineering and process engineering of OCM, there are still to date no established industrial processes. The San Francisco based start-up Siluria Technologies has recently announced the installation of an OCM demonstration plant, which uses novel nanowire catalysts for the OCM process and has a high focus on the downstream processing, however no data concerning the catalyst has been revealed<sup>80</sup>.

#### 1.4.2.1 Na<sub>2</sub>WO<sub>4</sub>-Mn/SiO<sub>2</sub> catalyst for the oxidative coupling of methane

A very promising OCM catalyst was identified in the early 1990s, composed of 1.9 % wt Mn and 5 % wt Na<sub>2</sub>WO<sub>4</sub> supported on SiO<sub>2</sub><sup>81</sup>. This catalyst rivaled the performance of the leading OCM

catalysts, but exhibited stability for prolonged periods of time (more than 450 h)<sup>82,83</sup>. Investigations regarding the effect of each component (Na, W and Mn) on the catalytic activity and selectivity, effects of reaction pressure, temperature, methane to oxygen ratio, support material variation and catalyst preparation route have been conducted, and extensive literature is available<sup>43,84–95</sup>. A noteworthy and well-documented phenomenon that occurs in Na<sub>2</sub>WO<sub>4</sub>-Mn/SiO<sub>2</sub> catalysts is the phase transformation of the amorphous silica support to the crystalline  $\alpha$ -cristobalite phase after calcination at temperatures about 750°C<sup>86</sup>. This phase transition normally does not take place at this temperature, and is attributed to the lowering of the phase transition temperature of amorphous silica as a consequence of doping with sodium. This phenomenon is thought to be critical to the activity and selectivity of the catalyst, and is associated the formation of a crystalline phase that is inert to the OCM reaction, with a significant reduction in the specific surface area of the catalyst (as opposed to the fresh, uncalcined catalyst)<sup>96</sup>.

#### 1.4.2.2 Na<sub>2</sub>WO<sub>4</sub>-Mn/SiO<sub>2</sub> catalyst supported on SBA-15

An exhaustive study of the Na<sub>2</sub>WO<sub>4</sub>-Mn catalyst on a variety of supports confirmed the knowledge that the catalyst supported on silica exhibits remarkable stability and activity and selectivity and is a possible candidate for industrial application<sup>94</sup>. A highly promising achievement was reached regarding the variation of the type of silica support used for the Na<sub>2</sub>WO<sub>4</sub>-Mn catalyst, in terms of using OMS as opposed to commercial amorphous silica gel<sup>97</sup>. The SBA-15 supported catalyst exhibited a substantial increase in conversion in comparison to the catalyst supported on other forms of porous silica, as well as an increase in selectivity. The reason for this improved performance is thought to be a finer distribution of the catalytic components on the catalyst surface, given the ordered nature of the pores of SBA-15. In the present work, the performance of the Na<sub>2</sub>WO<sub>4</sub>-Mn catalyst supported on the OMS

### *1.5 Summary and open questions*

SBA-15 analog denoted as COK-12 is studied. COK-12 preparation is more environmentally friendly and inexpensive than SBA-15, making it a viable candidate for industrial application.

## 1.5 Summary and open questions

The present work is based on the synthesis of COK-12, an ordered mesoporous silica (OMS) material notable for its facile, economic and more environmentally-friendly synthesis. The synthesis of OMS materials, including COK-12, is carried out by templating with a micellar structure-directing agent, which upon removal produces the characteristic mesostructure and pore size of the OMS. The structure-directing agent selected for the synthesis will determine the mesostructure and pore size of the OMS. Further mesostructure and pore size tailoring can be carried out by addition of micellar swelling agents during the OMS synthesis, which solubilize inside the structure-directing agent micelles, thus enlarging the micelles or changing the mesophase altogether.

Taking into account the literature available, the synthesis of COK-12 –based materials, the processing of these materials and applications of COK-12 remain largely unexplored, in spite of the advantages that COK-12 synthesis holds over other OMS materials. Tailoring of the COK-12 mesostructure by using micellar swelling agents has not been reported thus far, and although the continuous synthesis of COK-12 has already been established, research regarding the optimization of this process for possible industrial use is necessary. Furthermore, there is still a gap in research concerning the use of COK-12 type materials in terms of surface functionalization (as has been widely studied for other OMS materials), processing, application, etc. A search on the term “COK-12” in Web of Science yields less than 20 results, as opposed to over 8000 for the analogous SBA-15. Therefore it is expected that studies regarding the upscaling and tailoring of COK-12 will open a window of opportunity regarding more economic and facile

synthesis of porous silica materials in an array of different mesostructures and pore sizes that can be tailored for specific applications.

## 2 Characterization methods

This section describes the characterization techniques used to routinely characterize the materials produced, with an overview of the technique, the information that can be obtained from each technique and methods for sample preparation. Routine characterization of COK-12 materials includes:

- Small-angle X-ray diffraction: pore ordering analysis
- Nitrogen sorption: pore shape analysis, determination of specific surface area and pore size distribution
- Scanning electron microscopy: morphological analysis
- Transmission electron microscopy: pore size, shape and ordering analysis.

In addition to the techniques mentioned above, characterization of the catalysts described in section 3.4 includes:

- Powder X-ray diffraction: determination of crystalline phases
- Inductively coupled plasma-optical emission spectroscopy: elemental analysis
- Gas pycnometry: density
- Energy-dispersive X-ray spectroscopy: elemental surface analysis

## 2.1 Small-angle X-ray diffraction

Given their wavelength of less than  $30 \text{ \AA}$ , which is in the same order of magnitude as interatomic distances of crystalline materials, X-rays can interact with matter, giving information regarding the crystallographic or structural properties of the material. When X-rays irradiate a sample, the following can occur:

- The atoms inside the sample will scatter the incident radiation in all directions
- The particles (i.e. clusters of atoms) inside the sample will produce additional scattering.

By measuring the angle-dependent distribution of scattered radiation (intensity), it is possible to draw conclusions about the average particle structure<sup>98</sup>.

X-ray diffraction (XRD) is the elastic scattering (Thompson scattering) of X-ray photons by atoms in a periodic lattice. When X-ray photons collide with electrons within the atoms and there is no energy transfer, the electrons oscillate at the same frequency as the incoming radiation, and emit radiation at the same frequency. Given that the radiation waves emitted by neighboring atoms are synchronized, coherent waves are produced that result in constructive interference (see Figure 2.1), which gives information about the particle structure that depends on the angle of observation  $2\theta$ . This scattering of waves in specific directions is represented by Bragg's law:

$$2d_{hkl} \sin \theta_{hkl} = n\lambda \quad (7)$$

Where:

d: interplanar distance of the  $hkl$  planes

$\theta$ : scattering angle of the  $hkl$  planes

n: positive integer naming the order of the reflection

$\lambda$ : wavelength of the incident wave

## 2.1 Small-angle X-ray diffraction

The scattering planes are recognized by the Miller indices  $(hkl)$ .

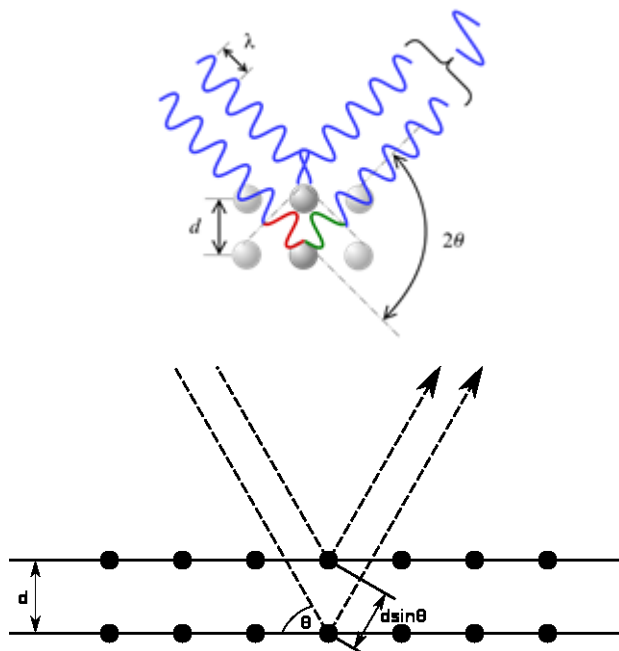


Figure 2.1 Left: Constructive interference. Right: Bragg's law of diffraction, in which two radiation waves of identical wavelength interact with two atoms within a crystalline solid and are scattered. The lower beam traverses an extra length of  $2d \sin \theta$ . Constructive interference occurs when this length is equal to an integer multiple of the wavelength of the incident radiation.

For structural crystallographic analysis on an atomic level, large  $2\theta$  values are used. Using small  $2\theta$  values (usually between  $0.1^\circ$  to  $10^\circ$ ), domains with larger dimensions can be studied, between 1 and 200 nm (small-angle X-ray diffraction, SAXRD). In this respect, this technique is useful for determining the nanoscale structure of materials, such as the periodicity of mesopores in the case of this work. With SAXRD it is possible to determine the lattice parameter

$a$ , which corresponds to the distance between the center of each pore, and the interplanar spacing  $d$  for a given orientation.

For this work, small-angle X-ray diffraction curves were obtained using a Bruker AXS D8 ADVANCE X-ray diffractometer with a Bragg–Brentano geometry equipped with a Lynx Eye 1D detector (CuK $_{\alpha}$ 1 radiation wavelength 0.15406 nm). Measurements were carried out between 0.5 and 6.0° 2 $\Theta$  value, with a step time of 1 s/0.0003° at 35 kV and 40 mA and with a 280 mm sample-detector distance. The patterns were analyzed using the Diffrac-Plus/EVA software from Bruker AXS, peaks were identified using the same software.

## 2.2 Nitrogen sorption

The adsorption of nitrogen is the standard method used to determine the specific surface area of porous materials. The relation between the amount adsorbed and the equilibrium pressure of nitrogen is known as the *adsorption isotherm*. Depending on the size and shape of the pores, the physisorption behavior varies. In the case of *micropore filling* (for pores less than 2 nm wide), physisorption takes place in one single step. In the case of mesopores (pores between 2 and 50 nm wide), physisorption is a two-step process, namely *monolayer-multilayer adsorption* and *capillary condensation*<sup>1</sup>.

Monolayer adsorption occurs when all the adsorbed molecules are in contact with the surface layer of the adsorbent, while in multilayer adsorption, the adsorption space accommodates more than one layer of molecules. After monolayer-multilayer adsorption occurs, capillary condensation takes place. Capillary condensation is unique in the fact that it occurs below the saturation pressure of the pure liquid. During this step the remaining available pore space is filled with condensate that is separated from the gas by a meniscus. This process differs from micropore filling in the fact that there is no meniscus formation in the latter<sup>1</sup>.

## 2.2 Nitrogen sorption

As was previously mentioned, sorption data is presented graphically in the form of adsorption isotherms, plotting the amount adsorbed against the equilibrium relative pressure. A classification of adsorption isotherms has been established by the International Union of Pure and Applied Chemistry (IUPAC), depicted in Figure 2.2.

Type I isotherm result from microporous solids with relatively small external surface. Type II isotherm is obtained with a non-porous or macroporous adsorbent, in this type of isotherm the point *B* indicates the stage at which monolayer coverage is complete and multilayer adsorption begins. Type III isotherms occur when there is a weak interaction between the adsorbate and adsorbent. Type IV isotherms exhibit a characteristic hysteresis loop, which is associated to capillary condensation, and also exhibits the initial monolayer-multilayer adsorption behavior. This type of isotherm is very common for many industrial adsorbents. Type V isotherm is uncommon, and is also related to weak adsorbate-adsorbent interaction. Type VI isotherm represents stepwise multilayer adsorption on a uniform non-porous surface.

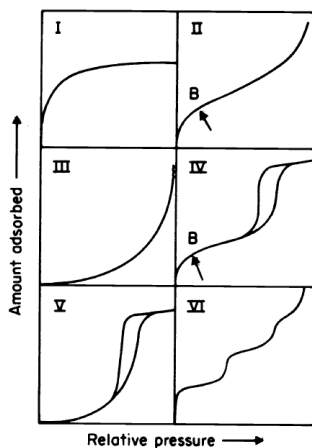


Figure 2.2 Types of adsorption isotherms as classified by IUPAC<sup>1</sup>.  
See text for details.

Information regarding the shape of the pore can be obtained from the hysteresis observed in adsorption isotherms. After monolayer-multilayer adsorption (Figure 2.3 A-C), capillary condensation occurs at a critical adsorbed film thickness, resulting in a sudden increase of the adsorbed volume. This is visible as a steep rise in the adsorption branch of the isotherm and is associated with the pore dimensions (Figure 2.3, C-D). The plateau at high relative pressure values is the result of completely filled pores with a meniscus formation at the pore opening. When desorption begins, evaporation takes place at lower relative pressures than condensation (Figure 2.3 E-F), giving way to the shape of the hysteresis loop, which is related to the pore opening.

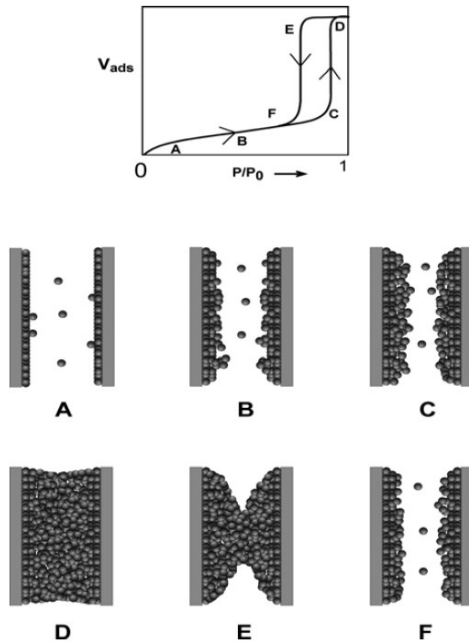


Figure 2.3 Schematic representation of multilayer adsorption, pore condensation and hysteresis in a single pore<sup>99</sup>. (A) monolayer formation, (B) multilayer adsorption, (C-D) capillary condensation, (E) pore evaporation by a receding meniscus, (F) desorption.

## 2.2 Nitrogen sorption

The types of hysteresis are shown in Figure 2.4. Type H1 and type H4 hysteresis are two extreme examples. For type H1, the two branches are almost vertical and nearly parallel over a large adsorbed volume range. This type of hysteresis is often associated with porous materials consisting of agglomerates. Type H4 exhibits branches that are nearly horizontal and parallel over a wide relative pressure range, and is associated with narrow slit-like pores. Type H2 and H3 are intermediates between these two extremes. Type H2 hysteresis is often associated with spherical pores with narrow windows or openings that connect them, or so called “ink-bottle” pores. Type H3 hysteresis is associated with aggregates of plate-like particles that give rise to slit-like pores.

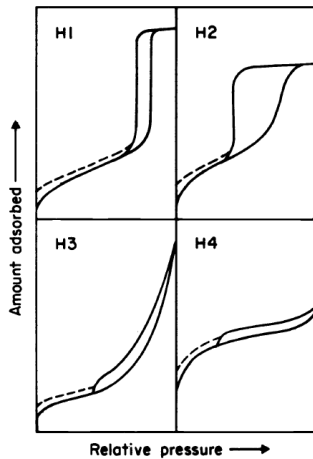


Figure 2.4 Types of hysteresis loops as classified by IUPAC<sup>1</sup>. See text for details.

### *Specific surface area*

The specific surface area can be calculated by the method of Brunauer, Emmett and Teller (BET)<sup>100</sup>, which is an extension of the Langmuir model for monolayer adsorption. The *BET specific surface area* ( $a_s$ ) is given by:

$$a_s = \frac{n_m^a \cdot L \cdot a_m}{m} \quad (8)$$

Where:

$n_m^a$ : monolayer capacity

L: Avogadro constant

$a_m$ : molecular cross-sectional area of the adsorbent (estimated at 0.162 nm<sup>2</sup> for N<sub>2</sub> at 77 K)

m: adsorbent mass

The monolayer capacity ( $n_m^a$ ) can be determined from the BET equation:

$$\frac{p}{n^a(p_0 - p)} = \frac{1}{n_m^a \cdot C} + \frac{(C-1)}{n_m^a \cdot C} \cdot \frac{p}{p_0} \quad (9)$$

Where:

p: equilibrium pressure

p<sub>0</sub>: saturation temperature at temperature of measurement

n<sup>a</sup>: amount adsorbed at the relative pressure (p/p<sub>0</sub>)

C: BET constant

The BET constant (C) is given by:

$$C = \exp \left[ \frac{E_1 - E_L}{RT} \right] \quad (10)$$

Where:

E<sub>1</sub>: heat of adsorption of the first layer

E<sub>L</sub>: heat of adsorption of subsequent layers, equal to the heat of liquefaction

R: gas constant

T: temperature

## 2.2 Nitrogen sorption

The BET equation requires a linear relation between  $p/n^a(p_0-p)$  and  $p/p_0$ , and the range of linearity is restricted to the  $p/p_0$  range between 0.05 and 0.30 (Figure 2.5).

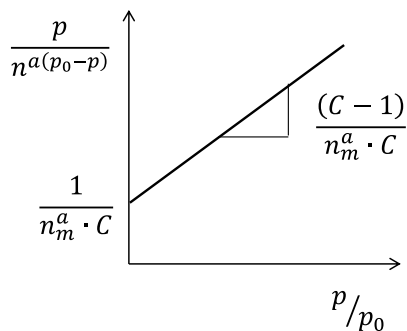


Figure 2.5 Graphical representation of the BET equation.

### *Experimental specifications*

Nitrogen sorption isotherms were recorded at 77 K on a QuadraSorb Station 4 apparatus after degassing for 10 h at 200 °C under vacuum. Surface area was determined using the BET method. Although the BJH method is widely accepted for the estimation of pore size distribution for cylindrical pores, it can underestimate the size when pores are smaller than 5 nm in diameter. For this reason, the pore size distribution determination of cylindrical mesopores was based on nonlocal density functional theory (NLDFT). Pore size distribution of micropores was also based on NLDFT calculations and was carried out only for the powder (P-COK-12, see section 3.2, Figure 3.5) and monolith (M-COK-12, see section 3.3, Figure 3.17) specimens. The calculation of the dimensions of “ink-bottle” or cage-like pores, as is the case for MCF, (type H2 hysteresis) was based on NLDFT, using the adsorption branch of the isotherm to estimate the diameter of the cage or pore cell, and the desorption (equilibrium) branch of the isotherm to determine

the diameter of the pore window (see Figure 1.6)<sup>50</sup>. All data was analyzed using the Quantachrome/QuadraWin software.

## 2.3 Scanning electron microscopy

Scanning electron microscopy (SEM) produces high-resolution images of a sample by scanning the surface with an electron beam in a raster pattern. The topographical image is constructed by analysis of the detected signal of secondary electrons emitted by atoms from the sample's surface upon the action of the high-energy electron beam.

SEM imaging is used in this work to study the morphology of the synthesized materials. Although morphology control is not one of the main focuses of this work, it is important to note the development of morphological variations with changes in the synthesis procedure. Imaging was carried out on a Zeiss Gemini Leo 1530 with integrated energy-dispersive X-ray spectroscopy (Noran System 6, Thermo Scientific). Samples were immobilized on conducting carbon pads and then sputtered with a thin layer of gold to prevent charging.

## 2.4 Transmission electron microscopy

By transmitting a beam of electrons through an ultrathin specimen (<200nm), a very high-resolution image can be obtained due to the electron-sample interaction. Part of the incident beam is transmitted, another part is dispersed and a fraction of the beam interacts with the sample giving way to a series of different responses that are useful for obtaining information about the sample, such as morphology and crystalline structure.

For TEM investigations of COK-12 materials, a small amount of the sample suspended in ethanol was placed on a TEM-grid (carbon film on 300 mesh Cu-grid, Plano GmbH, Wetzlar,

## 2.5 Powder X-ray diffraction

Germany). The samples were covered with a thin C-layer by thermal evaporation to avoid charging in the electron microscope.

A FEI Tecnai G<sup>2</sup> 20 S-TWIN transmission electron microscope (FEI Company, Eindhoven, Netherlands) equipped with a LaB<sub>6</sub>-source at 200 kV acceleration voltage was used. Images were recorded with a GATAN MS794 P CCD-camera. The microstructure (pore size and pore shape/morphology) of the samples was studied at the Department of Electron Microscopy (ZELMI), TU Berlin.

## 2.5 Powder X-ray diffraction

X-ray diffractograms were obtained using a Bruker AXS D8 ADVANCE X-ray diffractometer with a Bragg–Brentano geometry equipped with a Lynx Eye 1D detector (CoK<sub>α1</sub> radiation wavelength 0.178901 nm and CoK<sub>α2</sub> radiation wavelength 0.17929 nm). Measurements were carried out between 10 and 100° 2θ value, with a step time of 1 s/0.0096° at 35 kV and 40 mA. The patterns were analyzed using the Diffrac-Plus/EVA software from Bruker AXS and the PDF2 database.

## 2.6 Inductively coupled plasma - optical emission spectroscopy

Inductively coupled plasma - optical emission spectroscopy (ICP-OES) is a multi-elemental analytical technique used for the detection of trace metals. The sample is introduced into the equipment in liquid form and then nebulized to produce droplets which make their way into a gas plume which excites the metal atoms. Upon returning to their original state, they emit radiation which is detected and gives information on the type of metal present and its amount relative to the rest of the sample.

Inductively coupled plasma optical emission spectroscopy was carried out on a Horiba Scientific ICP Ultima2. Samples were

digested in an aqueous suspension with the addition of  $\text{HNO}_3$  and  $\text{HF}$  at  $200^\circ\text{C}$  for 5 h in an autoclave.

## 2.7 Gas pycnometry

With gas pycnometry it is possible to precisely determine the density of a sample via determination of the sample volume, regardless of the physical characteristics of the sample, by employing the principle of gas displacement and Boyle's law. The volume measured in a gas pycnometer is the amount of space within the measuring chamber that is not accessible to the gas, which is essentially the volume of the sample itself. The most common and convenient gas used is helium, due to its size and the fact that it is inert. The pycnometer consists of two chamber or cells separated by a valve; one of the cells contains the sample. Upon filling the sample cell, the pressure  $P_1$  is achieved and all pores in the sample are filled. Subsequently opening the valve releases gas into the second empty cell until the equilibrium pressure is reached<sup>101</sup>. In this sense, the density of the sample can be determined as follows:

$$\rho_s = \frac{m_s}{V_s} \quad (15)$$

Where:

$\rho_s$ : sample density

$m_s$ : mass of the sample

$V_s$ : volume of the sample

According to Boyle's law:

$$P_1 V_1 = P_2 V_2 \quad (16)$$

Applied to the system described above:

## 2.8 Energy-dispersive X-ray spectroscopy

$$P_1(V_c - V_s) = P_2(V_c + V_e - V_s) \quad (17)$$

Where:  $P_1$ : pressure in the sample cell

$P_2$ : pressure in the empty cell

$V_c$ : volume of the sample cell

$V_e$ : volume of the empty cell

Then:

$$V_s = V_c - \frac{P_2 V_e}{P_1 - P_2} \quad (18)$$

Measurements were carried out in a Micromeritics Multivolume Gas Pycnometer 1305.

## 2.8 Energy-dispersive X-ray spectroscopy

Coupled with SEM, energy-dispersive X-ray spectroscopy (EDX) is used to identify and quantify the distribution of elements on a sample by detecting X-rays emitted from the sample upon bombardment with a high-energy electron beam. Electrons are ejected from the atoms comprising the sample's surface as a result of the bombardment with high-energy electrons. The resulting electron vacancies are filled by electrons from a higher state, and an X-ray is then emitted to balance the energy difference between the two electrons' states; the energy of this X-ray is characteristic of the element from which it was emitted. The X-ray detector measures the relative abundance of emitted X-rays versus their energy.

EDX was carried out on a Zeiss Gemini Leo 1530 scanning electron microscope with integrated energy-dispersive X-ray spectroscopy (Noran System 6, Thermo Scientific). Samples were immobilized on conducting carbon pads and then sputtered with a thin layer of gold to prevent sample charging. Analysis was carried out on the Noran System Six (NSS) software.

### 3 Batch synthesis of COK-12

OMS synthesis normally requires harsh synthesis conditions such as very basic or acidic media and high temperature hydrothermal treatments. The discovery of COK-12 marked the first OMS synthesis that circumvents these conditions. The reaction takes place at room temperature and under quasi-neutral pH, and employs a more inexpensive silica source than that used for most OMS materials synthesis<sup>20</sup>.

With an aim to broaden the application possibilities of ordered mesoporous silica, investigations regarding the preparation of OMS in various macroscopic configurations have led to the fabrication of films and bulk materials (monoliths) as an alternative to powders. OMS monoliths have found applications in separation<sup>102</sup> and catalysis<sup>103</sup>. Monoliths prepared by direct synthesis have yielded mechanically stable centimeter-sized monoliths<sup>104</sup> and monoliths with a bimodal pore structure prepared by dual templating<sup>105</sup>.

The present chapter discusses the synthesis and batch upscaling of powder and monolithic COK-12. Powder COK-12 is presented as the reference material and is used as a basis for comparison in order to assess the quality of monolithic and upscaled materials in terms of pore size and mesoscale ordering. The use of powder and monolithic COK-12 as support materials in the preparation of the  $\text{Na}_2\text{WO}_4\text{-Mn/SiO}_2$  catalyst and testing in the oxidative coupling of methane reaction is also presented in this chapter. The work presented in this chapter can be found in 'Oxidative coupling of methane on the  $\text{Na}_2\text{WO}_4\text{-Mn}_x\text{O}_y$  catalyst:

### 3.1 Experimental

COK-12 as an inexpensive alternative to SBA-15<sup>3</sup>, *Catal. Commun.*, 2016, **85**, 75-78 and 'Batch and continuous synthesis upscaling of powder and monolithic ordered mesoporous silica COK-12', *Micro. Meso. Mater.*, 2018, **256**, 102-110.

## 3.1 Experimental

### 3.1.1 Reference material synthesis: powder COK-12

Powder COK-12 was synthesized according to Jammaer, et. al.<sup>20</sup>. The synthesis takes place at room temperature. In a typical synthesis, 4.0 g of the templating agent Pluronic P123 (Sigma Aldrich) were dissolved in 107.5 ml distilled water (DIW) in a covered glass beaker by stirring with a magnetic stirrer at approximately 250 rpm. After complete P123 dissolution, 3.684 g anhydrous citric acid (Roth) and 2.540 g trisodium citrate dehydrate (Roth) were added to control the synthesis pH between 4 and 5. The buffered surfactant solution was then stirred for 24 h. A solution of 10.4 g sodium silicate (Roth) and 30 ml DIW was prepared and incorporated into the buffered micellar solution. Immediate solid formation was observed, and stirring was maintained for 5 min after which the slurry was kept for 24 hours without stirring. The solid was separated from the mother liquor by vacuum filtration using a filter paper and a plastic Büchner funnel. The solid was thoroughly washed with at least 500 ml DIW, and then dried at 60°C overnight. The dry solid was then calcined at 500°C for 8 h, with a 1°C/min heating ramp, to completely remove the organic templating agent. From this point forward, COK-12 will be referred to as P-COK-12 (powder COK-12).

Table 3.1 Conditions for powder COK-12 materials synthesis.

Material	P-COK-12
Batch size	1X
P123 [g]	4.0
DIW <sup>a</sup> [ml]	107.5
Citric acid [g]	3.68
Sodium citrate [g]	2.54
Sodium silicate [g]	10.4
DIW <sup>b</sup> [ml]	30.0
HCl [ml]	-
DIW <sup>c</sup> [ml]	500

<sup>a</sup> For P123 solution

<sup>b</sup> For sodium metasilicate solution

<sup>c</sup> For washing

### 3.1.2 Monolithic COK-12 synthesis

Monolithic COK-12 (M-COK-12) was prepared following the procedure described in the previous section, albeit incorporating 6.0 ml HCl 37 % (Roth) immediately after incorporation of the sodium silicate solution.

Table 3.2 Conditions for monolithic COK-12 materials synthesis.

Material	M-COK-12
Batch size	1X
P123 [g]	4.0
DIW <sup>a</sup> [ml]	107.5
Citric acid [g]	3.68
Sodium citrate [g]	2.54
Sodium silicate [g]	10.4
DIW <sup>b</sup> [ml]	30.0
HCl [ml]	6.0
DIW <sup>c</sup> [ml]	500

<sup>a,b,c</sup> See Table 3.1

### 3.1 Experimental

#### 3.1.3 Upscaling of powder and monolithic COK-12 synthesis

Upscaling of the synthesis was carried out following the same procedure described above albeit using 25 times the quantities described in the original synthesis protocol. For this large synthesis volume, a 5 liter beaker and overhead mechanical stirring were used as a batch reactor. From this point forward, upscaled powder and monolithic COK-12 will be referred to as P-COK-12-25X and M-COK-12-25X.

Table 3.3 Synthesis conditions for upscaled COK-12 materials synthesis.

Material	P-COK-12	M-COK-12
Batch size	25X	25X
P123 [g]	100.0	100.0
DIW <sup>a</sup> [ml]	2687.5	2687.5
Citric acid [g]	92.10	92.10
Sodium citrate [g]	63.50	63.50
Sodium silicate [g]	260.0	260.0
DIW <sup>b</sup> [ml]	750.0	750.0
HCl [ml]	-	150
DIW <sup>c</sup> [ml]	12500	12500

<sup>a,b,c</sup> See Table 3.1

#### 3.1.4 Catalyst preparation and performance studies

##### 3.1.4.1 Catalyst support preparation

Three COK-12 supports were used for this study: powder COK-12, granular COK-12 produced by pressing and granular COK-12 produced by monolithic COK-12 synthesis. Powder COK-12 (P-COK-12) and monolithic COK-12 (M-COK-12) were prepared as described in section 3.1.1 and 3.1.2. Pressed COK-12 (denoted from

this point forward as GP-COK-12) was produced by pressing P-COK-12 with 35 kN force for 1 min using a 4 cm steel pressing die, and then grinding and sieving to obtain granules. Commercial silica gel (Davisil grade 636, Sigma Aldrich) is used as a fourth support, to prepare a standard catalyst for comparative purposes. A summary of the supports prepared for this study is shown in Table 3.4.

Table 3.4 COK-12 catalyst supports prepared for this study.

Support	Description
P-COK-12	Standard COK-12 powder
GP-COK-12	Standard COK-12 powder, pressed with 35 kN force for 1 min using a 4 cm steel pressing die, granulated by hand and sieved to 200-300 $\mu\text{m}$
M-COK-12	Monolithic COK-12 prepared in acidic synthesis media, the resulting material was granulated by hand and sieved to 200-300 $\mu\text{m}$
Silica gel	Commercial silica gel (Davisil grade 636, pore size 6 nm), sieved to 200-300 $\mu\text{m}$

### 3.1.4.2 Catalyst preparation

The catalysts used for this study were all prepared following the method of Fang et. al<sup>81</sup>. For all catalysts, solutions of manganese (II) nitrate tetrahydrate (Merck) and sodium tungstate dihydrate (Sigma-Aldrich) were incorporated into the support material separately via incipient wetness impregnation, in order to achieve 2.0 % Mn and 5.0 %  $\text{Na}_2\text{WO}_4$  content with respect to the final catalyst mass. After each impregnation, the catalyst was dried overnight at 100 °C and then calcined in air for 8 h at 800 °C with a 10 °C/min heating ramp in a muffle furnace.

Five catalysts were produced; the production route for each catalyst is shown in the table below. A standardized catalyst was prepared on commercial silica gel for comparison.

### 3.1 Experimental

Table 3.5 Catalysts prepared and tested throughout this study.

Catalyst	Description
P-CAT	Supported on P-COK-12
G-CAT	Supported on P-COK-12, then pressed with 35 kN force for 1 min using a 4 cm steel pressing die and granulated by hand and sieved to 200-300 $\mu\text{m}$
GP-CAT	Supported on GP-COK-12
M-CAT	Supported on M-COK-12
Silica-CAT	Supported on commercial silica gel (Davisil grade 636, pore size 6 nm), sieved to 200-300 $\mu\text{m}$

#### 3.1.4.3 Catalytic performance tests

##### *Catalytic performance tests at standard OCM conditions*

Testing was carried out in a single fixed-bed reactor using 100 mg of catalyst diluted in 1.5 ml quartz sand which is used to dissipate heat. The reaction temperature was set up at 725°C for the first 5 hours, then 750°C for 5 hours and finally 775°C for 5 hours for a total of 15 hours running time. The composition of the feed stream was fixed at  $\text{CH}_4:\text{N}_2:\text{O}_2$  of 4:4:1 with a flow rate of 60 ml/min. Synthetic air was used as the  $\text{O}_2$  source. These tests were carried out at the Chemical Reaction Engineering Group of the Technische Universität Berlin.

##### *Catalytic performance tests at lower reaction temperature*

The study of lower reaction temperatures for OCM was carried out in an 8-fold fixed bed reactor. The height of the catalyst bed was fixed at 30mm, for which 220-240 mg of catalyst were used without dilution. The composition of the feed stream was fixed at

CH<sub>4</sub>:N<sub>2</sub>:O<sub>2</sub> of 85:10:5 with a flow rate of 60 ml/min. These tests were carried out at the BASF-UniCat joint lab (BasCat).

### *Catalyst stability study*

For experiments regarding catalyst stability studies, an 8-fold fixed bed reactor was used. 100 mg of catalyst were used to form the catalyst bed without dilution. The composition of the feed stream was fixed at CH<sub>4</sub>:N<sub>2</sub>:O<sub>2</sub> of 4:4:1 with a flow rate of 60 ml/min. Reaction temperature was fixed at 750°C. These tests were carried out at the BASF-UniCat joint lab (BasCat).

## 3.2 Mesostructure and porosity of powder COK-12

Details regarding the mesostructure and porosity of the reference material powder COK-12 (P-COK-12) are presented in this section. The properties described below are used throughout this work as a basis for comparison.

### 3.2.1 Mesostructure and porosity of powder COK-12: single batch synthesis

SEM micrographs (Figure 3.1) revealed that P-COK-12 consists of agglomerates of particles roughly hexagonal in shape, with dimensions ranging between 200 and 500 nm.

The type of porous mesostructure was studied with SAXRD, in terms of pore ordering and pore-to-pore distances in periodic arrays. Most mesoporous materials are disordered at the atomic scale (amorphous), and their XRD patterns result from the periodicity of mesopore arrays. In contrast to single crystals, the diffraction angles for mesoporous materials are small, due to the larger unit cells. Most SAXRD patterns of mesoporous materials

### 3.2 Mesostructure and porosity of powder COK-12

exhibit only one intense peak, with several broad peaks. These peaks are used as a fingerprint to identify the mesostructure.

In the case of COK-12, which has 2D hexagonal  $p6m$  symmetry, the position ( $2\theta$  value) of the first three peaks follows the relation  $1:\sqrt{3}:2$ . Figure 3.2 shows the SAXRD pattern for as-calcined P-COK-12. Three clear peaks are visible, which were indexed as the (100), (110) and (200) peaks, with  $2\theta_{100} = 1.052^\circ$ ,  $2\theta_{110} = 1.800^\circ$  and  $2\theta_{200} = 2.039^\circ$ , which satisfies the relation for  $p6m$  hexagonal symmetry.

With this information, the interplanar spacing  $d$  between the (100) family of planes and the lattice parameter  $a$  were determined by means of Bragg's law (equation 7) and the known relationship between  $d$  and the hexagonal crystal system (equation 12)<sup>50</sup>:

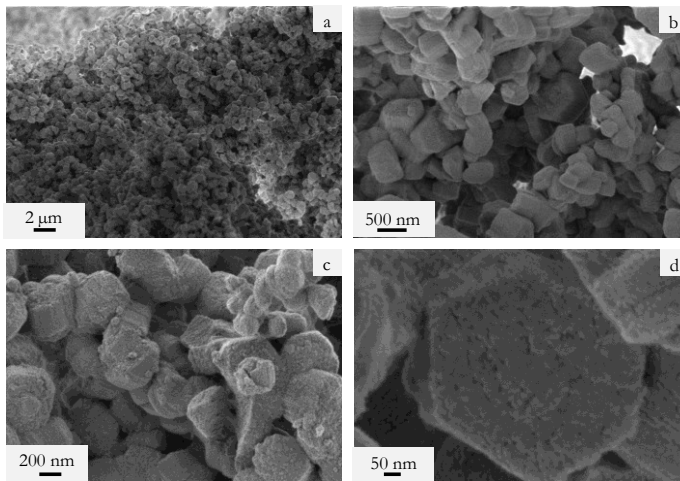


Figure 3.1 SEM micrographs of as-calcined P-COK-12. P-COK-12 consists of agglomerates of hexagonal plate-like particles that range from 200 to 500 nm in size.

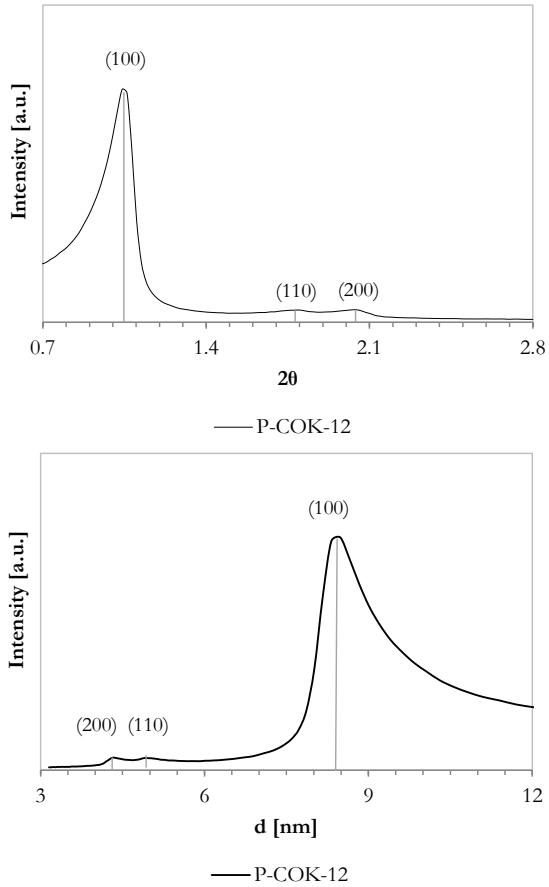


Figure 3.2 Left: SAXRD pattern of as-calcined P-COK-12-25X. Three peaks corresponding to  $p6m$  hexagonal symmetry are indexed, indicating long-range ordering. Right: d-spacing,  $d_{100}=8.39$  nm,  $d_{110}=4.91$  nm and  $d_{200}=4.32$  nm.

### 3.2 Mesostructure and porosity of powder COK-12

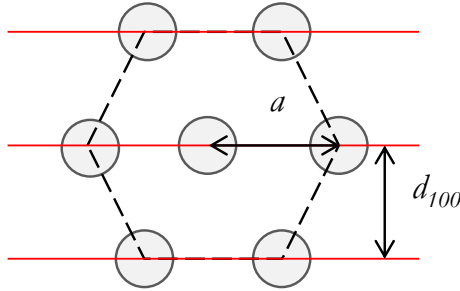


Figure 3.3 Schematic illustration of a 2D hexagonal  $p6m$  symmetry for COK-12. The circles represent pores. The red lines correspond to the (100) family of planes. The lattice parameter  $a$  corresponds to the distance between pore centers, and the interplanar spacing  $d_{100}$  to the distance between the (100) family of planes.

The  $d_{100}$  spacing then is:

$$2d_{100} \sin \theta_{100} = n\lambda$$

With:

$$n = 1$$

$$\lambda = 0.15406 \text{ nm}$$

$$2\theta_{100} = 1.052^\circ$$

Then:

$$d_{100} = 8.39 \text{ nm}$$

The lattice parameter  $a$  for a hexagonal crystal system was calculated by:

$$\frac{1}{d_{hkl}^2} = \frac{4}{3} \frac{h^2 + hk + k^2}{a^2} + \frac{l^2}{c^2} \quad (12)$$

With:

$$d_{hkl} = d_{100} = 8.39 \text{ nm}$$

$$h = 1$$

$$k = 0$$

$$l = 0$$

Then:

$$a = 9.69 \text{ nm}$$

In combination with TEM (see Figure 3.4), the periodicity and hexagonal ordering of the pores of P-COK-12 was confirmed. The pore diameter and wall thickness estimated by TEM are 5.0 nm and 3.9 nm, respectively. The distance between pore centers is approximately 9.8 nm, which is in agreement with the lattice parameter  $a$  calculated with SAXRD data. Furthermore, TEM images revealed an overview of the shape of the particles (Figure 3.4 a,b), which are hexagonal in shape with defined edges. The distribution of the pores from a longitudinal point of view is shown in Figure 3.4 e.

By nitrogen sorption analysis, further information regarding the pore shape, pore size distribution, pore volume and specific surface area was obtained. Figure 3.5 shows the adsorption-desorption isotherm of as-calcined P-COK-12. The isotherm is a type IV isotherm with a type H1 hysteresis. This graphical overview reveals that the porous structure of P-COK-12 consists of an array of open cylindrical mesopores with a very narrow pore size distribution, confirmed by the steep adsorption branch of the hysteresis loop which indicates that capillary condensation occurs at a small relative pressure range. The specific surface area as determined by the BET method is 647.7 m<sup>2</sup>/g. The mean pore size distribution as determined by NLDFT is 6.1 nm (Figure 3.6). The pore volume estimated by NLDFT is 0.640 cc/g. The mesopore size distribution is in accordance with that estimated graphically by TEM.

### 3.2 Mesostructure and porosity of powder COK-12

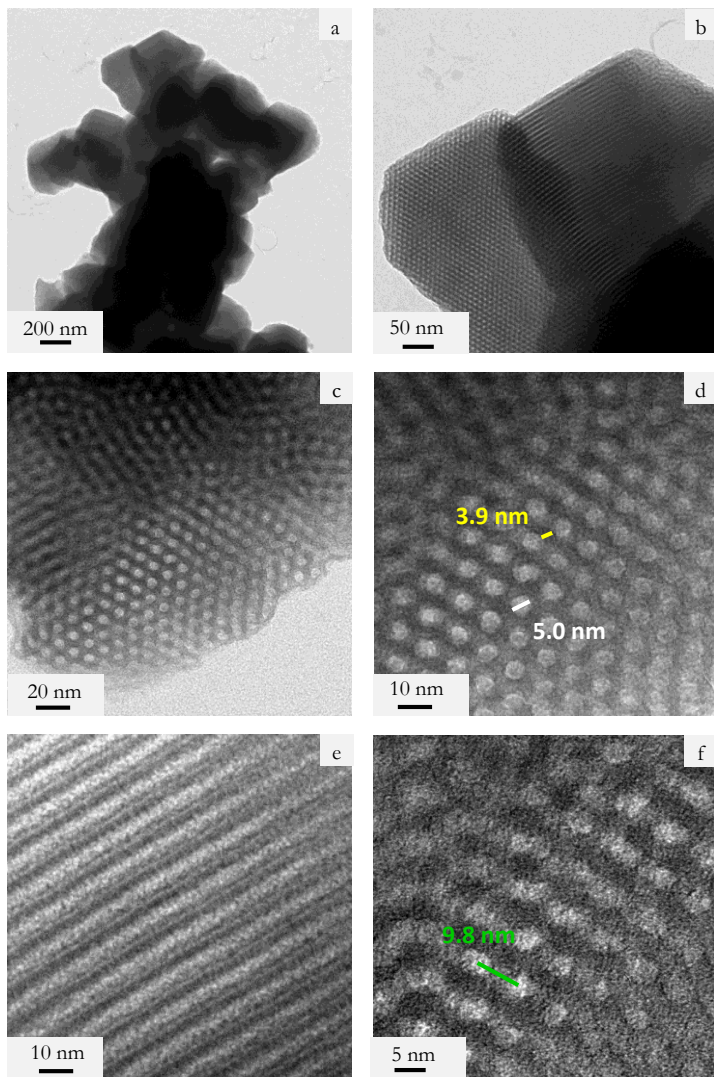


Figure 3.4 TEM micrographs of as-calcined P-COK-12. The shape of the particles as well as long-range 2D pore ordering can be seen in (a) and (b); (c) view from the top of the pores, (d) pore size (white, 5.0 nm) and wall thickness (yellow, 3.9 nm), (e) pore size, lateral view of cylindrical mesopores, (f) distance between pores (9.8 nm).

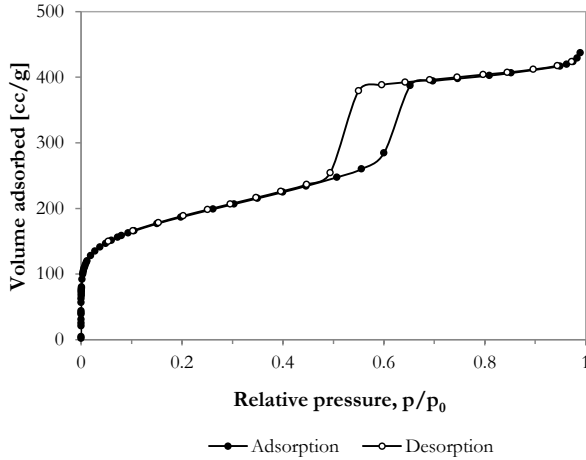


Figure 3.5 Nitrogen adsorption-desorption isotherm for as-calcined P-COK-12 with microporosity region. The isotherm is a type IV with H1 hysteresis, characteristic of mesoporous materials.

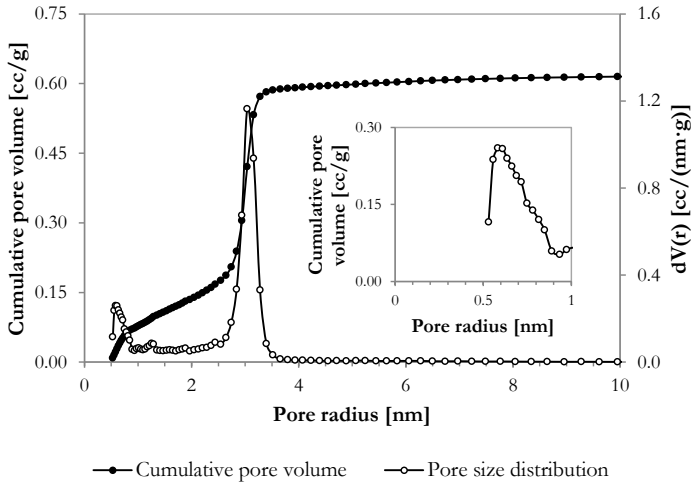


Figure 3.6 Pore size distribution of as-calcined P-COK-12 as determined by the NLDFT method, revealing a pore radius of 3.0 nm. Inlet: pore size distribution of micropores, with a 0.6 nm radius.

### 3.2 Mesostructure and porosity of powder COK-12

It is noteworthy to comment on the microporosity of COK-12, which has been previously reported<sup>20,63</sup>. In Figure 3.5, the initial gas uptake at low relative pressure indicates the presence of micropores, which was confirmed by the dual pore size distribution observed in Figure 3.6. There is a peak at the corresponding pore diameter of 1.2 nm (Figure 3.6 inset), which is in accordance to that reported by Imperor-Clerc et. al for SBA-15 and analogous to COK-12, given that both materials are templated with P123<sup>106</sup>. They report the presence of a “corona” region that includes condensed silica and also the hydrophilic PEO tails of the templating agent P123, which upon calcination produce micropores within the silica walls. The microporosity of P-COK-12 represents 12 % of the total pore volume, or 0.083 cc/g of a total of 0.640 cc/g.

#### 3.2.2 Mesostructure and porosity of powder COK-12: upscaled batch synthesis

The powder COK-12 synthesis was upscaled to 25 to determine if any changes in the mesostructure of the material occur. SAXRD (Figure 3.7) revealed three peaks which were indexed as the (100), (110) and (200) reflections, with  $2\theta_{100} = 1.052^\circ$ ,  $2\theta_{110} = 1.756^\circ$  and  $2\theta_{200} = 2.075^\circ$ , which satisfies the relation for  $p6m$  hexagonal symmetry.

The periodicity and hexagonal ordering of the pores of P-COK-12-25X were confirmed with TEM (Figure 3.8). The pore diameter, wall thickness and distance between pore centers estimated by TEM were 5.3 nm, 3.4 nm and 9.8, nm respectively. This is in agreement with the lattice parameter  $a$  (see

Table 3.6). As for P-COK-12, the particle shape observed in TEM micrographs is hexagonal shape with defined edges (Figure 3.8 a,b).

Figure 3.9 shows the adsorption isotherm for P-COK-12-25X. As in the case of P-COK-12, the isotherm is a type IV isotherm with a type H1 hysteresis, indicating open cylindrical

mesoporosity with a narrow pore size distribution. The specific surface area as determined by the BET method is 599.8 m<sup>2</sup>/g. The NLDFT (Figure 3.10) pore diameter is 6.6 nm. The pore volume as estimated by NLDFT is 0.626 cc/g, which is in line with that of P-COK-12.

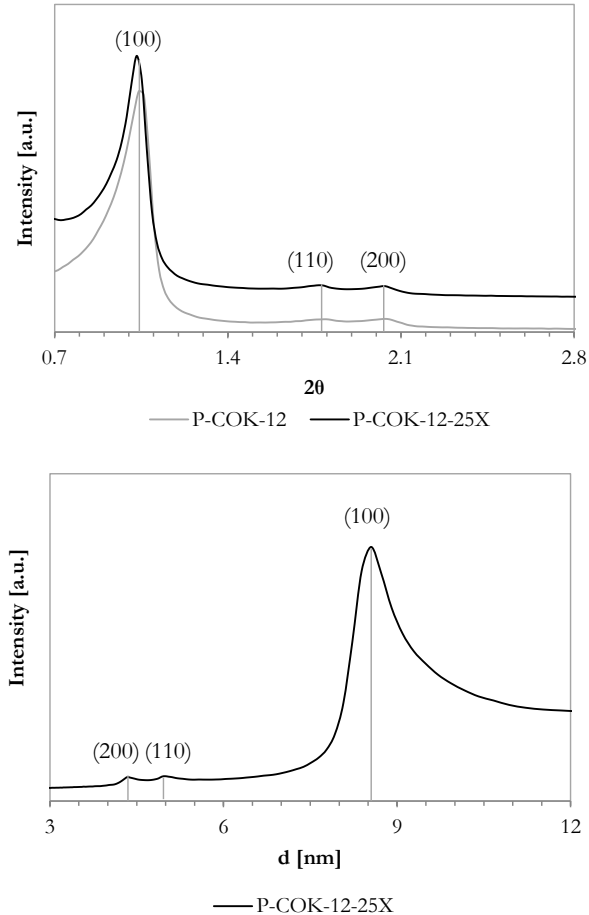


Figure 3.7 Top: SAXRD pattern of as-calcined P-COK-12-25X. Three peaks corresponding to  $p6m$  hexagonal symmetry are indexed. Patterns have been normalized to the (100) peak and shifted for

### 3.2 Mesostructure and porosity of powder COK-12

comparison, P-COK-12 pattern is shown for comparison. Bottom: d-spacing,  $d_{100}=8.39$  nm,  $d_{110}=4.97$  nm,  $d_{200}=4.32$  nm.

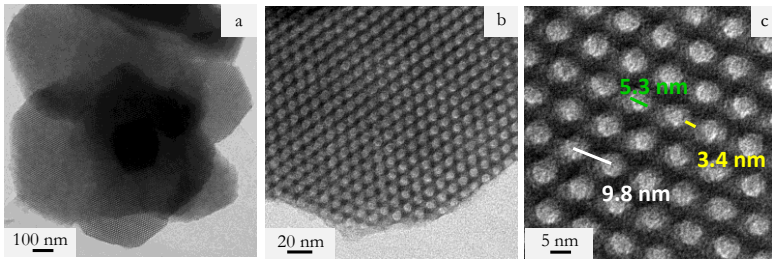


Figure 3.8 TEM micrographs of as-calcined P-COK-12-25X at different magnifications. The shape of the particles as well as long-range 2D hexagonal pore ordering can be seen in (a), (b) view from the top of the pores, (c) pore size (green, 5.3 nm), wall thickness (yellow, 3.4 nm) and distance between pores (white, 9.8 nm).

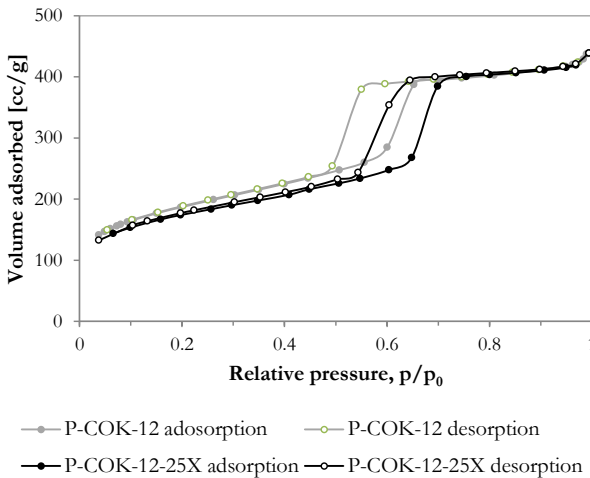


Figure 3.9 Nitrogen adsorption-desorption isotherm for as-calcined P-COK-12-25X. The isotherm is a type IV with H1 hysteresis, characteristic of mesoporous materials. P-COK-12 isotherm is shown for comparison.

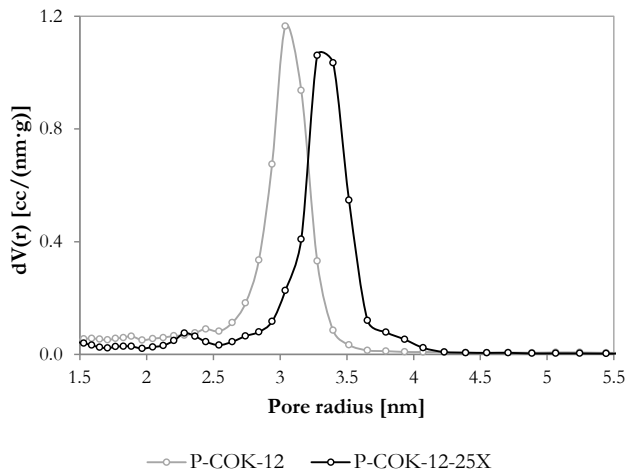


Figure 3.10 Pore size distribution of as-calcined P-COK-12-25X as determined by the NLDFT method, revealing a pore radius of 3.3 nm. Pore size distribution of P-COK-12 is shown for comparison. Data shown in the relevant pore size range.

Table 3.6 summarizes the properties of P-COK-12 and P-COK-12-25X. Powder COK-12 is presented as the reference material and is used as a basis for comparison in order to determine the quality of monolithic and upscaled materials in terms of pore size and mesoscale ordering.

Upon comparison of the results obtained for P-COK-12 and the upscaled P-COK-12-25X, no significant change in the properties of the material from larger-scale batch production was observed and production of up to 65 g was achieved. The successful and facile upscaling of P-COK-12 can be attributed to two factors:

(i) mixing is not critical in COK-12 synthesis. Normally, mixing is crucial in OMS synthesis, for example for particle morphology control<sup>107</sup> and to produce high quality materials using an inexpensive silica precursor<sup>108</sup>. However, obtaining the same mixing performance by using geometric similarity in small and large scale is very difficult, if not impossible. For similar mixer geometries

### *3.2 Mesostructure and porosity of powder COK-12*

that differ only in scale, a number of macro and micro-scale phenomena occur that result in differences in flow pattern. For example the Reynolds numbers in the large tank will be higher, typically 5 to 25 times higher than in a small tank and the energy dissipation per unit volume around the impeller is much higher than in the rest of the tank<sup>109</sup>. For COK-12, however, Jammaer et. al. proposed that the material forms upon reaching a minimum silica content and not due to mixing. As was discussed in section 1.3.5, the limited degree of cross-linking of the silicate network in the PEO shells of P123-silica micelles produces flexible micelles, due to the strong PEO-silicate oligomer interaction. This flexibility in the micelle shells allows for fast aggregation and growth with increasing silica content. For this thesis, in the case of P-COK-12-25X synthesis, the use of an overhead mechanical stirrer was sufficient for mixing of the reagents and producing a highly ordered uniform material.

(ii) the fact the synthesis takes place at room temperature implies that heat transfer is unnecessary. Any issues that arise from poor heat transfer in a larger volume, such as temperature gradients between the fluid nearest to the heat source and other parts of the fluid, are circumvented by room temperature synthesis.

The absence of the necessity of mixing and temperature control allows for the facile upscaling of powder COK-12, which has two main benefits: (i) a large amount of material with consistent properties can be synthesized and (ii) the synthesis of larger batches is less expensive. For studies requiring large amounts of OMS, consistent OMS properties must be ensured throughout to avoid introducing more variables into the study. This is achieved by synthesizing large quantities in a single batch. Furthermore, the production of a single large-scale batch is less expensive than producing multiple small-scale batches. Larger-scale OMS synthesis methods are necessary in order to develop OMS applications on an industrial scale.

Table 3.6 Properties of as-calcined P-COK-12 and P-COK-12-25X. Upscaling of the synthesis up to 25 times did not produce significant changes in the properties of the material.

Material	P-COK-12	P-COK-12 -25X
Mass <sup>a</sup> [g]	2.5	65.0
d <sub>100</sub> <sup>b</sup> [nm]	8.39	8.39
a <sup>c</sup> [nm]	9.69	9.69
P <sub>TEM</sub> <sup>d</sup> [nm]	5.0	5.3
W <sub>TEM</sub> <sup>e</sup> [nm]	3.9	3.4
Type <sup>f</sup>	IV	IV
H <sup>g</sup>	H1	H1
P <sub>DFT</sub> <sup>h</sup> [nm]	6.1	6.6
V <sub>DFT</sub> <sup>i</sup> [cc/g]	0.640	0.626
S <sub>BET</sub> <sup>j</sup> [m <sup>2</sup> /g]	647.7	599.8

<sup>a</sup> Final mass of as-synthesized material

<sup>b</sup> Interplanar distance between (100) planes estimated by SAXRD

<sup>c</sup> Lattice parameter estimated by SAXRD

<sup>d</sup> Pore diameter estimated by TEM

<sup>e</sup> Wall thickness estimated by TEM

<sup>f</sup> Type of isotherm

<sup>g</sup> Type of hysteresis

<sup>h</sup> Pore diameter estimated by NLDFT

<sup>i</sup> Pore volume estimated by NLDFT

<sup>j</sup> Specific surface area estimated by BET

### 3.3 Mesostructure and porosity of monolithic COK-12

Processes that require the use of larger particulate OMS drove the need to produce a material with particles within the micron range, as opposed to powders. For this reason, the synthesis and upscaling of monolithic COK-12 was studied in this work, by acidification of the original synthesis method. The synthesis takes place at room temperature, using a buffered aqueous solution of P123 as a templating agent and sodium silicate as a silica precursor, with acidification by incorporating HCl immediately after sodium silicate. The solution was aged for 24 hours, after which a compact gel was formed which was then filtered, washed, dried and calcined in the

### 3.3 Mesostructure and porosity of monolithic COK-12

same way as P-COK-12. Applications of M-COK-12 as a catalyst support are presented in section 3.4.

Due to acidification of the synthesis medium, a compact gel was formed which held the shape of the container after the required synthesis aging time of 24 h, however shrunken (i.e. it does not touch the sides of the container, see Figure 3.11 right). Transferring of the gel to the plastic Büchner funnel used for filtration resulted in breaking of the gel, and washing induced further breakage. After drying and calcination to remove the organic template, irregular hard particles ranging from a few micrometers to centimeters in size were obtained, as shown in Figure 3.12 (right).



Figure 3.11 P-COK-12 slurry (left) and M-COK-12 gel (middle and right) after aging for 24 h.



Figure 3.12 Macroscopic morphology of as-calcined P-COK-12 (left, fine powder) and as-calcined M-COK-12 (right, large hard irregular particles with a broad size distribution).

SEM micrographs (Figure 3.13) revealed that the morphology of M-COK-12 consists of an agglomerate of rod-like

particles similar to fibrous SBA-15<sup>110</sup>, with a diameter of 100-250 nm for the sub particles and over 500 nm for the agglomerates. The particles are about 2.5  $\mu\text{m}$  in length. The acidification of the synthesis media can promote crosslinking and therefore particle growth; the plate-like particles obtained for P-COK-12 grow in the direction of the pores, resulting in particles with a similar hexagonal shape with longer channels (2.5  $\mu\text{m}$  for M-COK-12 vs. 250 nm for P-COK-12, Figure 3.1).

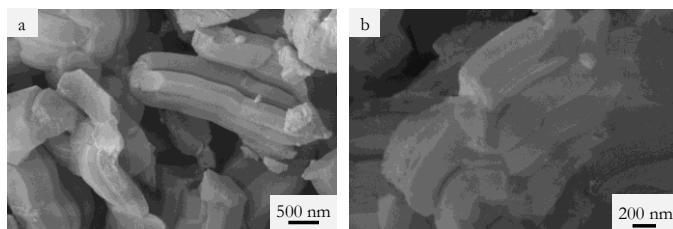


Figure 3.13 SEM micrographs of as-calcined M-COK-12 reveal the rod-like morphology of particles up to 2.5  $\mu\text{m}$  in length.

SAXRD (Figure 3.14) patterns of the original and upscaled M-COK-12 materials revealed three peaks which were indexed as (100), (110) and (200) reflections. Upscaling of the synthesis to 25 times had no effect on the long-range ordering of this material.

The periodicity and hexagonal ordering of the pores of M-COK-12 materials were confirmed with TEM (Figure 3.15). The pore diameter, wall thickness and distance between pore centers of M-COK-12 estimated by TEM were 6.5, 3.8 and 10.3 nm respectively. For this thesis, the M-COK-12 batch synthesis was upscaled 25 times, yielding up to 65 g of material with a uniform pore size distribution of 6.1 nm. In contrast, the M-COK-12 synthesis yields approximately 2.5 g of M-COK-12.

For M-COK-12-25X, the pore diameter, wall thickness and distance between pore centers determined by TEM were 5.1, 3.1 and 8.2 nm, respectively. These values are in agreement with the lattice parameters  $a$  calculated with SAXRD data (Table 3.8) and are within the expected range for materials templated with P123 under

### 3.3 Mesostructure and porosity of monolithic COK-12

the aforementioned synthesis conditions. As is the case for P-COK-12, the particle shape corresponds to a hexagonal shape with defined edges (Figure 3.15 c).

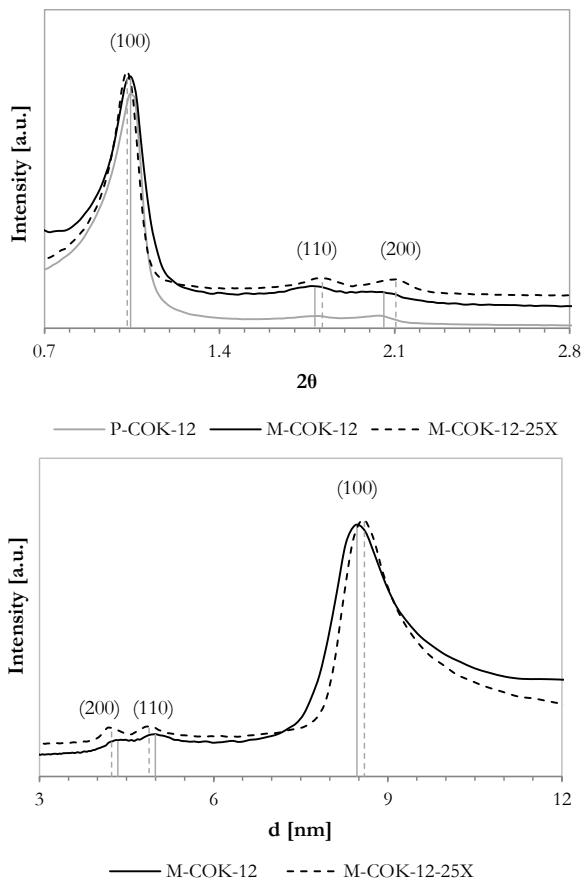


Figure 3.14 Top: SAXRD patterns of as-calcined M-COK-12 and M-COK-12-25X. Three peaks corresponding to  $p6m$  hexagonal symmetry are indexed. Patterns have been normalized to the (100) peak and shifted for comparison, Bottom: d-spacing for M-COK-12  $d_{100}=8.23$  nm,  $d_{110}=5.06$  nm,  $d_{200}=4.43$  nm; for M-COK-12-25X  $d_{100}=7.52$  nm,  $d_{110}=4.83$  nm,  $d_{200}=4.17$  nm.

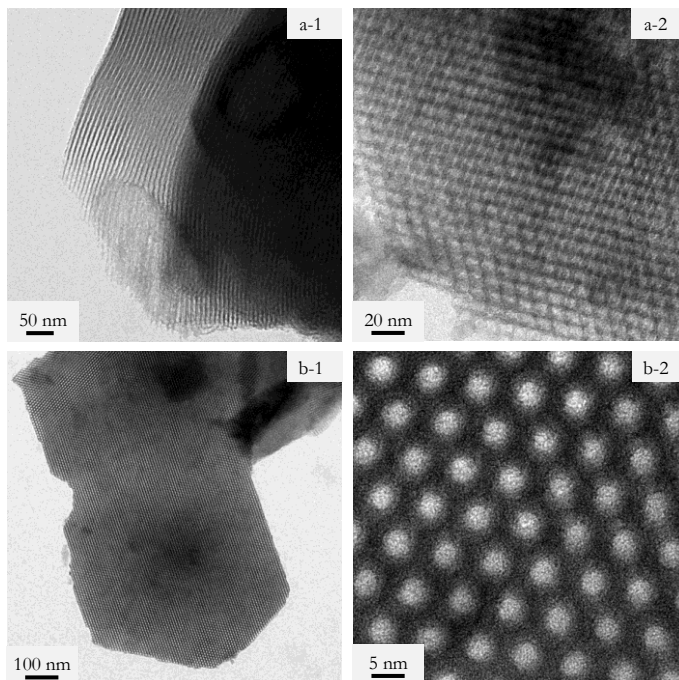


Figure 3.15 (a) TEM of as-calcined M-COK-12. Pore diameter, wall thickness and distance between pore centers are 6.5, 3.8 and 10.3 nm respectively (b) TEM of as-calcined M-COK-12-25X. Pore diameter, wall thickness and distance between pore centers are 5.1, 3.1 and 8.2 nm, respectively.

$N_2$  adsorption analysis (Figure 3.16) revealed that the adsorption isotherm of M-COK-12 and M-COK-12-25X are type IV isotherms with type H1 hysteresis, indicating open cylindrical mesoporosity with a narrow pore size distribution, as is expected. The specific surface areas determined by the BET method are  $346.83 \text{ m}^2/\text{g}$  for M-COK-12 and  $439.5 \text{ m}^2/\text{g}$  for M-COK-12-25X. This significant decrease in surface area with respect to that of P-COK-12 was attributed to a decrease in the contribution of microporosity to the overall surface area, evident in the shift of the isotherms to lower values of adsorbed volume at a low relative pressure range (Figure 3.17, detail of micropore region). The loss of

### 3.3 Mesostructure and porosity of monolithic COK-12

microporosity in M-COK-12 materials is likely due to the formation of a compact gel after aging. Washing of M-COK-12 compact gels is less effective than washing of powders, resulting in higher concentration of residual sodium from the silica source and the buffer solution (Table 3.7). Upon calcination, the residual sodium ions may migrate into the amorphous silica matrix and produce a phase transformation, which in turn results in the collapse of smaller pores.

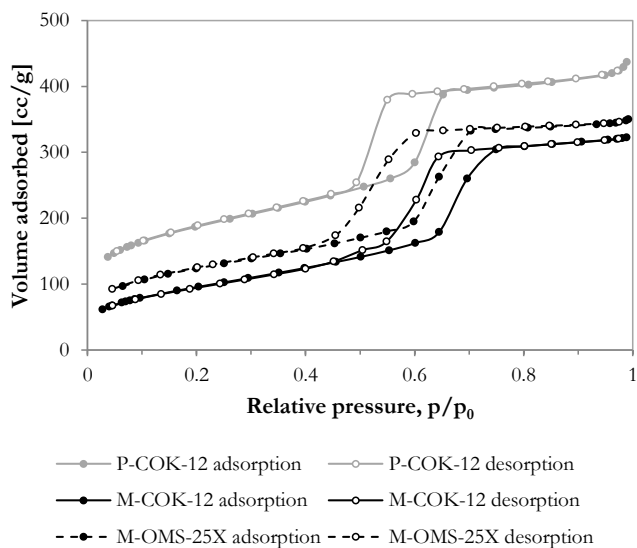


Figure 3.16 Nitrogen adsorption-desorption isotherms for as-calcined M-COK-12 and M-COK-12-25X. The isotherms are type IV with H1 hysteresis, characteristic of mesoporous materials. P-COK-12 isotherm is shown for comparison.

Table 3.7 Sodium content in relation to silica of P-COK-12 and M.COK-12 determined by ICP-OES.

Material	mol Na/mol Si
P-COK-12	0.002
M-COK-12	0.051

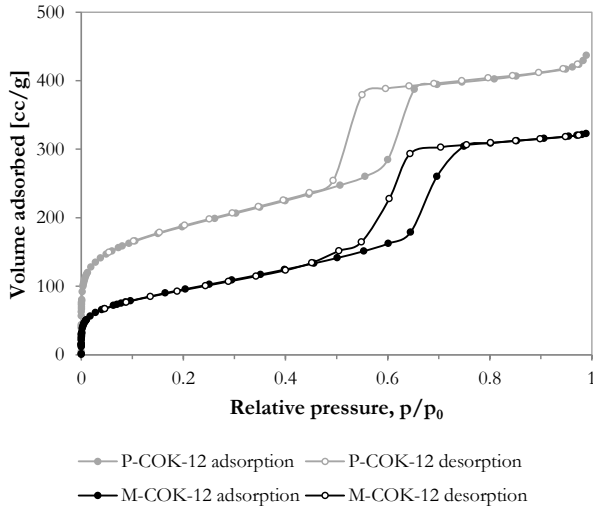


Figure 3.17 Detail of micropore region of nitrogen adsorption-desorption isotherm of as-calcined M-COK-12. P-COK-12 isotherm is shown for comparison. A loss in microporosity is observed evidenced by a lower uptake of nitrogen in the low relative pressure range.

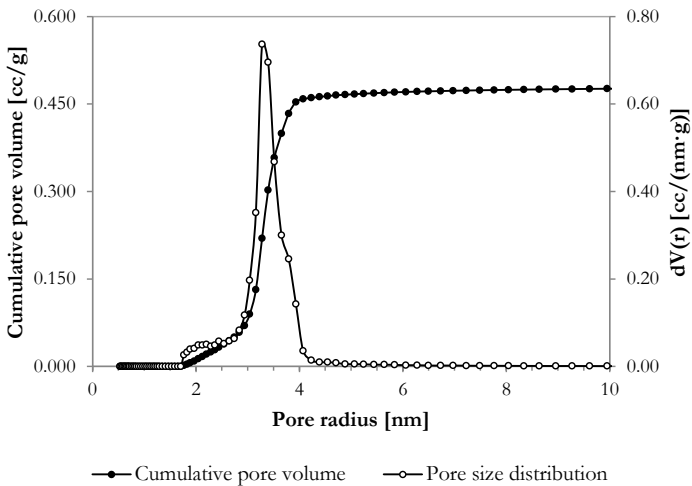


Figure 3.18 Pore size distribution of as-calcined M-COK-12 as determined by the NLDFT method, revealing a pore radius of 3.3 nm.

### 3.3 Mesostructure and porosity of monolithic COK-12

Figure 3.18 shows the pore size distribution of M-COK-12, confirming the absence of micropores. The NLDFT pore diameters of M-COK-12 and M-COK-12-25X are 6.6 and 6.1 nm, respectively. The pore volume of M-COK-12 and M-COK-12-25X are 0.483 and 0.520 cc/g, respectively. The decrease in pore volume with respect to P-COK-12 is due to the absence of micropores in M-COK-12 materials (Table 3.8).

It is worthwhile discussing the impact of the loss of microporosity, specifically in materials templated with P123. Smith, et. al.<sup>111</sup> conducted a study regarding the catalytic behavior of vanadia supported on SBA-15. The microporosity of SBA-15, referred to as surface roughness, was eliminated by a two-step calcination at 600° and then 700° or 850 °C to yield a smooth surface. They proposed that surface roughness results in differences in the local density of surface hydroxyl groups of SBA-15, which in turn results in the formation of different vanadia species with different catalytic behavior. Therefore, the direct synthesis of an OMS material such as M-COK-12 could be promising for such applications. The second calcination step is unnecessary, and large particles are obtained without post-processing, which is desirable for larger-scale catalytic applications.

Table 3.8 Properties of as-calcined M-COK-12 and M-COK-12-25X presented in comparison to P-COK-12.

Material	P-COK-12	M-COK-12	M-COK-12-25X
Mass <sup>a</sup> [g]	2.5	2.2	60.0
d <sub>100</sub> <sup>b</sup> [nm]	8.39	8.23	7.52
a <sup>c</sup> [nm]	9.69	9.50	8.68
P <sub>TEM</sub> <sup>d</sup> [nm]	5.0	6.5	5.1
W <sub>TEM</sub> <sup>e</sup> [nm]	3.9	3.8	3.1
Type <sup>f</sup>	IV	IV	IV
H <sub>g</sub>	H1	H1	H1
P <sub>DFT</sub> <sup>h</sup> [nm]	6.1	6.6	6.1
V <sub>DFT</sub> <sup>i</sup> [cc/g]	0.640	0.483	0.520
S <sub>BET</sub> <sup>j</sup> [m <sup>2</sup> /g]	647.7	346.8	439.5

<sup>a-j</sup> See Table 3.6

Table 3.8 summarizes the properties of M-COK-12 and M-COK-12-25X in comparison to the standard P-COK-12. Powder COK-12 is presented as the reference material and is used as a basis for comparison in order to determine the quality of monolithic and upscaled materials in terms of pore size and mesoscale ordering.

In this study, the decision to produce large ordered mesoporous silica particles was driven by the necessity of larger particles (as opposed to powder) to use as a catalyst support for the oxidative coupling of methane. Ordered mesoporous silica monoliths have been previously prepared either by direct synthesis<sup>105,112</sup> or by post-synthesis processing of OMS powders<sup>12,113</sup>, yielding monoliths with defined shapes that, unless stabilized by encapsulation with polymeric networks<sup>114,115</sup> or physical barriers (inside HPLC columns<sup>102</sup>, for example), are fragile and can crack easily. The shape of monolithic COK-12 was irrelevant for the present study, given that irregular particles are acceptable for use as a catalyst support as long as they are within the desired particle size range.

It is well established that acidification of the synthesis of silica materials prepared with sodium silicate promotes cross-linking and gel formation<sup>116</sup>. Enhanced crosslinking under acidic media could be responsible for the formation of stable agglomerates of M-COK-12 particles. It has been demonstrated that at low pH, the polycondensation rate of orthosilicic acid (which is the silica precursor to COK-12) decreases with decreasing pH<sup>117</sup>. This decrease in the polycondensation rate and therefore relatively faster hydrolysis rate results in more availability of reactive -OH groups, which in turn promotes further polycondensation resulting in particle growth during aging.

In addition to the formation of centimeter-sized particles, it is important to discuss the growth of M-COK-12 primary particles in comparison to P-COK-12 primary particles. Under normal synthesis conditions, the formation of COK-12 occurs immediately upon mixing the sodium silicate solution and the buffered P123 solution. Acidification with HCl directly after mixing the sodium

### 3.4 COK-12 as a catalyst support for the oxidative coupling of methane

silicate and P123 solution appears to promote particle growth in the direction parallel to the pores, as seen in Figure 3.13. P-COK-12 (Figure 3.1) exhibits a plate-like structure with pores  $\sim 250$  nm in length, which corresponds to the thickness of the particles. However, the primary particles of M-COK-12 have pores up to  $2.5\mu\text{m}$  in length, while maintaining the same pore diameter and high degree of ordering. These primary particles in turn agglomerate, forming hard particles up to centimeter sizes. A study regarding the morphologies of large pore periodic mesoporous organosilicas<sup>118</sup> gives some insight into the possible formation mechanism of M-COK-12. This study suggests the formation of silica-P123 seeds upon mixing the reagents, which aggregate to form nuclei. The nuclei continually grow due to polycondensation, with preferential growth on the long axis of the particle (parallel to the pores). This preferential growth along the long axis was attributed to severe passivation of hydroxyl groups at the surface of the particle as opposed to at the ends of the particle, where the hydroxyl groups are relatively shielded from the acid by the P123 micelles. As a result, growth along the long axis was able to proceed for a longer time resulting in particles with long major axes.

Upon comparison of the results obtained for M-COK-12 and the upscaled M-COK-12-25X, no significant change in the properties of the material from larger-scale batch production was observed and production of up to 60 g was achieved. The successful and facile upscaling of P-COK-12 can be attributed to the nonessential mixing and temperature control, as discussed in the previous section.

## 3.4 COK-12 as a catalyst support for the oxidative coupling of methane

In this work, COK-12 has been used as a catalyst support for the  $\text{Na}_2\text{WO}_4\text{-Mn/SiO}_2$  system for the oxidative coupling of methane reaction (OCM)<sup>119</sup>. Catalyst characterization before and after OCM

is presented in this section, as well as a study of the catalytic performance in a fixed bed reactor. Three different COK-12 supports are studied: powder COK-12 (see section 3.2), granular COK-12 produced by monolithic COK-12 synthesis (see section 3.3) and granular COK-12 produced by pressing (presented here).

### 3.4.1 Catalyst composition and structure

#### 3.4.1.1 Catalyst structure before OCM

##### *Pressed COK-12 mesostructure*

SEM micrographs (Figure 3.19) indicated that pressing produces breakage of the P-COK-12 particles. There is evidence of hexagonal plate-like particles characteristic of P-COK-12, as well as scattered residues that are the result of crushing at high pressure.

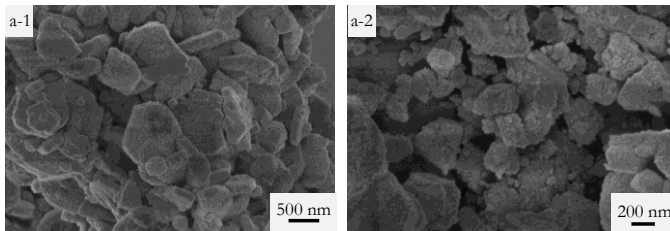


Figure 3.19 SEM micrographs of as-pressed GP-COK-12. Breakage of hexagonal P-COK-12 particles occurs due to pressing (a-2).

SAXRD (Figure 3.20) patterns of GP-COK-12 revealed three peaks which were indexed as (100), (110) and (200) reflections. The intensity of (110) and (200) reflections is lower in comparison to those of P-COK-12, indicating a loss of long-range ordering, probably due to the collapse of pores as a result of pressing, which is visible in TEM micrographs of GP-COK-12 (Figure 3.21 c).

### 3.4 COK-12 as a catalyst support for the oxidative coupling of methane

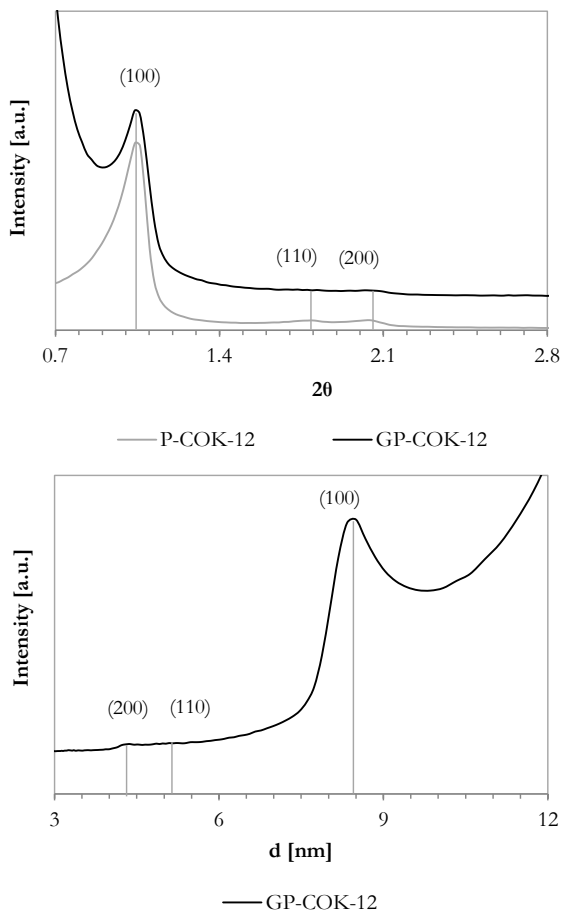


Figure 3.20 Left: SAXRD pattern of as-pressed GP-COK-12. Three peaks corresponding to  $p6m$  hexagonal symmetry are indexed.

Patterns have been normalized to the (100) peak and shifted for comparison, P-COK-12 pattern is shown for comparison. Right: d-spacing  $d_{100}=8.70$  nm,  $d_{110}=5.1$  nm,  $d_{200}=4.32$  nm.

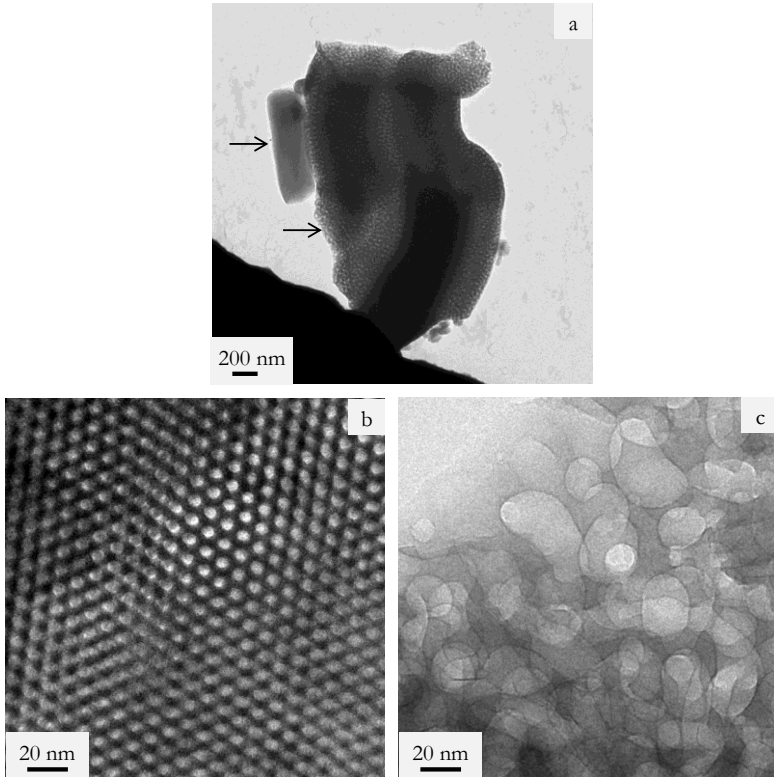


Figure 3.21 TEM micrographs of as-pressed GP-COK-12 showing (a) ordered (top arrow) and disordered (bottom arrow) regions, (b) ordered region (c) loss of ordering due to pressing.

$N_2$  adsorption analysis (Figure 3.22) revealed that GP-COK-12 exhibits a type IV isotherm with type H1 hysteresis. The specific surface area determined by the BET method is  $579.2 \text{ m}^2/\text{g}$ , with a pore diameter of 6.6 nm and a pore volume of  $0.536 \text{ cc/g}$ . A decrease in pore volume and surface area were observed for GP-COK-12, with an increase in the mean pore size distribution, which are all attributed to the collapsed pores (Figure 3.23).

### 3.4 COK-12 as a catalyst support for the oxidative coupling of methane

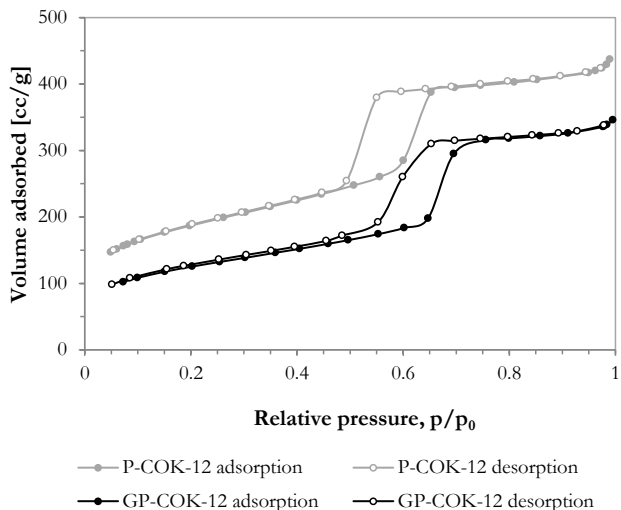


Figure 3.22 Nitrogen adsorption-desorption isotherm of as-pressed GP-COK-12. The isotherm is a type IV with H1 hysteresis, characteristic of mesoporous materials.

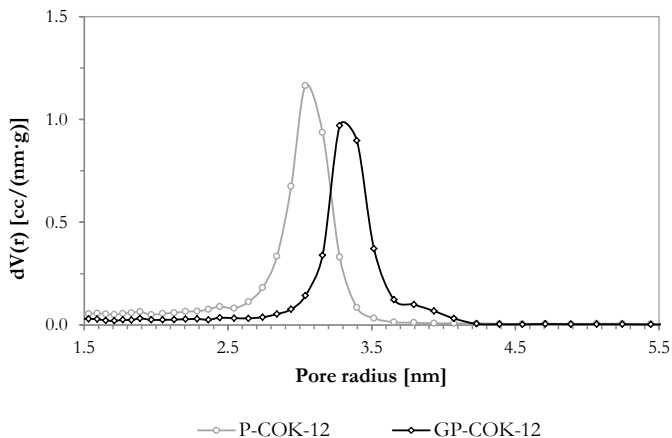


Figure 3.23 Pore size distribution of as-pressed GP-COK-12 as determined by the NLDFT method, revealing a pore radius of 3.3 nm. Data shown in the relevant pore size range.

The properties of the pressed material GP-COK-12 are summarized in Table 3.9 Pressing P-COK-12 to produce granulated GP-COK-12 yields a loss of long-range ordering. A decrease of pore volume and surface area due to the collapse of pores under the high pressure was observed for GP-COK-12.

Table 3.9 Properties of GP-COK-12. Pressing of P-COK-12 to produce GP-COK-12 results in a loss of mesoscale ordering, pore volume and surface area.

Material	P-COK-12	GP-COK-12
$d_{100}^a$ [nm]	8.39	8.70
$a^b$ [nm]	9.69	10.05
Type <sup>c</sup>	IV	IV
H <sup>d</sup>	H1	H1
$P_{DFT}^e$ [nm]	6.1	6.6
$V_{DFT}^f$ [cc/g]	0.640	0.536
$S_{BET}^g$ [m <sup>2</sup> /g]	647.7	579.2

<sup>a</sup> Interplanar distance between (100) planes estimated by SAXRD

<sup>b</sup> Lattice parameter estimated by SAXRD

<sup>c</sup> Type of isotherm

<sup>d</sup> Type of hysteresis

<sup>e</sup> Pore diameter estimated by NLDFT

<sup>f</sup> Pore volume estimated by NLDFT

<sup>g</sup> Specific surface area estimated by BET

### *Catalyst composition and structure*

SEM micrographs (Figure 3.24) revealed a macroporous morphology of fresh catalysts which is characteristic for this catalytic system<sup>120</sup>. An increase of the amount of large crystallites on the surface of Silica-CAT (Figure 3.24 d) can be observed. These crystallites have been identified as  $Mn_2O_3$ <sup>91</sup>.

### 3.4 COK-12 as a catalyst support for the oxidative coupling of methane

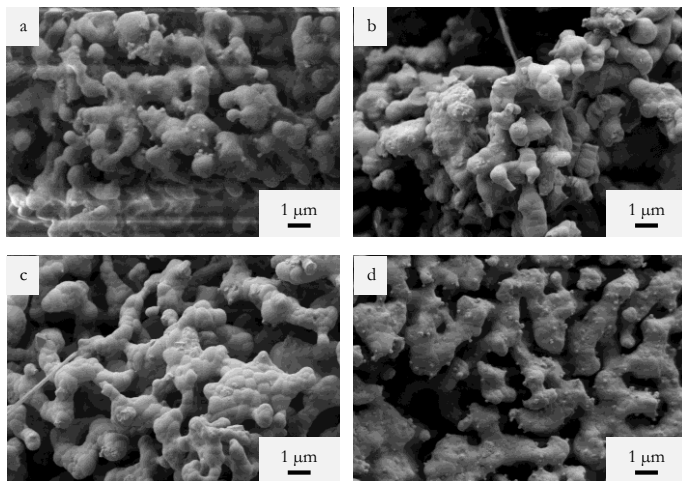


Figure 3.24 SEM micrographs of fresh catalysts: (a) P-CAT, (b) G-CAT, (c) GP-CAT, (d) Silica-CAT. There is an increase in the amount of large crystallites on the surface of Silica-CAT, which have been identified as the  $\text{Mn}_2\text{O}_3$  phase.

Elemental EDX mapping of the catalytic elements on each catalyst surface confirms a finer distribution on catalysts supported on P-COK-12 and M-COK-12 as opposed to that supported on commercial silica gel (Figure 3.25). This finer distribution was attributed to the ordered mesostructure of COK-12 supported catalysts prior to calcination. The distribution of catalytic components on GP-CAT and G-CAT is less fine, in all likelihood due to processing of the catalysts via pressing.

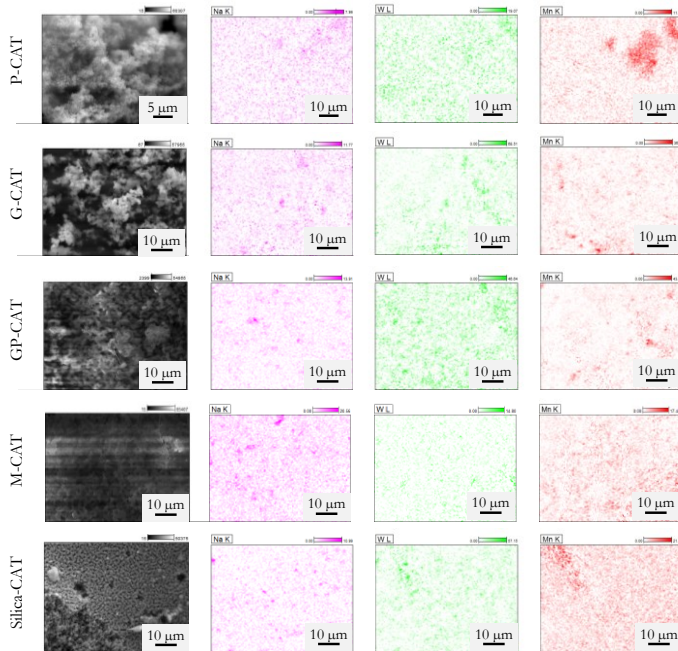


Figure 3.25 Elemental mapping on fresh catalyst surface by energy-dispersive X-ray spectroscopy (atomic percentage), Na (pink), W (green), Mn (red). Bar represents 10  $\mu\text{m}$ .

Elemental analysis of the catalysts carried out by ICP-OES corroborated the composition of the fresh catalysts (see Table 3.10). There is an excess of sodium present in M-CAT. As was discussed in section 3.3, this is attributed to a less efficient washing of M-COK-12, resulting in higher concentration of residual sodium from the silica source and the buffer solution.

### 3.4 COK-12 as a catalyst support for the oxidative coupling of methane

Table 3.10 Elemental composition of fresh catalysts determined by ICP-OES.

Catalyst	Na [at%]	W [at%]	Mn [at%]	Si [at%]
Theoretical	2.38	1.19	2.20	94.22
P-CAT	2.71	1.19	2.38	93.71
G-CAT	3.86	1.25	2.31	92.58
GP-CAT	3.43	1.10	2.18	93.28
M-CAT	8.47	1.18	2.47	87.87
Silica-CAT	2.94	1.24	2.55	93.27

XRD measurements reveal  $\alpha$ -cristobalite to be the main silica phase in all catalysts, with quartz as a secondary silica phase (Figure 3.26). It has been reported that for the  $\text{Na}_2\text{WO}_4\text{-Mn/SiO}_2$  catalyst, a phase transformation of the silica phase occurs, from amorphous silica (as-impregnated catalyst) to crystalline silica<sup>91</sup>. This phase transformation is due to the migration of sodium ions into the silica matrix, which in turn decrease the phase transformation temperature of silica to as low as 750°C. The calcination process for the catalyst preparation used in this work requires 800°C, ensuring that amorphous silica is crystallized. For all catalysts except M-CAT, sodium tungstate was identified as the main Na-W phase. In the case of M-CAT, sodium is present in the form of sodium manganese oxide, while tungstate appears as tungsten trioxide. Manganese also appears in the form of bixbyite (or braunite, similar diffraction pattern to  $\text{Mn}_2\text{O}_3$ ) for all catalysts.

Along with this phase transformation, the porous mesostructure of COK-12 and commercial silica supports collapsed, resulting in a loss of mesoporosity, as confirmed by nitrogen sorption analysis (Figure 3.27). The fresh catalysts have a surface area between 2 and 3  $\text{m}^2/\text{g}$  (Table 3.11).

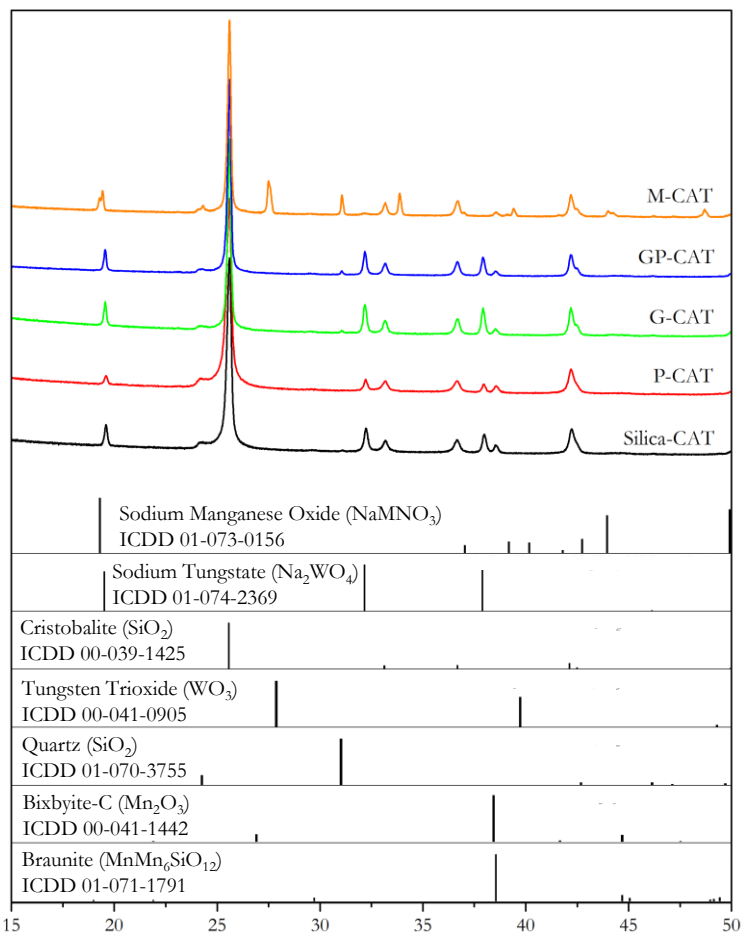


Figure 3.26 XRD patterns of fresh catalysts. The main phase in all catalysts is cristobalite, which appears as a result of phase transformation from amorphous silica due to the presence of sodium ions which decrease the phase transformation temperature. For all catalysts except M-CAT, sodium tungstate was identified as the main Na-W phase. In the case of M-CAT, sodium is present in the form of sodium manganese oxide, while tungstate appears as tungsten trioxide. Manganese also appears in the form of bixbyite (or braunite) for all catalysts. Patterns have been normalized to the cristobalite peak for comparison.

### 3.4 COK-12 as a catalyst support for the oxidative coupling of methane

The phase transformation from amorphous to crystalline silica has been reported as critical to obtain catalysts with a high selectivity towards  $C_2$  products (ethylene and ethane) in the oxidative coupling of methane<sup>86</sup>. It was proposed that, as opposed to using  $\alpha$ -cristobalite as a support, the use of amorphous silica and therefore the generation of cristobalite in situ is related to an improved dispersion, or even chemical bonding, of the sodium on the cristobalite surface.

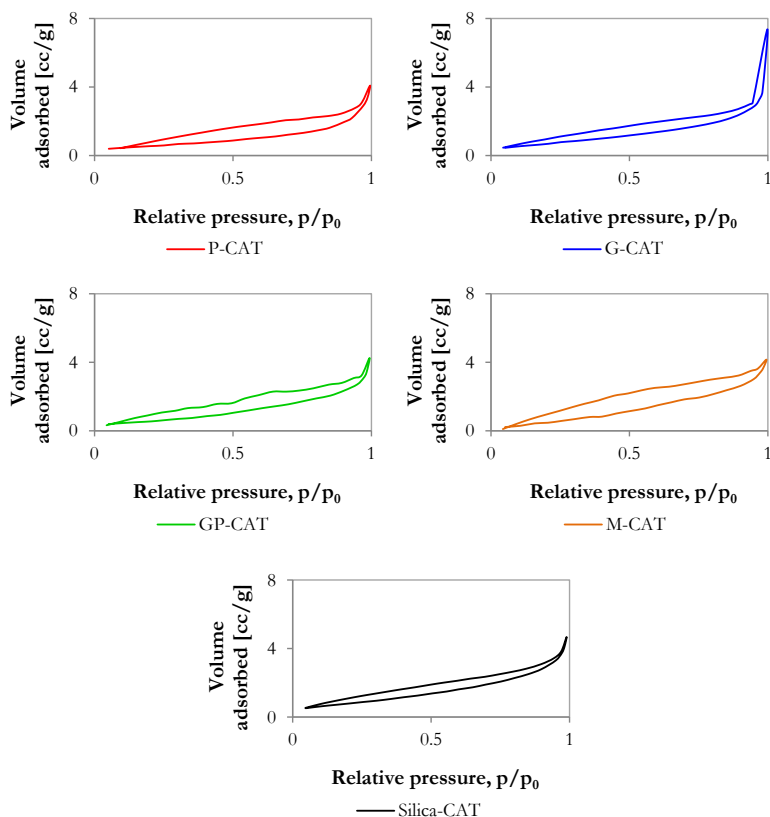


Figure 3.27 Nitrogen adsorption-desorption isotherms of fresh catalysts. A loss of surface area due to the collapse of the mesostructure of the support is observed.

The density of all catalysts was determined by gas pycnometry measurements (Table 3.11). It is noteworthy to mention the lower density of P-CAT of 1.93 g/ml with respect to other catalysts (2.30-2.72 g/ml), which exhibit a higher density due to processing.

Table 3.11 Specific surface area and density of fresh catalysts.

Catalyst	$S_{\text{BET}}$ [m <sup>2</sup> /g]	$\rho$ [g/cm <sup>3</sup> ]
P-CAT	2.0	1.93
G-CAT	2.7	2.47
GP-CAT	2.1	2.30
M-CAT	2.4	2.72
Silica-CAT	2.8	2.55

Five catalysts were prepared for this study, four supported on variations of COK-12 and one supported on commercial silica gel (Table 3.4). For all catalysts, a phase transformation from amorphous silica to cristobalite was observed upon calcination at 800°C, which occurs due to the presence of sodium ions that decrease the phase transformation temperature to as low as 750°C. The surface area of the catalysts decreases with respect to the surface area of the mesoporous silica support as a result of this phase transformation from around 600 m<sup>2</sup>/g to 2 m<sup>2</sup>/g. Catalysts exhibit different densities, with P-CAT having the lowest density (1.93g/cm<sup>3</sup>). This is expected given that no post-processing was carried out for P-CAT preparation and it is the only catalyst used for testing in powder form, as opposed to the granular catalysts (G-CAT, GP-CAT, M-CAT, Silica-CAT).

### 3.4.1.2 Catalyst structure after OCM

After testing in OCM, the macroporosity of the catalysts in comparison to the fresh catalysts is similar (fresh catalysts: Figure 3.24, used catalysts: Figure 3.28). Elemental mapping suggests that during OCM, melting of the catalytic components may occur,

### 3.4 COK-12 as a catalyst support for the oxidative coupling of methane

resulting in subsequent agglomeration that can yield areas with a greater concentration of active components in comparison to fresh catalysts (Figure 3.29).

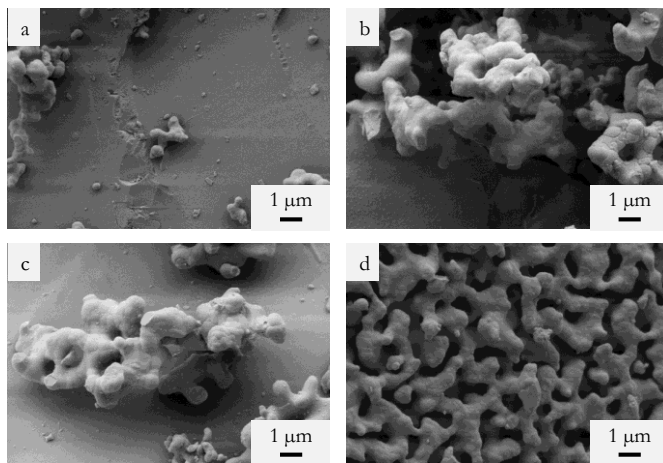


Figure 3.28 SEM micrographs of used catalysts after 15 hours and up to 775°C on stream: (a) P-CAT, (b) G-CAT, (c) GP-CAT, (d) Silica-CAT. Catalyst particles are mixed with quartz sand as a diluting agent (background in a, b and c).

The formation of a melt explains the loss of crystallites on the surface of used catalysts in comparison to fresh catalysts. This formation of a melt for Na/W/Mn/SiO<sub>2</sub> composites under OCM conditions has been studied by Nipan<sup>121</sup>. Koirala et. al.<sup>93</sup> also suggest the formation of a melt with increasing temperature during OCM, given that the melting temperature of Na<sub>2</sub>WO<sub>4</sub> is about 700°C. This is expected to produce a change in the surface concentration of active components, due to their potential coverage by a homogeneous layer of melt.

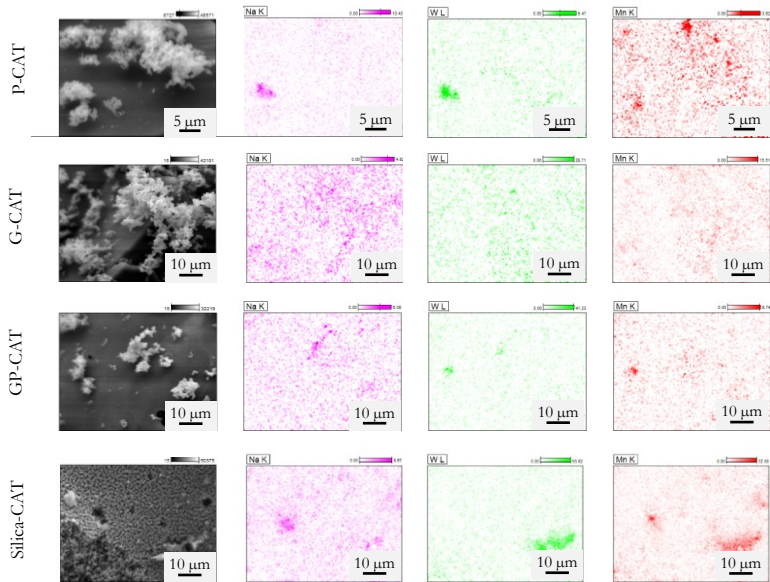


Figure 3.29 Elemental mapping on used catalyst surface after 15 hours and up to 775°C on stream by energy-dispersive X-ray spectroscopy (atomic percentage), Na (pink), W (green), Mn (red). Agglomeration of catalytic elements on the catalyst surface as a consequence of melting during OCM occurs. For P-CAT: bar corresponds to 5  $\mu\text{m}$ . For G-CAT, GP-CAT and Silica-CAT: bar corresponds to 10  $\mu\text{m}$ .

XRD patterns of used P-CAT reveal that silica is present as cristobalite and quartz, while a secondary quartz phase corresponding to the crystalline dilutant is also observed (Figure 3.30). Tungsten is present as manganese tungsten oxide, confirming the appearance of a new phase. A sodium phase could not be identified in the XRD pattern of used catalyst. Literature data indicates that sodium can interact strongly with  $\text{SiO}_2$ <sup>122</sup>. With this in mind, the apparent loss of sodium in the spent catalyst can be attributed to three factors: (i) sodium migrates to the quartz reactor walls, (ii) sodium migrates to the quartz dilutant and (iii) sodium diffuses into the silica matrix of the catalyst, as suggested by Elkins, et. al<sup>96</sup>. The re-formation of  $\text{Na}_2\text{WO}_4$  following re-oxidation of the

### 3.4 COK-12 as a catalyst support for the oxidative coupling of methane

used catalyst was reported by Sadjadi, et. al.<sup>120</sup>, indicating that sodium is not lost during OCM but could be present as Na<sub>2</sub>O in the bulk of the catalyst.

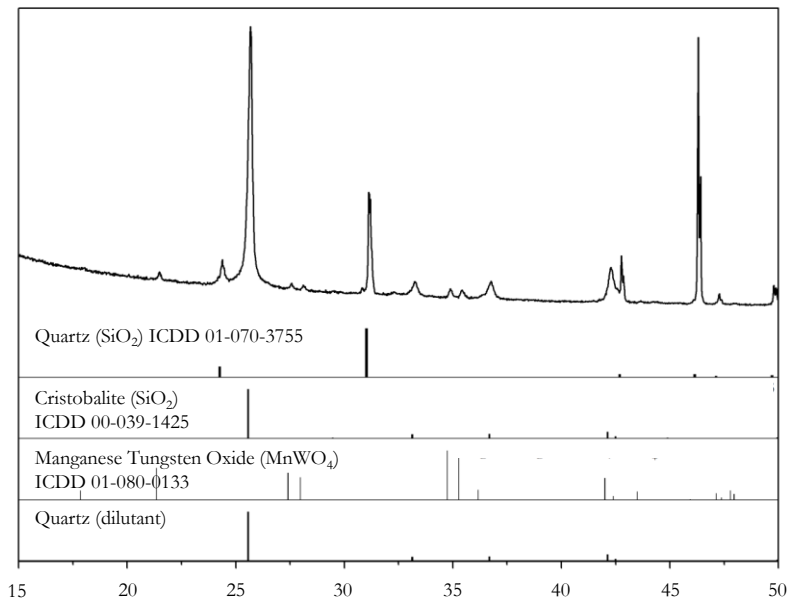


Figure 3.30 XRD patterns of used P-CAT after 15 hours and up to 775°C on stream. Manganese tungsten oxide appears as a new phase and a sodium phase cannot be identified, probably due to diffusion of sodium ions to the different silica matrices (dilutant, reactor and bulk catalyst). An intense quartz peak corresponding to the dilutant with a preferred orientation can be observed.

The information obtained by characterization of used P-CAT suggests the formation of a new phase (manganese tungsten oxide) after OCM. This can explain the loss of crystallites on the catalyst surface, as well as the possible formation of a melt during OCM that covers the surface of the catalyst. No sodium phase could be identified by XRD, possibly due to the migration of sodium into either the quartz reactor walls, the quartz dilutant or the

bulk silica of the catalyst, given the strong interaction that is expected between sodium and SiO<sub>2</sub>.

### 3.4.2 Catalyst performance in the oxidative coupling of methane

The catalysts were tested in terms of their activity under normal OCM conditions, at lower reaction temperature and to study their stability at prolonged times on stream. Three experiments were conducted, as summarized in Table 3.12.

Table 3.12 Description of catalytic testing experiments and catalysts used for each experiment.

Experiment	Brief description	Catalysts used
Catalytic performance tests at standard OCM conditions	Between 725-775°C	P-CAT, GP-CAT, G-CAT, Silica-CAT
Catalytic performance tests at lower reaction temperature	Between 500-725°C	P-CAT, GP-CAT, M-CAT, Silica-CAT
Catalyst stability study	750°C, 200 h on stream	P-CAT, GP-CAT, Silica-CAT

#### 3.4.2.1 Catalytic performance at standard OCM conditions

As can be seen in Figure 3.31, P-CAT has a maximum conversion of methane of 24 % with a maximum C<sub>2</sub> selectivity of 60.5 % at the highest temperature (775°C, Table 3.13). Between 5 and 10 h on stream, which corresponds to a reaction temperature of 750°C, P-CAT exhibits a methane conversion of 15.5 %, which is slightly higher than that reported for the analogous catalyst supported on SBA-15 at the same temperature (14 %)<sup>97</sup>.

### 3.4 COK-12 as a catalyst support for the oxidative coupling of methane

Likewise, Yildiz, et. al. reported a total selectivity to  $C_2$  at  $750^\circ C$  of 65 % using the SBA-15 supported catalyst<sup>97</sup>. The most interesting aspect of this finding was not only the high selectivity, but the fact that both the selectivity and the methane conversion were higher than that of the catalyst supported on commercial silica gel (equivalent to Silica-CAT), which had a total selectivity to  $C_2$  of 50 %. In the present study (Figure 3.31) it was found that at  $750^\circ C$ , the total selectivity to  $C_2$  of P-CAT reaches 54 %, which is lower than the selectivity of Silica-CAT (63 %). This finding corresponds to the “upper bound” limit predicted for OCM, in which an increase in methane conversion is accompanied by a decrease in selectivity.

A decrease of conversion is observed for G-CAT in comparison to P-CAT, which correlates with an increase in the density of the catalyst, i.e., the higher the catalyst density, the lower the methane conversion at the same reaction conditions. Furthermore, P-CAT exhibits a higher selectivity to ethylene than ethane in comparison with the granular catalysts (G-CAT, GP-CAT, Silica-CAT), which can be attributed to extended gas phase reactions that occur within the catalyst bed. For catalysts with a lower density, the catalyst bed height increases for the same catalyst mass, resulting in a longer residence time of reagents and products in contact with the catalyst, promoting further reactions.

An increase in conversion of  $CH_4$  was obtained for G-CAT and GP-CAT in comparison to Silica-CAT, due to the finer dispersion of catalytic components on the surface for catalysts prepared on an ordered mesoporous support.

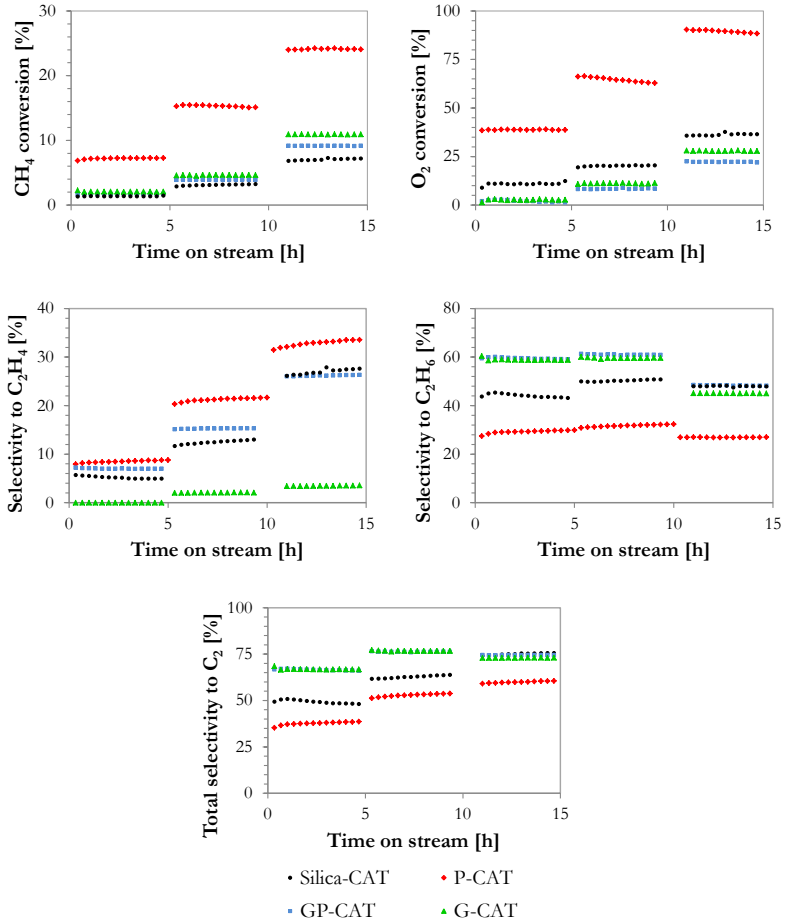


Figure 3.31 Conversion and selectivity to C<sub>2</sub> products of Silica-CAT, P-CAT, GP-CAT and G-CAT. An increase of 25°C is carried out each 5h. CH<sub>4</sub>:N<sub>2</sub>:O<sub>2</sub> ratio was 4:4:1 with a flow rate of 60 ml/min.

### 3.4 COK-12 as a catalyst support for the oxidative coupling of methane

Table 3.13 Catalytic activity tests: maximum methane conversion and selectivity to C<sub>2</sub> products at 775°C after 15 h.

Catalyst	CH <sub>4</sub> conversion [%]	Total C <sub>2</sub> selectivity [%]	C <sub>2</sub> H <sub>4</sub> selectivity [%]	C <sub>2</sub> H <sub>6</sub> selectivity [%]
P-CAT	24.0	60.5	33.5	27.0
G-CAT	9.2	73.0	28.0	45.0
GP-CAT	10.9	74.1	26.2	47.9
Silica-CAT	7.2	75.5	27.6	47.9

#### 3.4.2.2 Catalytic performance at lower reaction temperature

In Figure 3.32, the conversion of methane and selectivity to C<sub>2</sub> products for OCM carried out at lower reaction temperatures without dilution is presented. It is clear that for the case of M-CAT, activation of the catalyst occurred at a lower temperature (~550°C) than the rest of the catalysts. However, after 680°C there is a decrease in conversion with temperature increase for M-CAT. At this temperature, the conversion of methane of M-CAT reaches 7 % with a selectivity of 76 %, which is similar to that reported for Na<sub>2</sub>WO<sub>4</sub>-Mn/SiO<sub>2</sub> catalysts albeit at higher reaction temperatures. Overall materials supported on COK-12 have a lower activation temperature in comparison to Silica-CAT.

A decrease in the activation and reaction temperature of OCM catalysts, such as that observed for M-CAT, could prove a great economic advantage for the potential application of these catalysts in an industrial OCM process.

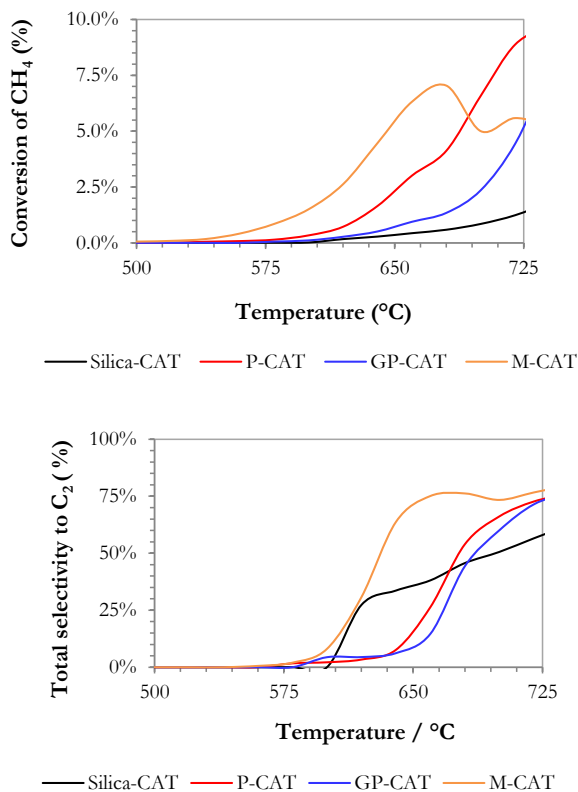


Figure 3.32 Conversion of methane and total selectivity to C<sub>2</sub> products at lower reaction temperature. CH<sub>4</sub>:N<sub>2</sub>:O<sub>2</sub> ratio was fixed at 85:10:5 with a flow rate of 60 ml/min without dilution of the catalyst bed. Conversion of methane occurs at temperatures as low as 550°C for M-CAT.

### 3.4.2.3 Catalyst stability after prolonged time on stream

Figure 3.33 illustrates the behavior of selected catalysts for longer reaction times in OCM. Although high conversions are initially reached, especially for GP-CAT, there appears to be a sudden deactivation of the COK-12 supported catalysts in comparison to

### 3.4 COK-12 as a catalyst support for the oxidative coupling of methane

Silica-CAT, indicating that the long-term stability should be improved. This drop in activity is most notable for GP-CAT, reaching initial methane conversions of up to 26 % which decrease to less than 10 % after 100 hours on stream.

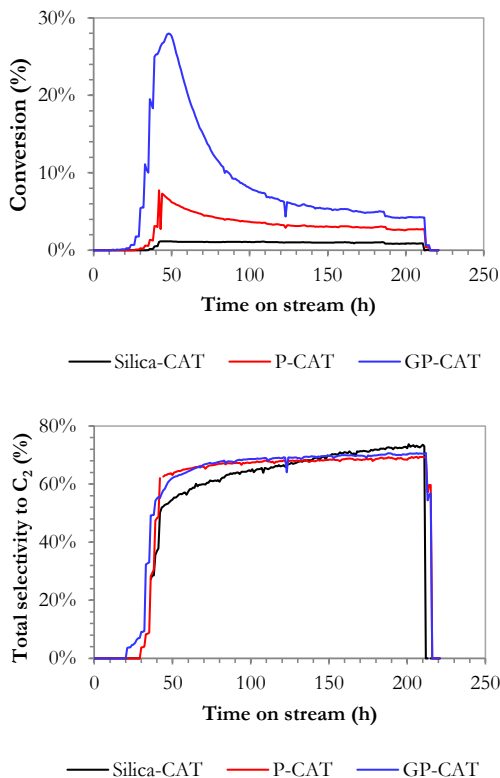


Figure 3.33 Conversion of methane and total selectivity to C<sub>2</sub> products at prolonged time on stream. Reaction carried out at 750°C with a CH<sub>4</sub>:N<sub>2</sub>:O<sub>2</sub> ratio of 4:4:1 and 60 ml/min flow rate without dilution of the catalyst bed. Deactivation of the catalysts after prolonged time on stream is observed.

Catalyst deactivation can be attributed to the formation of hotspots within the catalyst bed, which is common when no dilutant is used to dissipate heat. The formation of hotspots leads to

runaway temperatures within the catalyst bed, which deactivate the catalyst and produce particle agglomeration.

In spite of the loss of activity after prolonged times on stream, the activity of P-CAT and GP-CAT is higher than that of Silica-CAT, with similar selectivity to C<sub>2</sub> products for all three catalysts, indicating a superior performance.

### 3.5 Conclusions and outlook

The ordered mesoporous silica material COK-12 was successfully upscaled with no significant change in the properties of the material, achieving a production of up to 65 g of material. The material is synthesized at room temperature and precipitation of the solid occurs immediately under the synthesis conditions. With this in mind, the success of upscaling was attributed to the absence of temperature and mixing control necessary for COK-12 synthesis, which would otherwise complicate the upscaling of any process.

Monolithic COK-12 (M-COK-12) was successfully synthesized by acidification of the original COK-12 synthesis, yielding irregular hard particles ranging from a few micrometers to several centimeters in size, which are agglomerates of sub particles of up to 2.5 μm in length and 500 nm in diameter. Upon comparison of the results obtained for M-COK-12 materials, the only significant change in the porosity of the material is a loss of microporosity, resulting in a decrease of the total pore volume and specific surface area in comparison to P-COK-12. The direct synthesis of a monolithic OMS with significantly less microporosity in comparison to P123-templated counterparts could be of great relevance for studies in catalysis. Furthermore, M-COK-12 synthesis was also successfully upscaled, yielding up to 60 g of material.

COK-12 was used in various forms as a support for the Na<sub>2</sub>WO<sub>4</sub>-Mn catalyst, for testing in the oxidative coupling of methane (OCM). All fresh catalysts exhibited a loss of mesoporosity and surface area due to the phase transformation of amorphous to crystalline silica in the form of cristobalite. This phase

### *3.5 Conclusions and outlook*

transformation has been reported as critical to obtain high selectivity to C<sub>2</sub> products in OCM.

Na<sub>2</sub>WO<sub>4</sub>-Mn/SiO<sub>2</sub> catalysts supported on COK-12 were tested to determine their activity, resulting in excellent conversion and selectivity to C<sub>2</sub> products when the catalyst was used in powder form, up to 24 % methane conversion with 61 % C<sub>2</sub> selectivity at 775°C. The catalyst supported on monolithic COK-12 can be activated at temperatures below 575°C, which is desirable for industrial application. A loss of activity was observed for COK-12 supported catalysts after several hours of use, with deactivation of the catalysts within the first 50 hours on stream. This deactivation was attributed to runaway temperatures within the catalyst bed due to the formation of hotspots. Nonetheless, COK-12 supported catalysts exhibit a superior performance to the standard Silica-CAT even after deactivation.

The characterization of the catalyst supported on powder OCM after reaction reveals a new crystalline phase as well as the absence of a sodium phase, which is likely due to the diffusion of sodium ions into the various silica matrices available (quartz reactor walls, quartz dilutant, bulk silica of the catalyst).

The excellent performance of the Na<sub>2</sub>WO<sub>4</sub>-Mn/SiO<sub>2</sub> catalyst supported on powder and monolithic COK-12 in terms of high yield and activation at lower temperatures, respectively, is of great significance in ongoing OCM research. The relatively inexpensive synthesis of powder and monolithic COK-12 support, in comparison to its analog OMS material SBA-15, represents an important development in OCM catalyst research. Moreover, the facile upscaling of powder and monolithic COK-12 make this material an attractive candidate for use as a catalyst support in pilot plant research. Further investigations regarding post-processing of these materials for possible industrial application (pelletizing, granulation, etc.), coupled with reactor engineering and processing, will contribute to the development of OCM technology, paving the way for industrial application.

## 4 Tailoring the mesostructure of COK-12

An attractive characteristic of the synthesis of ordered mesoporous silica (OMS) materials prepared by soft templating is the ability to tailor the mesostructure with the use of micellar swelling agents. Depending on the templating agent selected, micellar swelling agents that solubilize within the micelle cores can be used to expand the size of the micelles and produce micellar phase transitions. This versatility expands the potential application of OMS materials, e.g. for use in adsorption/separation of bulky molecules<sup>123,124</sup> or immobilization of enzymes<sup>125</sup>.

The motivation behind the studies presented in this chapter was to test the flexibility of the COK-12 synthesis in terms of pore enlargement by the incorporation of micellar swelling agents. Two swelling agents were chosen: hexane, which has been reported as an effective swelling agent<sup>37,43</sup>, and polypropylene glycol (PPG), which was demonstrated to enlarge the pores of SBA-15<sup>126</sup>.

Interestingly, an increase in the pore size was not the only phenomenon observed, but also a mesophase change in COK-12. The use of hexane resulted in the formation of a mesocellular foam (MCF) and the use of PPG produced a mesophase change from hexagonal to multilamellar vesicular (MLV). The studies regarding the use of hexane to produce MCF and PPG to produce MLV are presented in this chapter. Both studies are based on the synthesis of COK-12; powder COK-12 is presented as the reference material and is used as a basis for comparison. The work presented in this chapter can be found in 'Tailoring of ordered mesoporous silica

## 4.1 Materials synthesis

COK-12: Room temperature synthesis of mesocellular foam and multilamellar vesicles', *Micro. Meso. Mater.*, 2018, **267**, 142-149.

### 4.1 Materials synthesis

The synthesis of silica MCF and MLV materials is based on the synthesis of COK-12 (section 3.1.1), with swelling agent incorporation. The templating agent (P123) is dissolved in water at room temperature. After P123 dissolution and before incorporation of the buffer, a certain amount of n-hexane (Roth) or polypropylene glycol (PPG, average molecular weight  $\sim 2000$  mol/g, Sigma-Aldrich) was added (Table 4.1 and Table 4.2) after which the buffer is added. The sodium silicate solution is then added and immediate precipitation is observed. After aging for 24 hours the materials were washed with water, filtered, dried and calcined at  $500^{\circ}\text{C}$  to remove organics.

Table 4.1 Conditions for MCF synthesis with hexane as a swelling agent.

Material	P-COK-12	MCF-COK-12-1.0	MCF-COK-12-2.0
Hexane [ml]	0	1.0	2.0
P123 [g]	4	4	4
DIW <sup>a</sup> [ml]	107.5	107.5	107.5
Citric acid [g]	3.68	3.68	3.68
Sodium citrate [g]	2.54	2.54	2.54
Sodium silicate [g]	10.4	10.4	10.4
DIW <sup>b</sup> [ml]	30.0	30.0	30.0
DIW <sup>c</sup> [ml]	500.0	500.0	500.0

<sup>a</sup> For P123 solution

<sup>b</sup> For sodium metasilicate solution

<sup>c</sup> For washing

#### 4 Tailoring the mesostructure of COK-12

Table 4.1 (cont.) Conditions for MCF synthesis with hexane as a swelling agent.

Material	MCF-COK-12-4.0	MCF-COK-12-5.4	MCF-COK-12-8.0
Hexane [ml]	4.0	5.4	8.0
P123 [g]	4	4	4
DIW <sup>a</sup> [ml]	107.5	107.5	107.5
Citric acid [g]	3.68	3.68	3.68
Sodium citrate [g]	2.54	2.54	2.54
Sodium silicate [g]	10.4	10.4	10.4
DIW <sup>b</sup> [ml]	30.0	30.0	30.0
DIW <sup>c</sup> [ml]	500.0	500.0	500.0

Table 4.1 (cont.) Conditions for MCF synthesis with hexane as a swelling agent.

Material	MCF-COK-12-16.0	MCF-COK-12-24.0	MCF-COK-12-32.0
Hexane [ml]	16.0	24.0	32.0
P123 [g]	4	4	4
DIW <sup>a</sup> [ml]	107.5	107.5	107.5
Citric acid [g]	3.68	3.68	3.68
Sodium citrate [g]	2.54	2.54	2.54
Sodium silicate [g]	10.4	10.4	10.4
DIW <sup>b</sup> [ml]	30.0	30.0	30.0
DIW <sup>c</sup> [ml]	500.0	500.0	500.0

Table 4.2 Conditions for MLV synthesis with polypropylene glycol (PPG) as a swelling agent.

Material	P-COK-12	MLV-COK-12-0.10	MLV-COK-12-0.25
PPG [ml]	0	0.1	0.25
P123 [g]	4	4	4
DIW <sup>a</sup> [ml]	107.5	107.5	107.5
Citric acid [g]	3.68	3.68	3.68
Sodium citrate [g]	2.54	2.54	2.54
Sodium silicate [g]	10.4	10.4	10.4
DIW <sup>b</sup> [ml]	30.0	30.0	30.0
DIW <sup>c</sup> [ml]	500.0	500.0	500.0

<sup>a-c</sup> See above

## 4.2 Hexane as a swelling agent

Table 4.2 (cont.) Conditions for MLV synthesis with polypropylene glycol (PPG) as a swelling agent.

Material	MLV- COK-12-0.50	MLV- COK-12-0.75	MLV- COK-12-1.00
PPG [ml]	0.50	0.75	1.00
P123 [g]	4	4	4
DIW <sup>a</sup> [ml]	107.5	107.5	107.5
Citric acid [g]	3.68	3.68	3.68
Sodium citrate [g]	2.54	2.54	2.54
Sodium silicate [g]	10.4	10.4	10.4
DIW <sup>b</sup> [ml]	30.0	30.0	30.0
DIW <sup>c</sup> [ml]	500.0	500.0	500.0

Table 4.2 (cont.) Conditions for MLV synthesis with polypropylene glycol (PPG) as a swelling agent.

Material	MLV- COK-12-1.50	MLV- COK-12-2.00	MLV- COK-12-2.50
PPG [ml]	1.50	2.00	2.50
P123 [g]	4	4	4
DIW <sup>a</sup> [ml]	107.5	107.5	107.5
Citric acid [g]	3.68	3.68	3.68
Sodium citrate [g]	2.54	2.54	2.54
Sodium silicate [g]	10.4	10.4	10.4
DIW <sup>b</sup> [ml]	30.0	30.0	30.0
DIW <sup>c</sup> [ml]	500.0	500.0	500.0

## 4.2 Hexane as a swelling agent: synthesis of a silica mesocellular foam

Mesocellular foams (MCF) are composed of uniformly sized spherical cells that are connected by windows, creating an interconnected 3-D pore system (Figure 1.6). MCF can be synthesized by the incorporation of micellar swelling agents to surfactant-templated syntheses<sup>48</sup>. This transition is the result of the formation of a noded structure in cylindrical micelles which

maintained their hexagonal packing. Upon increasing swelling agent addition, the nodes separate into spherical micelles and aggregate to form MCF (Figure 1.7).

In this section, studies regarding the preparation of silica MCFs based on the synthesis of COK-12 using sodium silicate as the silica source, P123 as a structure directing agent and hexane as a micellar swelling agent are presented. The phase transition from hexagonal to MCF is discussed.

The morphology of selected MCF samples is revealed by SEM (Figure 4.1). After transition from hexagonal to MCF morphology (Figure 4.1 a vs. Figure 4.1 b, see Figure 4.4 for nitrogen adsorption isotherms), there appears to be little change in the morphology of the material, except for a loss of sharp edges characteristic of P-COK-12.

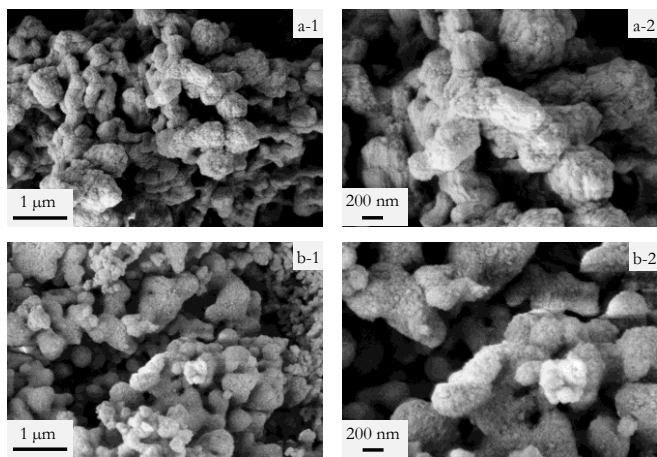


Figure 4.1 SEM micrographs of selected as-calcined MCF-COK-12. (a) MCF-COK-12-2.0 ( $p6m$  mesostructure). (b) MCF-COK-12-4.0 (MCF morphology). Little difference is observed between (a) and (b), despite the difference in mesostructure.

SAXRD patterns of MCF samples are shown in Figure 4.2. The (100) peak shows a clear tendency to shift to lower  $2\theta$  values with increasing amounts of hexane. This shift corresponds to an increase in the interplanar distance  $d_{100}$  (Table 4.3). Moreover, it is

## 4.2 Hexane as a swelling agent

evident that long-range ordering decreased, visible in the decrease of the intensity second and third reflections corresponding to (110) and (200) with increasing amount of hexane.

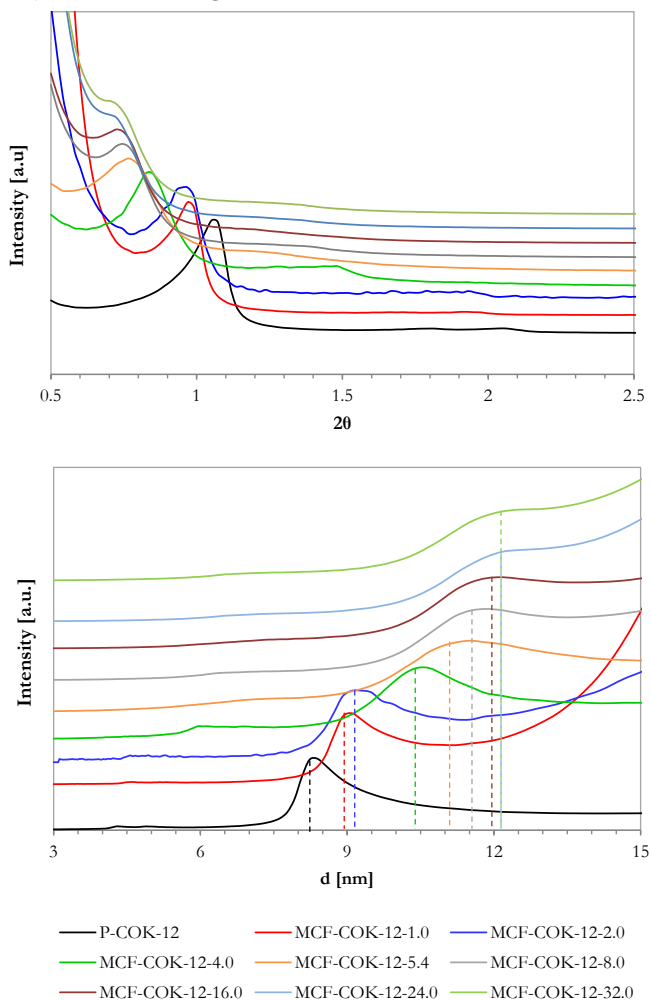


Figure 4.2 Top: SAXRD pattern of as-calcined MCF-COK-12. Patterns have been normalized to the (100) peak and shifted for comparison. With increasing hexane concentration, a shift of the (100) peak to lower  $2\theta$  values is observed. Bottom: d-spacing (shown for the (100) family of planes). See Table 4.3 for more information.

Upon comparison of TEM micrographs of the standard P-COK-12 and micrographs of MCF-COK-12, an increase in the diameter of the pores at the highest hexane concentration is evident (Figure 4.3). For the sample with 2.0 ml hexane/g P123 (MCF-COK-12-2.0, Figure 4.3 b) the pores are apparently the same size as the pores of P-COK-12, however a loss of mesoscale ordering was observed. A significant increase in pore size occurred for the sample with 5.4 ml hexane/g P123 (MCF-COK-12-5.4, Figure 4.3 c), with a pore diameter of 7.7 nm (estimated graphically).

Figure 4.4 illustrates the progression from type H1 to type H2 hysteresis with increasing concentration of hexane. For hexane of 4.0 ml/g P123 and higher, the type of hysteresis is H2, which is characteristic of “ink-bottle” shaped pores. This change in the type of hysteresis corresponds to a phase transition in the mesostructure due to the preferential solubilization of hexane into the cores of P123 micelles. The phase transition is accompanied by an increase in pore size, from 6.6 nm to 8.4 nm, which was the highest pore size obtained (Table 4.3).

The distribution of the size of cylindrical pores (in the case of MCF-COK-12-1.0 and MCF-COK-12-2.0) and of pore cells and windows (for materials with “ink-bottle” pores, MCF-COK-12-4.0 and higher) are shown in Figure 4.5 and Figure 4.6. There is a slight increase in pore size for materials with cylindrical pores, and a sudden increase for materials with “ink-bottle” pores. An increase in hexane concentration results in a more uniform window size.

## 4.2 Hexane as a swelling agent

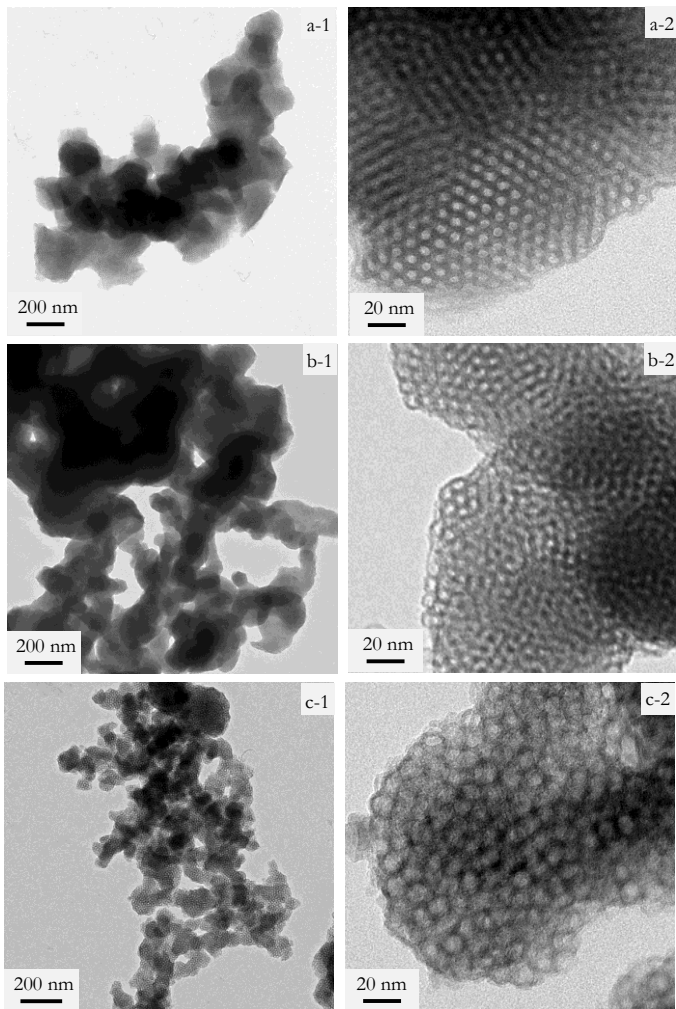


Figure 4.3 TEM micrographs of as-calcined MCF-COK-12. (a) Standard P-COK-12, (b) MCF-COK-12-2.0 and (c) MCF-COK-12-5.4. An increase in the pore size accompanied by a decrease in ordering is observed.

#### 4 Tailoring the mesostructure of COK-12

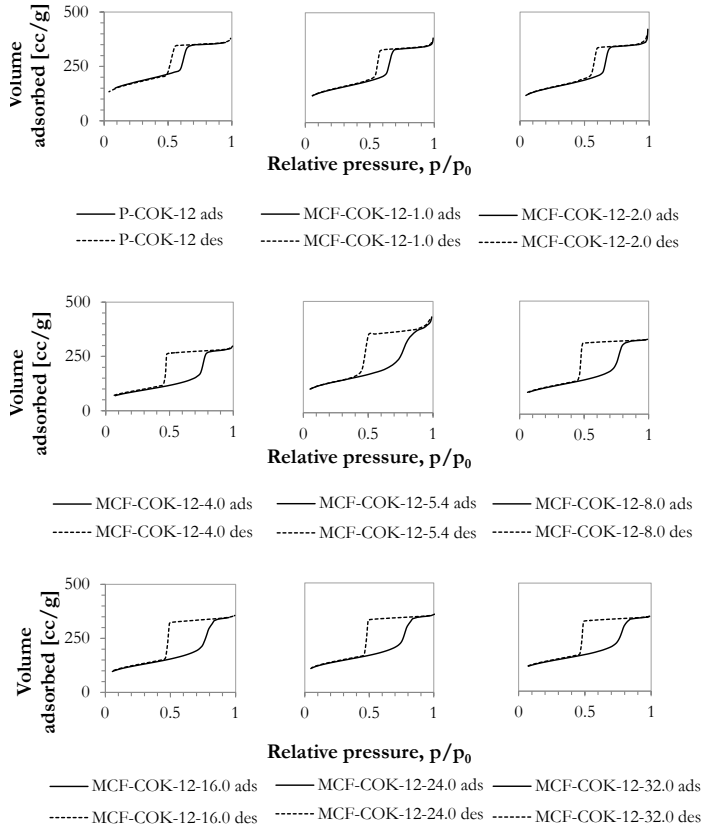


Figure 4.4 Nitrogen adsorption-desorption isotherms of as-calcined MCF-COK-12. The isotherms are type IV with H1 hysteresis until a shift to H2 hysteresis is observed for MCF-COK-12-4.0. Type H2 hysteresis is associated to materials with “ink-bottle” pores.

## 4.2 Hexane as a swelling agent

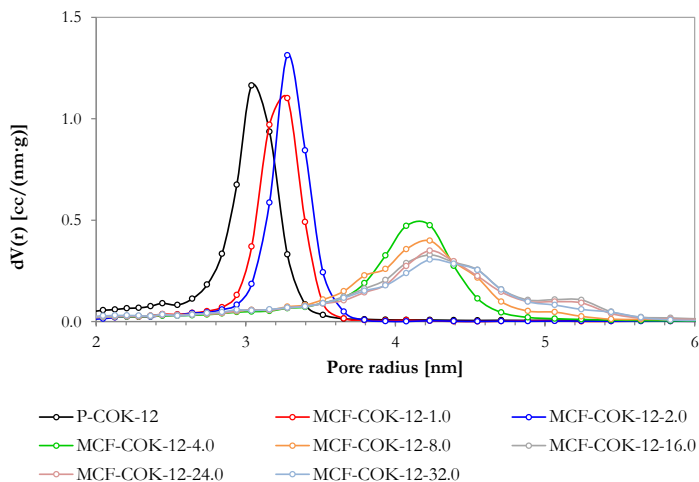


Figure 4.5 Pore (samples with H1 hysteresis) and Cell size distribution (samples with H2 hysteresis) of as-calcined MCF-COK-12 as determined by the NLDFT method.

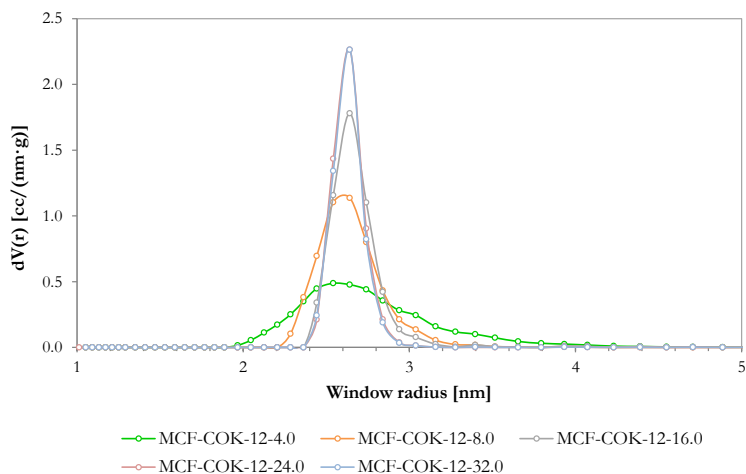


Figure 4.6 Window size distribution of as-calcined MCF-COK-12 (samples with H2 hysteresis) as determined by the NLDFT method. Data is shown for the relevant size range.

#### 4 Tailoring the mesostructure of COK-12

Table 4.3 Properties of as-calcined MCF-COK-12 synthesized using hexane as a micellar swelling agent.

Material	P-COK-12	MCF-COK-12-1.0	MCF-COK-12-2.0
Type <sup>a</sup>	IV	IV	IV
H <sup>b</sup>	H1	H1	H1
d <sub>100</sub> <sup>c</sup> [nm]	8.39	9.06	9.24
a <sup>d</sup> [nm]	9.69	10.46	10.67
P <sub>DFT</sub> <sup>e</sup> [nm]	6.1	6.5	6.6
I <sub>DFT</sub> <sup>f</sup> [nm]	-	-	-
V <sub>DFT</sub> <sup>g</sup> [cc/g]	0.640	0.543	0.566
S <sub>BET</sub> <sup>h</sup> [m <sup>2</sup> /g]	647.7	496.3	490.2

<sup>a</sup> Type of isotherm

<sup>b</sup> Type of hysteresis

<sup>c</sup> Interplanar distance between (100) planes estimated by SAXRD

<sup>d</sup> Lattice parameter estimated by SAXRD

<sup>e</sup> Cell diameter estimated by NLDFT

<sup>f</sup> Window diameter estimated by NLDFT

<sup>g</sup> Pore volume estimated with the adsorption branch by NLDFT

<sup>h</sup> Specific surface area estimated by BET

Table 4.3 (cont.) Properties of as-calcined MCF-COK-12 synthesized using hexane as a micellar swelling agent.

Material	MCF-COK-12-4.0	MCF-COK-12-5.4	MCF-COK-12-8.0
Type <sup>a</sup>	IV	IV	IV
H <sup>b</sup>	H2	H2	H2
d <sub>100</sub> <sup>c</sup> [nm]	10.56	11.53	11.82
a <sup>d</sup> [nm]	12.19	13.31	13.65
P <sub>DFT</sub> <sup>e</sup> [nm]	8.2	8.4	8.4*
I <sub>DFT</sub> <sup>f</sup> [nm]	5.2	5.3	5.3
V <sub>DFT</sub> <sup>g</sup> [cc/g]	0.436	0.625	0.495
S <sub>BET</sub> <sup>h</sup> [m <sup>2</sup> /g]	295.8	460.8	393.9

<sup>a-h</sup> See above.

\* The contribution of the shoulder observed graphically is not taken into account for this estimation

## 4.2 Hexane as a swelling agent

Table 4.3 (cont.) Properties of as-calcined MCF-COK-12 synthesized using hexane as a micellar swelling agent.

Material	MCF-COK-12-16.0	MCF-COK-12-24.0	MCF-COK-12-32.0
Type <sup>a</sup>	IV	IV	IV
H <sup>b</sup>	H2	H2	H2
d <sub>100</sub> <sup>c</sup> [nm]	12.12	12.53	12.53
a <sup>d</sup> [nm]	13.99	14.47	14.47
P <sub>DFT</sub> <sup>e</sup> [nm]	8.4*	8.4*	8.4*
I <sub>DFT</sub> <sup>f</sup> [nm]	5.3	5.3	5.3
V <sub>DFT</sub> <sup>g</sup> [cc/g]	0.531	0.528	0.518
S <sub>BET</sub> <sup>h</sup> [m <sup>2</sup> /g]	402.9	450.4	445.1

<sup>a-h</sup> See above.

\* The contribution of the shoulder observed graphically is not taken into account for this estimation

Table 4.3 shows the properties of mesocellular foam materials prepared by using hexane as a micellar swelling agent. The properties of P-COK-12 are shown for comparison.

An increase in the size of the pores with an increase of hexane concentration up to 2.0 ml / g P123 was observed, from 6.1 nm for standard P-COK-12 to 6.6 for MCF-COK-12-2.0. Further increase in hexane concentration resulted in a mesophase transition from cylindrical hexagonally ordered mesopores to mesocellular foam (MCF), as evidenced graphically by the hysteresis of nitrogen adsorption isotherms. This phase transition is associated to the formation of “ink-bottle” type pores, with a cell diameter of up to 8.5 nm and a window opening of up to 5.3 nm. After the mesophase transition occurs (for a hexane concentration of 4.0 ml /g P123, MCF-COK-12-4.0), the cell and window sizes do not change, but the size distribution of the windows becomes narrower.

Increasing the hexane concentration led to increasing values of the lattice parameter *a*. Given that the size of the cell and window does not increase, it can be deduced that the walls of MCF materials become thicker with increasing amounts of hexane. However, this increase in wall thickness is not apparent in TEM images (Figure 4.3). While SAXRD analysis confirms an increase in the spacing

between pores, the cell size distribution determined by NLDFT (Figure 4.5) shows a shoulder at larger cell sizes, up to 10.6 nm. The contribution of this shoulder to the total pore size distribution is 12 % for MCF-COK-12-8.0, 33 % for MCF-12-16.0 and 29 % for MCF-COK-12-24.0. A shoulder is not observed for MCF-COK-12-32.0, however the peak is quite broad. This broad pore size distribution and the contribution of a secondary larger cell size could be responsible for the increase in the lattice parameter, meaning that there is no thickening of the walls of MCF materials.

A similar study by Lettow, et. al.<sup>48</sup> examining the phase transition of SBA-15 with the incorporation of 1,3,5-trimethylbenzene (TMB), led to the proposal of a mechanism for the phase transition from a  $p6m$  hexagonal symmetry to MCF. In this study, the transition to MCF is also characterized by a sudden increase in pore diameter, although the SAXRD pattern at the phase change was that of a  $p6m$  hexagonal symmetry. It was proposed that the change in pore morphology is due to the formation of a noded structure in the cylindrical pores, while maintaining their hexagonal packing (see Figure 1.7 for reference). With increasing TMB concentration the nodes separate into spherical micelles that aggregate and form the MCF phase. The mesophase change is driven by the need to decrease the micelle surface-to-volume ratio with the incorporation of more swelling agent into the synthesis. The transition from cylindrical micelles to the spherical micelles that make up the MCF mesophase is driven by the need to cover an increasing amount of swelling agent with a fixed amount of P123. Cores of swelling agent are formed and are covered with the minimum amount of P123, resulting in spherical micelles and the noded structure depicted in Figure 1.7.

The facile synthesis of silica MCF at room temperature and using an inexpensive silica source has been demonstrated in this work. In contrast to the most recent reports regarding silica MCF synthesis, the synthesis based on COK-12 is more economically viable and could be potentially upscaled as was demonstrated in the previous chapter. Potential applications in adsorption/separation of

### 4.3 Polypropylene glycol as a swelling agent

biomolecules make this synthesis of MCF an important contribution to the field of ordered mesoporous material research.

## 4.3 Polypropylene glycol as a swelling agent: synthesis of multilamellar vesicular silica

Multilamellar vesicular (MLV) silica structures consist of concentric silica shells and voids in alternation (Figure 1.8). MLV silica materials are normally obtained using amphiphilic molecules of different chain lengths as templating agents. After the initial MLV silica reports, in which biomimetic approaches and ionic surfactants were used, many reports regarding the synthesis of MLV silica using P123 as the templating agent and various swelling agents emerged.

In this section, studies regarding the preparation of silica MLVs based on the synthesis of COK-12 are presented, using sodium silicate as the silica source, P123 as a structure directing agent and polypropylene glycol (PPG) as a micellar swelling agent. The selection of PPG was based on previous studies<sup>126</sup>.

SEM micrographs (Figure 4.7) revealed the morphology of MLV-COK-12 materials. For the lowest PPG concentration (MLV-COK-12-0.10, Figure 4.7 a,b), particle morphology is the same as that of P-COK-12 (see Figure 3.1 for reference. At the highest concentration of PPG (MLV-COK-12-2.50, Figure 4.7 c,d), the morphology is that of collapsed spheres in the range of 200-500 nm. This is thought to be the result of the removal of the organic template by calcination. A similar morphology was observed for MLV silica by Yuan, et. al.<sup>59</sup>

The SAXRD patterns of as-calcined MLV materials are presented in Figure 4.8. Only a slight increase in d-spacing is observed with increasing PPG concentration, which hints that there is no increase in pore diameter. However, a loss of  $p6m$  mesoscale ordering for the highest concentrations of PPG is observed, which indicates a significant loss of the hexagonal  $p6m$  phase. This loss of long-range order was confirmed with TEM (Figure 4.9), in which an

obvious decrease in hexagonal mesoporosity is observed for increasing PPG concentration.

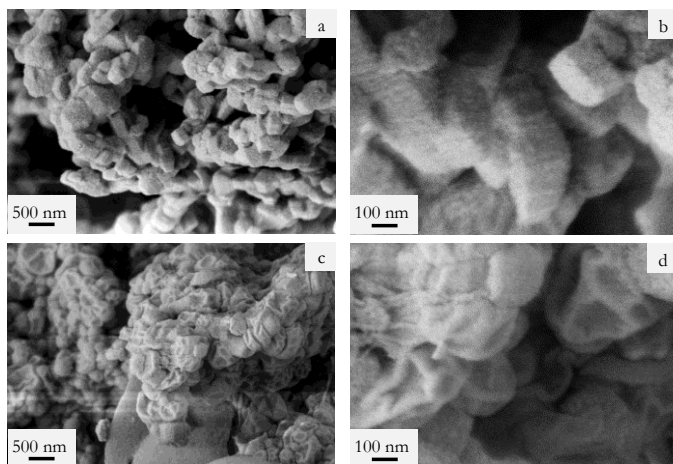


Figure 4.7 SEM micrographs of as-calcined MLV-COK-12: (a,b) MLV-COK-12-0.10: lowest PPG concentration, morphology identical to P-COK-12. (c,d) MLV-COK-12-2.50: highest PPG concentration, collapsed spheres.

TEM micrographs (Figure 4.9) give further insight into the mesoscale transition of MLV materials. With increasing PPG concentration, the MLV phase occurs and coexists with the hexagonal phase (Figure 4.9 d,e). Higher PPG/P123 ratios produce more vesicular particles and fewer particles with cylindrical pores, until no particles with  $p6m$  mesophase were observed (Figure 4.9 h). It is not possible to report a single TEM pore size for MLV materials, given that the distance between the walls of MLV particles varies from 10 up to 30 nm for single samples. The thickness of the silica walls also tends to be inconsistent, however for most samples it varies between 7.2 and 10.6 nm, reaching up to 19.7 nm.

The shape of MLVs is irregular; not all MLV particles have a regular circumference (Figure 4.9 e, f). The walls of most of the observed MLVs are curved inward, similar to a deflated balloon.

### 4.3 Polypropylene glycol as a swelling agent

This could be the result of calcination to remove the PPG/P123; the creation of a void between silica walls could destabilize the structure to yield irregular spheroids. This is consistent with the information obtained from SEM micrographs (Figure 4.7).

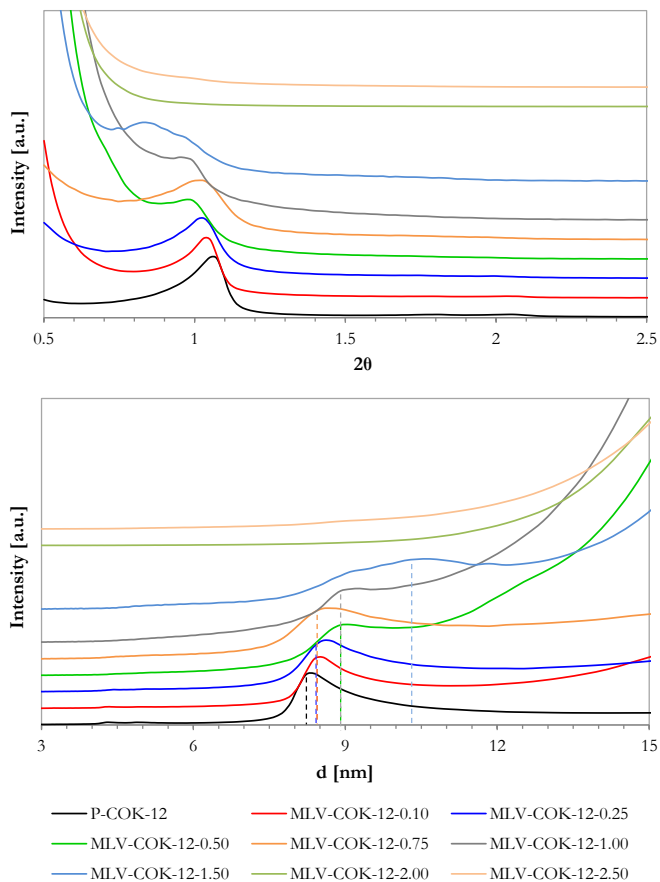


Figure 4.8 Top: SAXRD pattern of as-calcined MLV-COK-12. Patterns have been normalized to the (100) peak and shifted for comparison. P-COK-12 pattern is shown for comparison. At the highest PPG concentration, long-range ordering is lost. Bottom: d-spacing (shown for the (100) family of planes). See Table 4.4 for more information.

The nitrogen adsorption-desorption isotherms of MLV materials are shown in Figure 4.10. All isotherms were classified as type IV isotherms, characteristic of mesoporous materials. A progression from type H1 hysteresis to type H2 hysteresis occurred with increasing PPG concentration. The first clear tendency to H2 was observed for MLV-COK-12-0.25. H2 hysteresis is normally associated to “ink-bottle” type pores. In the case of MLV materials however, cylindrical pores coexist with the larger porosity resulting from the formation of silica vesicles. This contribution is responsible for a shift in the type of hysteresis. The nitrogen uptake as seen in the adsorption branches occurs at a broader relative pressure range, which is an indication of a broadening of the pore size distribution, associated to the appearance of porosity resulting from the voids between the silica layers in MLV materials.

In this regard, as the concentration of PPG increases, it is evident that the mesopore size distribution becomes broader, with the slope of the adsorption branch corresponding to capillary condensation decreasing as PPG concentration increases. However, there is uptake of nitrogen at relative pressure values of 0.95 and above. This indicates that there is a narrower pore size distribution of larger mesopores, which was attributed to the porosity corresponding to the void between silica walls in MLVs.

The pore size distribution as estimated by NLDFT is shown in Figure 4.11 and is presented to illustrate the contribution of mesopores to the total porosity of the sample. It is evident that the contribution of mesopores to the total pore volume decreases with an increase of PPG concentration, which is in line with the finding that the hexagonal mesophase is progressively lost. The contribution of mesopores ranges from 89 % for the MLV-COK-12-0.10 sample to 56 % for the MLV-COK-12-2.50 sample.

### 4.3 Polypropylene glycol as a swelling agent

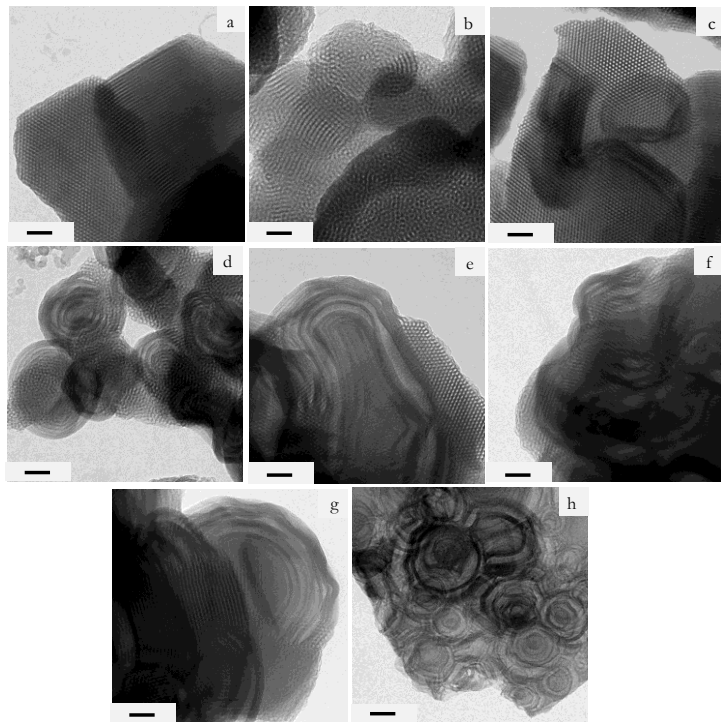


Figure 4.9 TEM micrographs with pore detail of as-calcined MLV-COK-12. (a) Standard P-COK-12 (b) MLV-COK-12-0.10 (c) MLV-COK-12-0.25 (d) MLV-COK-12-0.50 (e) MLV-COK-12-0.75 (f) MLV-COK-12-1.00 (g) MLV-COK-12-1.50 (h) MLV-COK-12-2.50. Bar represents 50 nm.

#### 4 Tailoring the mesostructure of COK-12

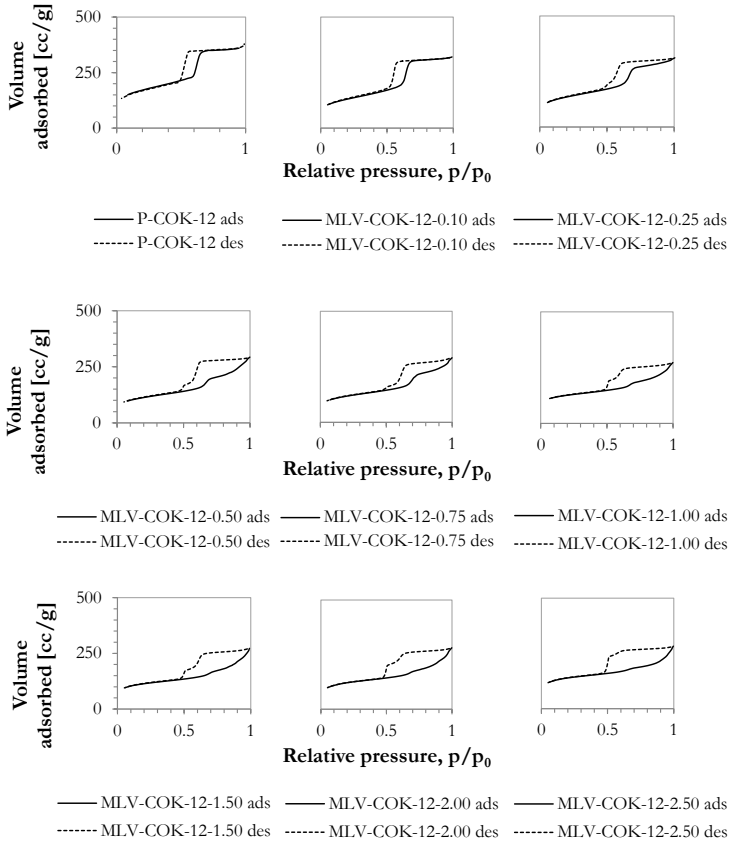


Figure 4.10 Nitrogen adsorption-desorption isotherms of as-calcined MLV-COK-12. The isotherms are type IV with H1 hysteresis until a shift to H2 hysteresis is observed for MLV-COK-12-0.50. P-COK-12 isotherm is shown for comparison.

### 4.3 Polypropylene glycol as a swelling agent

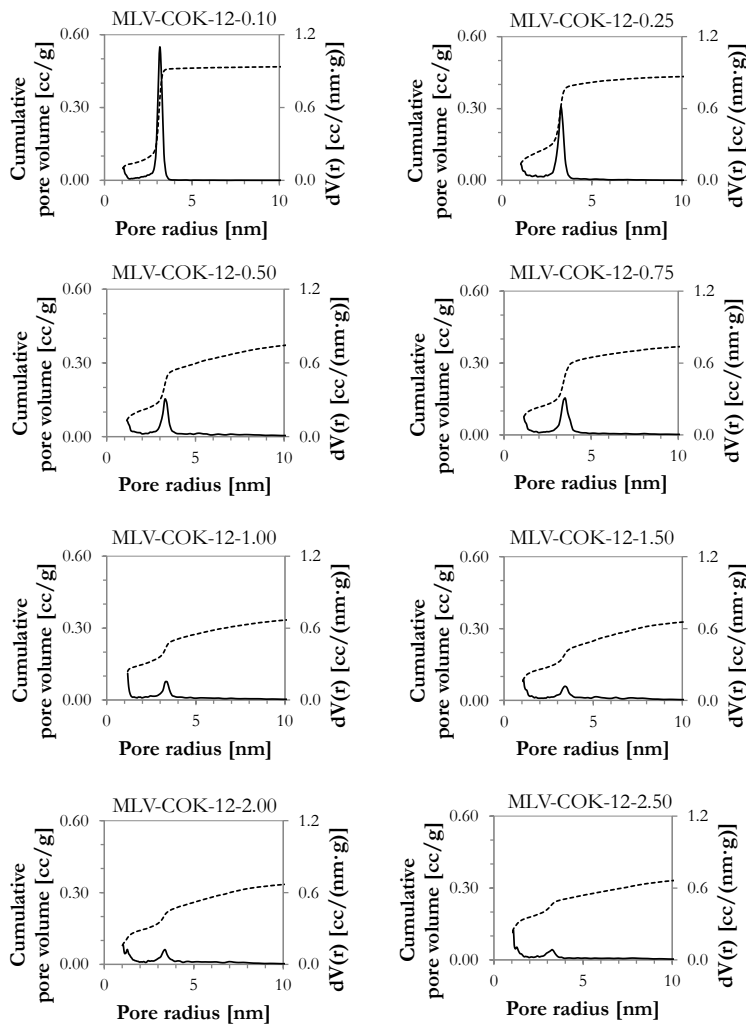


Figure 4.11 Pore size distribution of as-calcined MLV-COK-12 as determined by the NLDFT method. Solid line represents pore size distribution. Dashed line represents cumulative pore volume. A loss of mesoporosity was observed with increasing PPG concentration.

Table 4.4 Properties of as-calcined MLV-COK-12 synthesized using polypropylene glycol (PPG) as a micellar swelling agent.

Material	Type <sup>a</sup>	H <sup>b</sup>	d <sub>100</sub> <sup>a</sup> [nm]	V <sup>c</sup> [cc/g]	S <sub>BET</sub> <sup>f</sup> [m <sup>2</sup> /g]
P-COK-12	IV	H1	8.39	0.640	647.7
MLV-COK-12-0.10	IV	H1/H2	8.73	0.475	440.3
MLV-COK-12-0.25	IV	H1/H2	8.64	0.453	452.3
MLV-COK-12-0.50	IV	H2	9.00	0.430	372.9
MLV-COK-12-0.75	IV	H2	8.67	0.422	386.4
MLV-COK-12-1.00	IV	H2	9.01	0.394	398.7
MLV-COK-12-1.50	IV	H2	10.60	0.389	368.8
MLV-COK-12-2.00	IV	H2	-	0.407	395.8
MLV-COK-12-2.50	IV	H2	-	0.403	445.8

<sup>a</sup> Type of isotherm<sup>b</sup> Type of hysteresis<sup>c</sup> Interplanar distance between (100) planes estimated by SAXRD<sup>d</sup> Pore volume estimated from the adsorption isotherm<sup>e</sup> Specific surface area estimated by BET

The properties of MLV materials prepared using PPG as a swelling agent are shown in Table 4.4. The properties of P-COK-12 are shown for comparison.

As was previously mentioned, PPG was chosen as a micellar swelling agent with the intent to produce COK-12 with enlarged hexagonally-ordered pores. The phase transition from hexagonal to MLV silica using PPG was unexpected and has not been reported thus far. Moreover, studies regarding the formation of a lamellar phase for the triblock copolymer used as a templating agent through this work, P123, could not be found. Previous studies concerning the use of PPG as a swelling agent in systems with PEO-PPO-PEO type templates report an increase in pore diameter, without phase transition for silica systems<sup>126–128</sup>, and with a transition to MCF for ordered mesoporous titania<sup>129</sup>. The unexpected phase transition from hexagonal to MLV silica observed in this work is addressed in terms of the aggregation and packing behavior of the templating phase below.

### 4.3 Polypropylene glycol as a swelling agent

Given that the structure of PPG ( $(C_3H_8O_2)_n$ , molecular weight  $\sim 2000$  mol/g,  $n \sim 25$ ) is the same as that of the hydrophobic block of P123 ( $(C_3H_8O_2)_n$ , molecular weight  $\sim 5800$  mol/g,  $n \sim 70$ , Figure 1.4), a migration of PPG towards PPO is expected, thus enlarging the hydrophobic block of P123.

Considering an enlargement of the hydrophobic block of P123, a phase transition such as that reported by Wanka, et.al.<sup>130</sup> (Figure 4.12) is expected. Generally, a lamellar phase appears for a PPO/PEO molar ratio of around 7, and as the mass of the PPO block increases, the copolymer concentration required for forming subsequent phases decreases<sup>131</sup>. The triblock copolymers depicted in Figure 4.12 have the same PPO block size. The lamellar phase is not present for P123 (Figure 4.12 left). However, by assuming that the more hydrophobic L121 ( $PEO_5PPO_{68}PEO_5$ ) and P123 with an enlarged PPG hydrophobic block ( $PEO_{20}PPO_{70+PPG \text{ content}}PEO_{20}$ ) are similar regarding the ratio of hydrophobic to hydrophilic block volume, it can also be assumed that their aggregation behavior is similar. With a decrease in the size of the PEO block (or alternatively, an increase in the PPO block as in the case of P123 with PPG content) the hexagonal phase disappears and a lamellar phase appears (Figure 4.12 right). The formation of a vesicle is the second of a two-step process, in which the lamellar phase closes to form a vesicle. The lamellar phase closes as a result of bending to decrease the line tension<sup>132</sup>.

It is well-established that a phase transition in PEO-PPO-PEO type triblock copolymers in aqueous solution occurs with increasing polymer concentration and increasing mass of the hydrophobic PPO block of the polymer<sup>130,131,133,134</sup>. Aside from this, the formation mechanism proposed for COK-12<sup>63</sup> suggests that the addition of silica to the aqueous P123 solution eliminates the steric stabilization of the micelles, enabling fast aggregation. This ease in micellar aggregation in the formation of COK-12 has an important effect in the phase transition observed for MLV materials presented in this work, given that not only is there an increase in the

hydrophobic block of the micelles, but facile micellar aggregation also occurs.

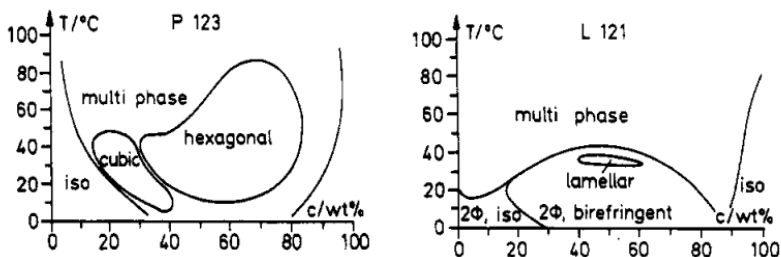


Figure 4.12 Phase diagrams of PEO-PPO-PEO systems in aqueous solution. Left: P123 (PEO<sub>20</sub>PPO<sub>70</sub>PEO<sub>20</sub>) phase diagram. Right: L121 (PEO<sub>5</sub>PPO<sub>68</sub>PEO<sub>5</sub>) phase diagram. The appearance of a lamellar phase can be observed for L121<sup>130</sup>. Reprinted with permission from G. Wanka, H. Hoffmann, and W. Ulbricht: 'Phase Diagrams and Aggregation Behavior of Poly(oxyethylene)-Poly(oxypropylene)-Poly(oxyethylene) Triblock Copolymers in Aqueous Solutions', *Macromolecules*, 1994, **27**(15), 4145-4159. Copyright 1994 American Chemical Society.

With this in mind, the following formation mechanism is proposed. When PPG is incorporated into the micellar P123 solution, which consists of spherical micelles, it migrates toward the hydrophobic block, thus enlarging it. This enlargement is associated to an increase in the average packing parameter of the micelles, which could induce the formation of the lamellar phase, unreported so far for mesoporous silica synthesis using PPG as a micellar swelling agent. This phase transition is made possible by the characteristic facile aggregation of micelles in COK-12 synthesis, in which steric stabilization between micelles is lifted upon addition of the silica precursor to the synthesis media. The lamellar phase then closes to decrease the line tension, resulting in multilamellar vesicles.

It is interesting to address the coexistence of both hexagonal and MLV phases at different PPG concentrations. As can be seen in Figure 4.12, the appearance of a multi-phase is possible. Although the multi-phase occurs at high temperatures and high

#### 4.4 Conclusions and outlook

copolymer concentration, it is possible that the effect of the PPG-silica interaction as well as the influence of the buffer enable the existence of both phases. These effects are out of the scope of the present work and the study of these phenomena could be the platform for further fundamental research, to contribute to establishing predictive tailored syntheses for different forms of mesoporous silica.

MLV materials were obtained, demonstrating the coexistence of the hexagonal  $p6m$  phase and the multilamellar MLV phase, with a loss of the  $p6m$  upon increasing PPG concentration. MLV silica has already found potential application in catalysis<sup>135</sup> and drug delivery<sup>136</sup>.

## 4.4 Conclusions and outlook

The use of hexane and polypropylene glycol (PPG) as micellar swelling agents was presented in this section, with the aim to study the flexibility of COK-12 synthesis in term of using said micellar swelling agents for pore enlargement.

It was demonstrated that the use of hexane not only produces an enlargement of the characteristic cylindrical pores of COK-12, but also induces a phase transition from hexagonally-ordered to multicellular foam (MCF). This phase transition is associated to the formation of “ink-bottle” type pores, with a cell diameter of up to 8.5 nm and a window opening of up to 5.3 nm. The facile synthesis of silica MCF at room temperature and using an inexpensive silica source, based on the COK-12 synthesis, is more economically viable and could be potentially upscaled as was demonstrated in the previous chapter. Potential applications in adsorption/separation of biomolecules make this synthesis of MCF an important contribution to the field of ordered mesoporous material research.

An unexpected phase transition occurred when using PPG with the intent to produce pore enlargement. The incorporation of PPG, which is the same structure as the hydrophobic block of the

triblock copolymer template P123, produced a shift from cylindrical hexagonal to multilamellar vesicular (MLV). It was demonstrated that with increasing PPG concentration, both phases coexist, and the MLV phase becomes the dominant phase at the highest PPG concentration. This phase change has not been demonstrated so far for systems in which PPG is used as a swelling agent. In line with the synthesis of MCF, MLV synthesis is also based on the COK-12 synthesis and is therefore more economically viable and environmentally friendly than other mesoporous silica syntheses, and has the added advantage of being easily upscaleable. MLV silica has already found potential application in catalysis and drug delivery.

## 5 Continuous synthesis of COK-12

In a batch process, the conditions within the process are continually changing. In contrast, in a continuous process, the conditions within the process are largely the same in time. Variations in feed composition, utilities and other variables occur, but normally these changes are either can be averaged. Moreover, continuous processes decrease the time, energy and therefore cost of syntheses by minimizing the number of synthesis steps. With this in mind and with the aim to contribute to more eco-friendly synthesis routes of ordered mesoporous silica, the continuous synthesis of COK-12 is presented in this chapter.

The work carried out in this work regarding the continuous production of COK-12 is based on the concept developed by Jammaer et. al.<sup>63</sup> in which two feed streams, one containing the buffered template solution and the other the silica precursor, are mixed by pumping to immediately produce COK-12 slurry. Two experimental procedures were established, one to test variations in the time of aging of the slurry prepared in continuous mode, and the other to examine the influence of the feed stream flow rates on the quality of the material. Powder COK-12 is presented as the reference material and is used as a basis for comparison in order to assess the quality of monolithic and upscaled materials in terms of pore size and mesoscale ordering. The work presented in this chapter can be found in 'Batch and continuous synthesis upscaling of powder and monolithic ordered mesoporous silica COK-12', *Micro. Meso. Mater.*, 2018, **256**, 102-110.

## 5.1 Conceptual and basic process design and installation

A continuous COK-12 production unit was designed and set up in the Chair of Advanced Ceramics at the Technische Universität Berlin (Figure 5.1).

The continuous synthesis process begins with the preparation of precursor solutions in the jacketed vessels S-1 and S-2 which are kept at 25°C and stirred by overhead stirring. The precursor solutions were then pumped with rotary pumps P-1 and P-2 to the mixing point, where the inlet flow rate ( $Q$ ) was controlled by rotameters R-1 and R-2. At the mixing point M-1, which consists of a Y-piece connector, the precursor solutions met and immediate precipitation of the solid material occurred. The slurry (stream 7) is then collected for subsequent batch processes – filtration, washing, drying and calcination.

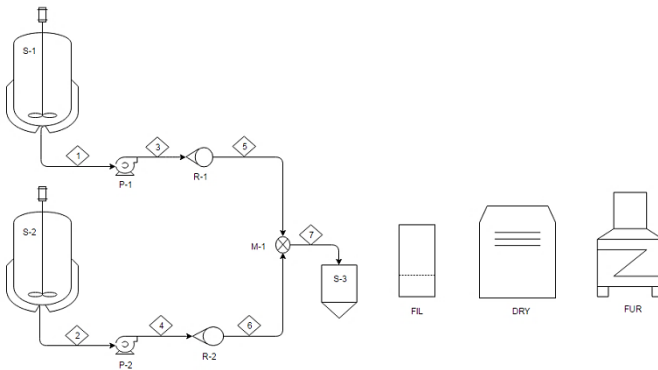


Figure 5.1 Conceptual process flow diagram for the continuous COK-12 production unit of the Chair of Advanced Ceramics at the Technische Universität Berlin. Precursor solution preparation takes place in vessels S-1 and S-2, solutions are pumped to the mixing point M-1 with rotary pumps P-1 and P-2. Flow rates are set by rotameters R-1 and R-2. After mixing, the COK-12 slurry is collected in vessel S-3. After slurry collection, the batch processes of filtration, washing, drying and calcination take place.

## 5.1 Conceptual and basic process design and installation

Table 5.1 Equipment and specifications for the continuous COK-12 production unit.

Device	Specifications
Thermostats (Figure 5.2 a)	Manufacturer: Haake Temperature setting: 25°C
Overhead stirrers (Figure 5.2 c,d)	Manufacturer: IKA Speed set at medium to avoid bubble formation Capacity: 6 liters
Solution preparation vessel S-1 (Figure 5.2 c)	Solution composition [wt%]: 3.40 % P123 91.32 % DIW 3.13 % citric acid 2.16 % trisodium citrate
Solution preparation vessel S-2 (Figure 5.2 d)	Capacity: 20 liters Solution composition [wt %]: 25.74 % sodium silicate 74.26 % DIW
Rotary pumps P-1 and P-2 (Figure 5.2 b)	Manufacturer: Carl Roth GmbH + Co. KG Model 1 rotary pump Maximum flow rate: 4.5 l/min Maximum lift: 0.75 m Inlet diameter: 17 mm Outlet diameter: 13 mm
Rotameters R-1 and R-2 (Figure 5.2 e)	Manufacturer: Key Instruments Acrylic flow meter Minimum flow rate: 10 cm <sup>3</sup> /min Maximum flow rate: 100 cm <sup>3</sup> /min Inlet and outlet diameter: 1/8"
Vacuum filtration FIL (Figure 5.3 a)	Filtering flask capacity: 10 liter Ceramic büchner funnel Vacuum pump Filter paper
Drying cabinet DRY (Figure 5.3 b)	Manufacturer: Heraeus Instruments Temperature setting: 60°C
Furnace FUR (Figure 5.3 c)	Manufacturer: Nabertherm Maximum temperature setting: 500°C



Figure 5.2 Equipment for the continuous synthesis of COK-12. (a) thermostat, (b) overview of the setup and pumps, (c) solution preparation vessel S-1 for sodium silicate solution, (d) solution preparation vessel S-2 for buffered P123 solution, (e) rotameters, (f) collection vessel.

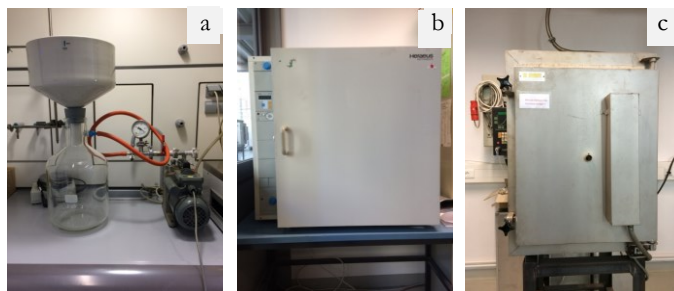


Figure 5.3 Subsequent batch processes of continuous COK-12 synthesis. (a) vacuum filtration/washing, (b) drying in drying cabinet, (c) calcination in furnace.

## 5.2 Continuous production: materials synthesis

Given the limitations in space and material availability, a careful selection of equipment was carried out. The equipment and specifications are summarized in Table 5.1. All piping is silicone tubing (Carl Roth GmbH) and was selected to accommodate the dimensions of the connections of equipment. The dimensions of the equipment and the pumping capacity have led us to estimate a maximum production of 330 g/run of COK-12. A process run includes the continuous synthesis step and all subsequent batch processes. Mixing (overhead stirrers) and pumping were controlled via a user interface in the system design platform LabVIEW.

## 5.2 Continuous production: materials synthesis

In this work, two experiments carried out in the continuous COK-12 production unit, regarding variations in the aging time of the COK-12 slurry and the variations in the flow rate of the feed streams are presented. For both experiments, an amount equivalent to 50 times that of the original COK-12 synthesis was used to prepare the precursor solutions (Table 5.2).

Table 5.2 Synthesis conditions for continuous COK-12 synthesis.

Material	P-COK-12
Batch size	50X
P123 [g]	200
DIW <sup>a</sup> [ml]	5375
Citric acid [g]	184.2
Sodium citrate [g]	127.0
Sodium silicate [g]	520.0
DIW <sup>b</sup> [ml]	1500
DIW <sup>c</sup> [ml]	300.0

<sup>a</sup> For P123 solution

<sup>b</sup> For sodium metasilicate solution

<sup>c</sup> For washing per 100 ml collected sample

For both process runs, the buffered P123 solution was prepared in solution preparation vessel S-2 by completely dissolving P123 in DIW and then incorporating the buffer, and the solution was stirred 24 h. The sodium silicate solution was prepared in vessel S-1 and after homogenization, pumping of the precursor solutions was started. Once steady state was achieved for each solution and the desired flow rate was adjusted by means of rotameters R-1 and R-2, both feed pipes were connected to the mixing point M-1. After mixing, the initial product was discarded for 5 minutes and then sample collection began.

Collected samples were then filtered, washed, dried, calcined and prepared for characterization. The amount of DIW used for washing was determined depending on the volume of each sample, using about 300 ml DIW for 100 ml of collected sample.

### 5.2.1 Variation of the aging time

By keeping the flow rate and the ratio of P123 precursor solution flow rate to sodium silicate precursor solution flow rate ( $Q_{P123}/Q_{sod\text{sil}}$ ) constant, changes in the properties of P-COK-12-CONT due to differences in the aging time after mixing were investigated. Samples were collected in closed glass beakers and kept static for different aging times (Table 5.3) after which they were filtered, washed, dried, calcined and prepared for characterization.

Table 5.3 Experimental conditions for continuous COK-12 synthesis with varying aging time.

Sample name	$Q_{P123}^a$ [ml/min]	$Q_{sod\text{sil}}^b$ [ml/min]	Aging time [h]
P-COK-12-CONT-0h	72	26	0
P-COK-12-CONT-1h	72	26	1
P-COK-12-CONT-6h	72	26	6
P-COK-12-CONT-24h	72	26	24

<sup>a</sup> P123 solution stream flow rate

<sup>b</sup> Sodium silicate solution stream flow rate

## 5.2.2 Variation of the feed stream flow rate

By varying the flow rate  $Q$  of the precursor solution streams, the effect of jetting at the mixing point as a means of homogenization was studied. Calibration of flow meters was carried out by measuring the stream volume for 20 seconds for each standard flow meter position (POS, Table 5.4) presented in this section). To determine flow rates, the calibration equations were used.

Table 5.5 summarizes the calculated experimental conditions. The name of each sample is related to the position of the sodium silicate stream flow meter, which was the selected variable for each experiment. All other parameters were calculated based on this selection.

### *Flow meter calibration*

Calibration of the flow meters was done to determine the real flow rates of each stream at different flow meter positions (POS). Calibration was carried out by measuring the stream volume for 20 seconds for each standard POS. The real flow rate was then calculated by:

$$Q = \frac{\text{measured volume [ml]}}{20 \text{ s}} \times \frac{60 \text{ s}}{1 \text{ min}} [=] \text{ ml/min} \quad (13)$$

and plotted against the respective POS (Figure 5.4).

The following equations were obtained from a linear regression of the measured points and used to determine the position of the flow rate meter for the desired flow rate of the precursor streams:

$$Q_{sodsil} = 0.9092 * POS_{sodsil} - 9.1359, R^2 = 0.9842 \quad (14)$$

$$Q_{P123} = 0.963 * POS_{P123} - 8.4565, R^2 = 0.9844 \quad (15)$$

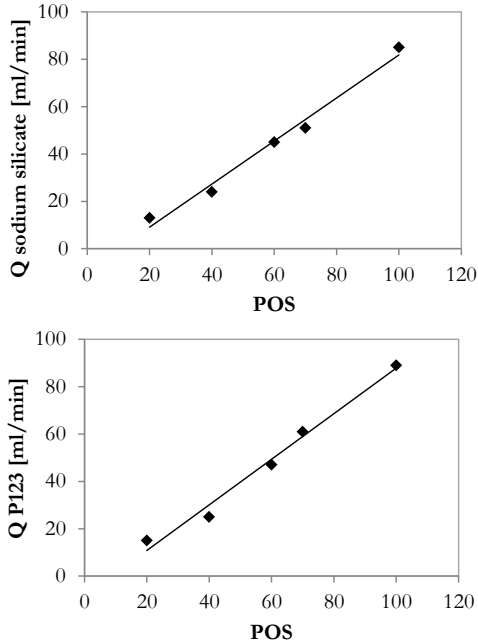


Figure 5.4 Calibration curves of flow rate meters.

Based on this calibration, the real flow rates and  $Q_{P123}/Q_{sodsil}$  ratio were determined. The position of the sodium silicate stream  $POS_{sodsil}$  was fixed and the following calculations were made (see Table 5.7 for all calculations):

$$POS_{sodsil} = 20$$

$$Q_{sodsil} = 0.9092 * 20 - 9.1359 = 9.1 \text{ ml/min}$$

Given the  $Q_{P123}/Q_{sodsil}$  ratio of 2.7 determined from the standard COK-12 synthesis, the estimated flow rate  $Q'_{P123}$  and  $POS'_{P123}$  were calculated:

5.2 Continuous production: materials synthesis

$$Q'_{P123} = 2.7 * 9.1 \text{ ml/min} = 24.5 \text{ ml/min}$$

$$POS'_{P123} = \frac{Q'_{P123} + 8.4565}{0.963} = \frac{24.5 \text{ ml/min} + 8.4565 \text{ ml/min}}{0.963} = 34.2$$

The real position  $POS_{P123}$  was fixed as the nearest multiple of 5 of the calculated position, given the design of the flow rate meter. For this case,  $POS_{P123}$  was fixed as 35, for which the real flow rate  $Q_{P123}$  and real  $Q_{P123}/Q_{\text{sodsil}}$  ratio were calculated:

$$Q_{P123} = 0.963 * 35 - 8.4565 = 25.2 \text{ ml/min}$$

$$\frac{Q_{P123}}{Q_{\text{sodsil}}} = \frac{25.2 \text{ ml/min}}{9.1 \text{ ml/min}} = 2.8$$

Table 5.4 Estimated and real flow rate meter positions and flow rates of feed streams.

Sample name	$POS_{\text{sodsil}}^a$	$Q_{\text{sodsil}}^b$ [ml/min]	$Q'_{P123}^c$ [ml/min]
P-COK-12-CONT-20	20	9,1	24,4
P-COK-12-CONT-25	25	13,6	36,7
P-COK-12-CONT-30	30	18,1	49,0
P-COK-12-CONT-35	35	22,7	61,3
P-COK-12-CONT-40	40	27,2	73,5
P-COK-12-CONT-45	45	31,8	85,8

<sup>a</sup> Selected sodium silicate flow rate meter position

<sup>b</sup> Sodium silicate stream flow rate at POS

<sup>c</sup> Estimated P123 stream flow rate with  $Q_{P123}/Q_{\text{sodsil}}$  ratio of 2.7

Table 5.4 (cont.) Estimated and real flow rate meter positions and flow rates of feed streams.

Sample name	POS <sub>P123</sub> <sup>d</sup>	POS <sub>P123</sub> <sup>e</sup>	Q <sub>P123</sub> <sup>f</sup> [ml/min]	Q <sub>P123</sub> / Q <sub>sodsil</sub>
P-COK-12-CONT-20	34,1	35	25,2	2,8
P-COK-12-CONT-25	46,9	45	34,9	2,6
P-COK-12-CONT-30	59,6	60	49,3	2,7
P-COK-12-CONT-35	72,4	75	63,8	2,8
P-COK-12-CONT-40	85,1	85	73,4	2,7
P-COK-12-CONT-45	97,9	95	83,0	2,6

<sup>d</sup> Estimated P123 flow rate meter position<sup>e</sup> Real P123 flow rate meter position<sup>f</sup> Real P123 stream flow rate

Table 5.5 Experimental conditions for continuous COK-12 synthesis with varying flow rate.

Sample name	Aging time [h]	Q <sub>sodsil</sub> <sup>a</sup> [ml/min]	Q <sub>P123</sub> <sup>b</sup> [ml/min]	Q <sub>P123</sub> / Q <sub>sodsil</sub>
P-COK-12-CONT-20	0	9,1	25,2	2,8
P-COK-12-CONT-25	0	13,6	34,9	2,6
P-COK-12-CONT-30	0	18,1	49,3	2,7
P-COK-12-CONT-35	0	22,7	63,8	2,8
P-COK-12-CONT-40	0	27,2	73,4	2,7
P-COK-12-CONT-45	0	31,8	83,0	2,6

<sup>a</sup> Sodium silicate solution stream flow rate<sup>b</sup> P123 solution stream flow rate

### 5.3 Influence of variation of operation parameters

The following section presents results concerning variations in the time of aging and flow rate of the feed streams in the continuous synthesis of COK-12. Results are presented in comparison to powder COK-12, which is considered a basis for comparison to assess the quality of the materials.

### 5.3.1 Influence of the variation of the aging time on COK-12 mesostructure

SAXRD (Figure 5.5) patterns of P-COK-12-CONT materials with variation in aging time revealed three peaks which were indexed as (100), (110) and (200) reflections. The intensity of (110) and (200) peaks increases with increasing aging time up to 24 h, indicating an increase in long-range ordering. Variations in the position of the (100) peak are attributed to experimental error in the measurement.

The periodicity and hexagonal ordering of the pores of P-COK-12-CONT materials was confirmed with TEM (Figure 5.6). The diameter of the pores and wall thickness estimated by TEM are shown in Table 5.6; these values are in agreement with the lattice parameters  $a$  calculated with SAXRD data and are within the expected range for materials templated with P123. As is the case for P-COK-12, the particle shape corresponds to a hexagonal shape with defined edges (Figure 5.6 d-2).

Comparison of the TEM micrographs of P-COK-12-CONT materials to P-COK-12 (Figure 5.6, compared to Figure 3.4) indicates an increase in the dimensions of the particles. This was attributed to a reduced shear rate that results from mixing via jetting of two streams, as opposed to the vigorous stirring required for the batch synthesis. Zhao et. al. reported that the morphology of OMS can be controlled given the mixing conditions during synthesis; higher mixing rates produced smaller particles<sup>107</sup>. Higher time of aging also appears to increase the uniformity of the mesostructure of P-COK-12-CONT materials.

N<sub>2</sub> adsorption analysis (Figure 5.7) revealed that the adsorption isotherm of P-COK-12-CONT materials with variation in time of aging are type IV isotherms with type H1 hysteresis, indicating open cylindrical mesoporosity with a narrow pore size distribution, as is expected. The specific surface areas determined by the BET method are shown in Table 5.6 in comparison to the standard P-COK-12. P-COK-12-CONT materials have a lower

surface area than the original P-COK-12, ranging from 381 to 501 m<sup>2</sup>/g versus 648 m<sup>2</sup>/g. This could be a result of less efficient washing in comparison to the batch process. Although a fixed amount of washing water is used for each sample taken from the continuous process, it is possible that the solid content in the slurry varies from sample to sample.

The NLDFT pore diameters of P-COK-12-CONT materials with variations in time of aging are between 6.1 and 6.5 nm (Figure 5.8). The pore volume ranges from 0.447 to 0.484 cc/g, which represents a decrease in comparison to the standard P-COK-12.

Table 5.6 summarizes the properties of P-COK-12-CONT materials with variation in the time of aging of the slurry, with a  $Q_{P123}/Q_{\text{sodsil}}$  ratio of 2.8 and  $Q_{P123}$  of 72 ml/min. The properties of the standard P-COK-12 are shown for comparison. It was demonstrated that longer slurry aging times improve the quality of the material.

The success of COK-12 continuous synthesis can be attributed to the same factors as the successful batch synthesis upscaling reported in Chapter 3. On one hand, mixing is not critical in COK-12 synthesis. Jammaer et. al. proposed that COK-12 forms upon reaching a minimum silica content and not due to mixing<sup>63</sup>. As was discussed in section 1.3.5, the limited degree of cross-linking of the silicate network in the PEO shells of P123-silica micelles produces flexible micelles, due to the strong PEO-silicate oligomer interaction. This flexibility in the micelle shells allows for fast aggregation and growth with increasing silica content, for which mixing is not as crucial. In the case of P-COK-12-CONT synthesis, the jetting produced by the two streams at the mixing point was sufficient for mixing of the reagents. The other important factor is the fact the synthesis takes place at room temperature. Any issues that arise from poor heat transfer are circumvented by room temperature synthesis. Although mixing and temperature control are not as critical to obtain a well ordered material, it was demonstrated

### 5.3 Influence of variation of operation parameters

that an increase in the time of aging of the COK-12 slurry slightly increases the degree of ordering of the material.

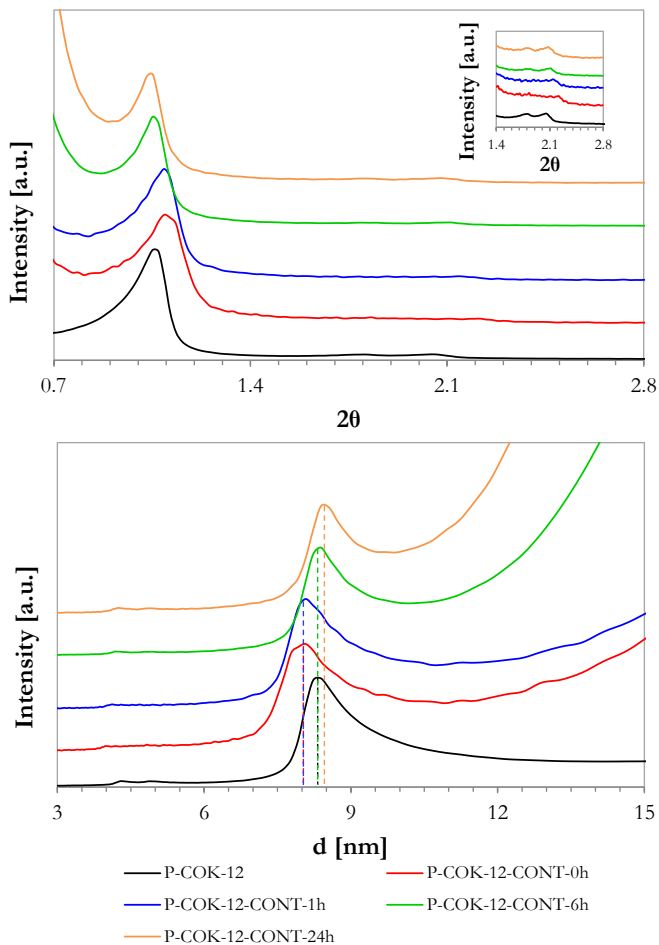


Figure 5.5 Top: SAXRD pattern of as-calcined P-COK-12-CONT with variations in time of aging, with a  $Q_{P123}/Q_{\text{sodasil}}$  ratio of 2.8 and  $Q_{P123}$  of 72 ml/min. Three peaks corresponding to  $p6m$  hexagonal symmetry are observed. Patterns have been normalized to the (100) peak and shifted for comparison. Inlet: detail of second and third peaks (110) and (200). Bottom: d-spacing (shown for the (100) family of planes).

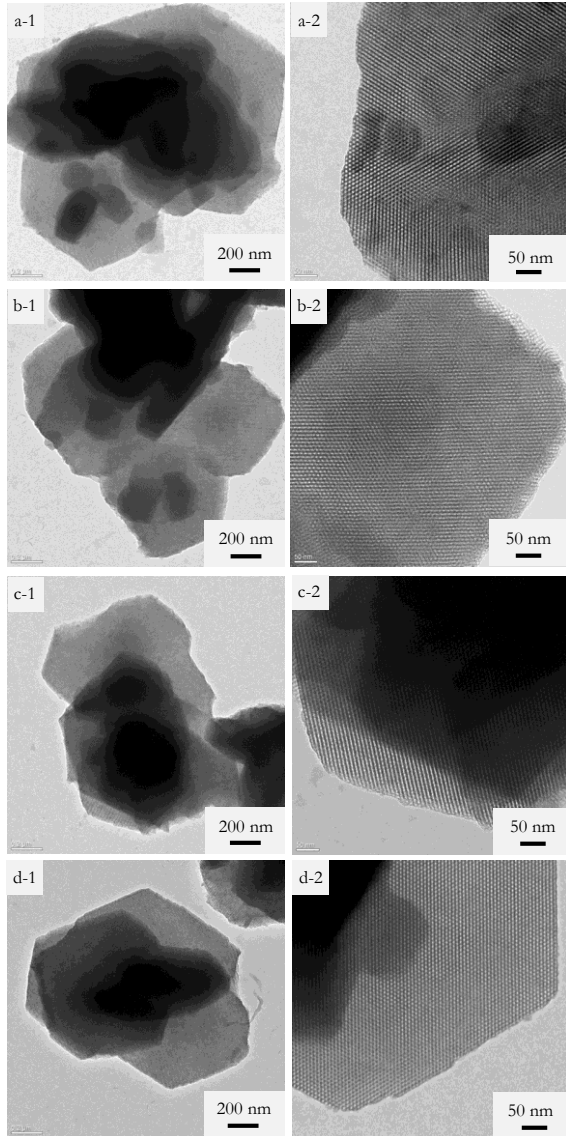


Figure 5.6 TEM micrographs of as-calcined P-COK-12-CONT with variations in time of aging (a) 0 h aging, (b) 1 h aging, (c) 6 h aging, (d) 24 h aging. The shape of the particles as well as long-range 2D hexagonal pore ordering can be seen.

### 5.3 Influence of variation of operation parameters

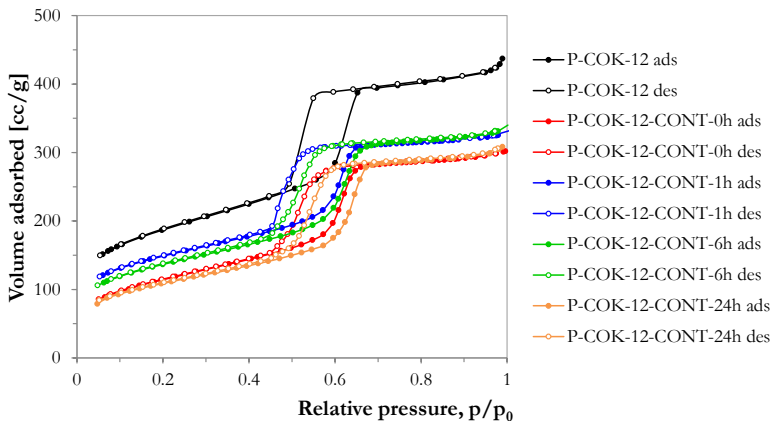


Figure 5.7 Nitrogen adsorption-desorption isotherms for as-calcined P-COK-12-CONT with variations in time of aging with a  $Q_{P123}/Q_{sodasil}$  ratio of 2.8 and  $Q_{P123}$  of 72 ml/min. The isotherms are type IV with H1 hysteresis, characteristic of mesoporous materials. P-COK-12 isotherm is shown for comparison.

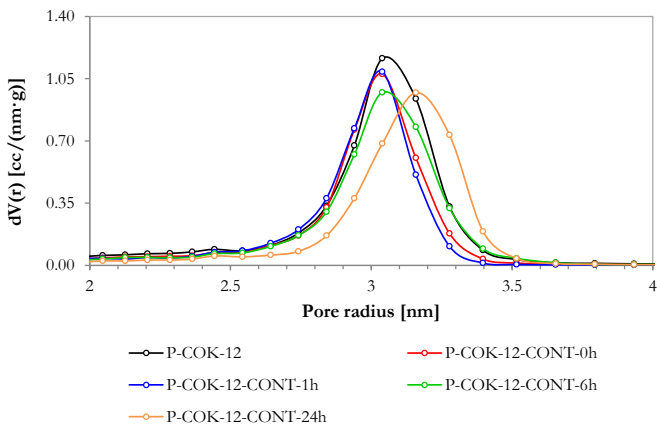


Figure 5.8 Pore size distribution of as-calcined P-COK-12-CONT with variations in time of aging with a  $Q_{P123}/Q_{sodasil}$  ratio of 2.8 and  $Q_{P123}$  of 72 ml/min as determined by the NLDFT method. Pore size distribution of P-COK-12 is shown for comparison. Data is shown only for the relevant pore size range.

Table 5.6 Properties of as-calcined P-COK-12-CONT with variations in time of aging.

Material	$d_{100}^a$ [nm]	$a^b$ [nm]	$P_{TEM}^c$ [nm]	$W_{TEM}^d$ [nm]
P-COK-12	8.39	9.69	5.0	3.9
P-COK-12-CONT-0h	7.93	9.16	5.4	3.8
P-COK-12-CONT-1h	7.93	9.16	5.1	3.6
P-COK-12-CONT-6h	8.39	9.69	5.1	3.9
P-COK-12-CONT-24h	8.39	9.69	5.1	3.9

<sup>a</sup> Interplanar distance between (100) planes estimated by SAXRD

<sup>b</sup> Lattice parameter estimated by SAXRD

<sup>c</sup> Pore diameter estimated by TEM

<sup>d</sup> Wall thickness estimated by TEM

Table 5.6 (cont.) Properties of as-calcined P-COK-12-CONT with variations in time of aging.

Material	Type <sup>e</sup>	H <sup>f</sup>	$P_{DFT}^g$ [nm]	$V_{DFT}^h$ [cc/g]	$S_{BET}^i$ [m <sup>2</sup> /g]
P-COK-12	IV	H1	6.1	0.640	647.7
P-COK-12-CONT-0h	IV	H1	6.1	0.447	402.9
P-COK-12-CONT-1h	IV	H1	6.1	0.484	501.1
P-COK-12-CONT-6h	IV	H1	6.1	0.482	467.5
P-COK-12-CONT-24h	IV	H1	6.5	0.458	381.0

<sup>e</sup> Type of isotherm

<sup>f</sup> Type of hysteresis

<sup>g</sup> Pore diameter estimated by NLDFT

<sup>h</sup> Pore volume estimated by NLDFT

<sup>i</sup> Specific surface area estimated by BET

### 5.3.2 Influence of the variation of the flow rate on COK-12 mesostructure

SAXRD (Figure 5.9) patterns of P-COK-12-CONT materials with variation in flow rate of the feed streams indicate that there was an increase in long-range ordering with an increase in flow rate, evident in the increase of the intensity of (110) and (200) peaks. The pattern of the P-COK-12-CONT-45 sample is nearly identical to that of the standard P-COK-12 pattern. This increase in long-range ordering is an indicator that although a large degree of ordering was obtained at low flow rates, higher flow rates increase the linear velocity of the feed streams and therefore increase the shear rate, producing a more efficient mixing of the P123 and silica precursor solutions. Variations in the position of the (100) peak are attributed to experimental error in the measurement.

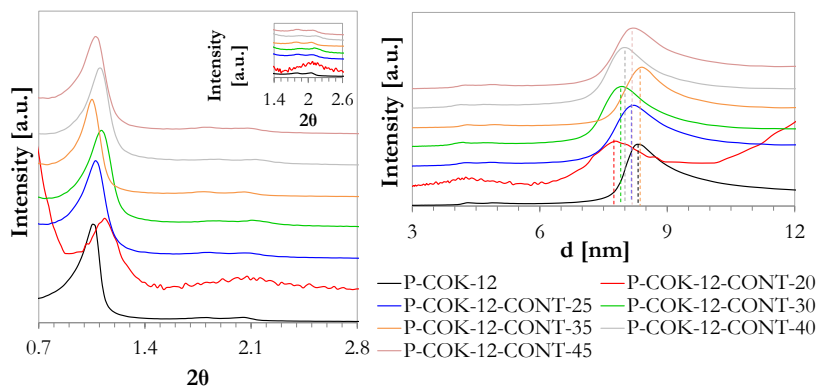


Figure 5.9 SAXRD pattern of as-calcined P-COK-12-CONT with variations in flow rate. Three peaks corresponding to  $p6m$  hexagonal symmetry are observed. Patterns have been normalized to the (100) peak and shifted for comparison. Inlet: detail of second and third peaks (110) and (200). Right: d-spacing (shown for the (100) family of planes).

TEM micrographs (Figure 5.10) confirmed an increase in the degree of ordering with flow rate increase. For the P-COK-12-CONT-40 sample, particles have a more regular and uniform shape and a hexagonal ordering of the porous mesostructure is evident.

The pore sizes and pore volumes estimated by nitrogen sorption analysis are in line with that expected for a material templated with P123, albeit accompanied by a slight decrease in surface area (Figure 5.12, Table 5.7). Graphical evidence (Figure 5.11 and Figure 5.12) confirms the improvement of the regularity of the material with increasing flow rate, namely in the shape of the hysteresis loop of the adsorption isotherm and narrowing of the pore size distribution.

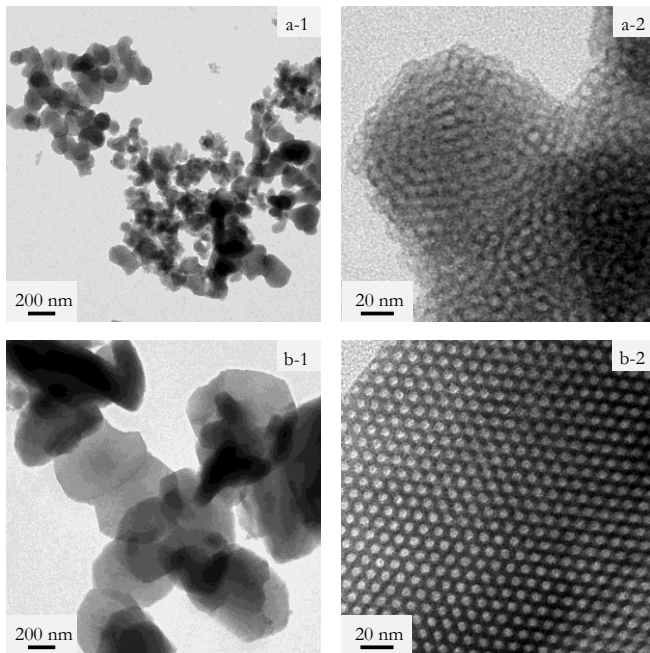


Figure 5.10 TEM micrographs of as-calcined P-COK-12-CONT with varying flow rate. An increase in ordering is visible for the sample with the highest flow rate. (a) P-COK-12-CONT-20. (b) P-COK-12-CONT-40.

### 5.3 Influence of variation of operation parameters

Table 5.7 summarizes the properties of P-COK-12-CONT materials with variation in the flow rate of the feed streams. The properties of the standard P-COK-12 are shown for comparison. It was demonstrated that higher feed stream flow rates improve the quality of the material.

As was discussed in the previous section, the success of COK-12 continuous synthesis is attributed to the fact that mixing and temperature control are not critical factors in COK-12 synthesis. However, although the mixing conditions are not critical to obtain an ordered material, it was demonstrated that higher flow rates yield a material with a higher degree of ordering.

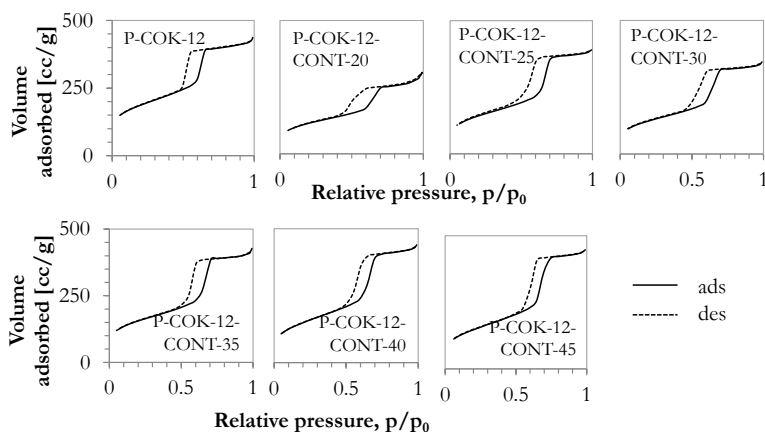


Figure 5.11 Nitrogen adsorption-desorption isotherms for as-calcined P-COK-12-CONT with variations in flow rate (flow rate of sodium silicate stream from 9.1 to 31.8 ml/min and of P123 stream from 25.2 to 83.0 ml/min). See Table 5.7 for flow rate details. The isotherms are type IV with H1 hysteresis, characteristic of mesoporous materials. P-COK-12 isotherm is shown for comparison.

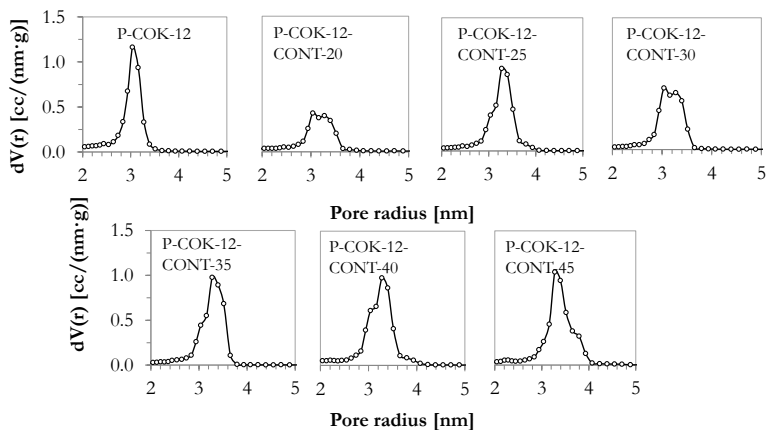


Figure 5.12 Pore size distribution of as-calcined P-COK-12-CONT with variations in flow rate as determined by the NLDFT method. Pore size distribution of P-COK-12 is shown for comparison. Data is shown only for the relevant pore size. See Table 5.7 for flow rate details.

Table 5.7 Properties of as-calcined P-COK-12-CONT with variations in flow rate.

Material	$d_{100}^a$ [nm]	$a^b$ [nm]	Type <sup>c</sup>
P-COK-12	8.39	9.69	IV
P-COK-12-CONT-20	7.79	9.00	IV
P-COK-12-CONT-25	8.22	9.49	IV
P-COK-12-CONT-30	7.95	9.18	IV
P-COK-12-CONT-35	8.39	9.69	IV
P-COK-12-CONT-40	8.02	9.26	IV
P-COK-12-CONT-45	8.20	9.47	IV

<sup>a</sup> Interplanar distance between (100) planes estimated by SAXRD

<sup>b</sup> Lattice parameter estimated by SAXRD

<sup>c</sup> Type of isotherm

## 5.4 Conclusions and outlook

Table 5.7 (cont.) Properties of as-calcined P-COK-12-CONT with variations in flow rate.

Material	H <sup>d</sup>	P <sub>DFT</sub> <sup>e</sup> [nm]	V <sub>DFT</sub> <sup>f</sup> [cc/g]	S <sub>BET</sub> <sup>g</sup> [m <sup>2</sup> /g]
P-COK-12	H1	6.1	0.640	647.7
P-COK-12-CONT-20	H1	6.1	0.425	403.0
P-COK-12-CONT-25	H1	6.6	0.570	504.7
P-COK-12-CONT-30	H1	6.1	0.509	440.8
P-COK-12-CONT-35	H1	6.6	0.625	545.5
P-COK-12-CONT-40	H1	6.6	0.651	538.5
P-COK-12-CONT-45	H1	6.6	0.666	528.0

<sup>d</sup>Type of hysteresis

<sup>e</sup>Pore diameter estimated by NLDFT

<sup>f</sup>Pore volume estimated by NLDFT

<sup>g</sup>Specific surface area estimated by BET

## 5.4 Conclusions and outlook

A continuous COK-12 production unit with a 300 g/run capacity was installed in the Chair of Advanced Ceramics of the Technische Universität Berlin. The production unit was launched and successful continuous COK-12 production was achieved, yielding a material with a high degree of pore ordering and uniform pore size. A study regarding variations in the time of aging of the slurry obtained from this process demonstrated that higher aging times slightly increase the degree of ordering. Similarly, a study concerning the variation of the flow rate of the feed streams demonstrated that higher flow rates increase the degree of ordering, even though an ordered material was obtained even at the lowest flow rate.

The main advantage of a continuous operation versus batch synthesis is the ability to produce a material with consistent quality, given that the conditions within the process are largely the same at any given time. Furthermore, a continuous operation implies a more

economic process, given that the time and energy (in terms of utilities and manpower) required to produce an equivalent batch-synthesized material are generally lower. The overall cost of COK-12 batch synthesis is lower than for the synthesis of SBA-15, for example, and would be even lower when produced in continuous operation. The continuous synthesis of COK-12 is an important milestone in the industrialization of ordered mesoporous silica materials.

## 6 Conclusions and outlook

The ordered mesoporous silica material (OMS) denoted as COK-12 was successfully synthesized and exhibits the expected mesostructure for materials templated with the triblock copolymer P123. The synthesis, conducted at room temperature and quasi-neutral pH, yields hexagonal plate-like particles that exhibit a highly ordered 2D hexagonal cylindrical pore array, with a narrow pore size distribution of 6.1 nm, separated by an amorphous silica wall. By acidification of the synthesis, it was possible to obtain monolithic COK-12 with similar properties as the powder counterpart, albeit with a loss of microporosity. Both the powder and monolithic synthesis were successfully upscaled 25 times in batch without any significant changes in the properties of the materials, yielding up to 65 g of material.

Powder and monolithic COK-12 were used in different forms (powder, granular produced by pressing and monolithic) as a catalyst support for the  $\text{Na}_2\text{WO}_4\text{-Mn/SiO}_2$  catalyst for the oxidative coupling of methane (OCM) reaction. The catalysts were tested to determine their activity, resulting in excellent activity and selectivity to the desired products when the catalyst was used in powder form as opposed to granular form, with performance similar to the catalyst supported on SBA-15. A study concerning the stability of the catalysts after prolonged reaction time resulted in a loss of activity after several hours of use, however the performance of COK-12 supported catalysts was superior to that of the standard catalyst, even after loss of activity. Furthermore, the activity at lower reaction temperatures was studied, demonstrating that the catalyst supported on monolithic COK-12 can be activated at temperatures

below 575°C, which is desirable for industrial application. The  $\text{Na}_2\text{WO}_4\text{-Mn/SiO}_2$  catalytic system supported on ordered mesoporous silica appears to be a promising candidate for application in OCM: However, catalyst design alone is not sufficient to reach the breakthrough required for industrial application, and development of more efficient reactor setups is also required.

The flexibility of the mesostructure of COK-12 was studied by tailoring with the aid of micellar swelling agents. Two new COK-12 phases were obtained: siliceous mesocellular foam (MCF) and multilamellar vesicular (MLV) silica. MCF was obtained by incorporating hexane as a micellar swelling agent in the COK-12 synthesis. The resulting material has an “ink-bottle” pore structure with larger pores, up to 8.5 nm in cell diameter with a pore opening of 5.3 nm. MLV was prepared using polypropylene glycol (PPG) as a micellar swelling agent in the COK-12 synthesis. With increasing PPG concentration, both the MLV and 2D hexagonal mesophases coexist, until at the highest PPG concentration the hexagonal mesophase is lost and only MLV silica is obtained. MCF and MLV materials exhibit a high surface area and porosity, similar to the original COK-12.

With the aim to further upscale COK-12 synthesis, a continuous synthesis process to produce powder COK-12 was successfully installed and tested. Variations in the time of aging of the COK-12 slurry and variations in the flow rate of the feed streams were studied, resulting in materials with properties nearly identical to those of the original COK-12. An increase in the time of aging aids in incrementing the degree of ordering of the material, with aging for 24 hours producing materials of the highest quality. Similarly, higher flow rates produce better quality materials due to better mixing conditions for streams with a higher flow rate.

The materials presented in this work have potential for a wide variety of applications. Their characteristic large surface areas, porous structure and hosting capabilities can be exploited for many applications. For example, enzyme immobilization by physical adsorption in large-pore OMS, such as the MCF materials presented

## *6 Conclusions and outlook*

in this work, is possible and limited by the size of the enzyme and the size of the OMS pore. COK-12 can be used in gas sensing, in humidity sensing or as a host matrix for sensor-active probe molecules. The use of OMS in catalysis has been widely studied, for example in terms of the use of OMS as a support for catalytic nanoparticles which can be synthesized in-situ with the OMS or can be incorporated into the OMS porous structure by encapsulation in organics which solubilize in the micellar template cores. The materials presented in this work can be submitted to post-processing (by freeze-casting, gel-casting, etc.) to yield hierarchically porous materials with pores in the micro, meso and macro scale, which would be especially interesting for applications that require materials with superior mass diffusion properties, such as in heterogeneous catalysis.

Given that the OMS surface has a large concentration of silanol groups, functionalization of the pore walls by post-synthesis grafting or co-condensation opens yet another multitude of applications for COK-12-based materials. Functionalized OMS has applicability in fields as diverse as environmental control as a heavy metal ion adsorbent or in biocatalysis by acting as an enzyme host that provides the possibility of immobilization by covalent bonding to the grafted species. Functionalized OMS also have applicability in the fabrication of smart materials such as stimuli-responsive molecular switches that can be anchored onto an OMS support. OMS with larger particle sizes can be functionalized and have extensive applications in drug delivery, for example regarding the covalent grafting of biomolecules for tissue engineering technology.

The present work paves the way for many possibilities for further developments. Regarding COK-12 batch syntheses, the influence of synthesis parameters on the properties of monolithic COK-12 and upscaled powder and monolithic COK-12 can be studied. For example, the effect of variation of the synthesis temperature on pore size was not addressed in this work but has been reported, as have changes in particle morphology as a result of stirring. Regarding the continuous synthesis of COK-12, the

merging of the continuous and batch processes (filtration, washing and calcination) is the next step in setting up a fully continuous process, which would reduce production time even further. Moreover, in the context of the continuous production unit, many possibilities arise in terms of specialized COK-12 synthesis. In-situ production of any of the direct-synthesis materials described in the previous paragraphs would in principle be possible in continuous mode. Loading with nanoparticles and functionalization by co-condensation could be carried out by using the appropriate reagents in the feed solutions, yielding large quantities of these materials.

The successful continuous synthesis and mesophase tailoring of COK-12 offer promising and exciting possibilities for the future of ordered mesoporous silica synthesis. The facile nature and more environmentally-friendly conditions of the synthesis could lead to industrial production. Mesoscale tailoring with different swelling agents can yield an array of different mesoporous configurations. Possible merging of mesoscale tailoring and continuous synthesis can lead to large-scale production of materials with interesting applications in a multitude of industries, while contributing to the more sustainable production of these materials.

## 7 References

1. K. S. W. Sing, D. H. Everett, R. A. W. Haul, L. Moscou, R. A. Pierotti, J. Rouquerol, and T. Siemieniewska: 'Reporting physisorption data for gas/solid systems: with special reference to the determination of surface area and porosity', *Pure & Appl. Chem.*, **57**(4), 603–619.
2. M. Manzano and M. Vallet-Regí: 'New developments in ordered mesoporous materials for drug delivery', *J. Mater. Chem.*, 2010, **20**(27), 5593, doi: 10.1039/b922651f.
3. A. Walcarius: 'Mesoporous materials and electrochemistry', *Chem. Soc. Rev.*, 2013, **42**(9), 4098, doi: 10.1039/c2cs35322a.
4. T. Wagner, S. Haffer, C. Weinberger, D. Klaus, and M. Tiemann: 'Mesoporous materials as gas sensors', *Chem. Soc. Rev.*, 2013, **42**(9), 4036–4053, doi: 10.1039/C2CS35379B.
5. M. Hartmann: 'Ordered Mesoporous Materials for Bioadsorption and Biocatalysis', *Chem. Mater.*, 2005, **17**(18), 4577–4593, doi: 10.1021/cm0485658.
6. T.-L. Chew, A. L. Ahmad, and S. Bhatia: 'Ordered mesoporous silica (OMS) as an adsorbent and membrane for separation of carbon dioxide (CO<sub>2</sub>)', *Advances in Colloid and Interface Science*, 2010, **153**(1-2), 43–57, doi: 10.1016/j.cis.2009.12.001.
7. K. Moller and T. Bein: 'Inclusion Chemistry in Periodic Mesoporous Hosts', *Chem. Mater.*, 1998, **10**(10), 2950–2963, doi: 10.1021/cm980243e.
8. Q. Yang, J. Liu, L. Zhang, and C. Li: 'Functionalized periodic mesoporous organosilicas for catalysis', *J. Mater. Chem.*, 2009, **19**(14), 1945, doi: 10.1039/b815012e.
9. X. Sheng, J. Kong, Y. Zhou, Y. Zhang, Z. Zhang, and S. Zhou: 'Direct synthesis, characterization and catalytic application of SBA-15 mesoporous silica with heteropolyacid incorporated into their framework', *Microporous and Mesoporous Materials*, 2014, **187**, 7–13, doi: 10.1016/j.micromeso.2013.12.007.

10. T. Cheng, Q. Zhao, D. Zhang, and G. Liu: 'Transition-metal-functionalized ordered mesoporous silicas: An overview of sustainable chiral catalysts for enantioselective transformations', *Green Chem*, 2015, **17**(4), 2100–2122, doi: 10.1039/C4GC02204A.
11. J. Zhu, X. Xie, S. A. C. Carabineiro, P. B. Tavares, J. L. Figueiredo, R. Schomäcker, and A. Thomas: 'Facile one-pot synthesis of Pt nanoparticles /SBA-15: An active and stable material for catalytic applications', *Energy Environ. Sci.*, 2011, **4**(6), 2020, doi: 10.1039/c1ee01040a.
12. L. Usón, M. G. Colmenares, J. L. Hueso, V. Sebastián, F. Balas, M. Arruebo, and J. Santamaría: 'VOCs abatement using thick eggshell Pt/SBA-15 pellets with hierarchical porosity', *Catalysis Today*, 2014, **227**, 179–186, doi: 10.1016/j.cattod.2013.08.014.
13. J. S. Beck, J. C. Vartuli, W. J. Roth, M. E. Leonowicz, C. T. Kresge, K. D. Schmitt, C. T. W. Chu, D. H. Olson, E. W. Sheppard, S. B. McCullen, J. B. Higgins, and J. L. Schlenker: 'A new family of mesoporous molecular sieves prepared with liquid crystal templates', *J. Am. Chem. Soc.*, 1992, **114**(27), 10834–10843, doi: 10.1021/ja00053a020.
14. V. Chiola, J. Ritsko, and C. Vanderpool: 'Process for producing low-bulk density silica', US3556725 A, USA, 26 February 1969.
15. F. Di Renzo, H. Cambon, and R. Dutartre: 'A 28-year-old synthesis of micelle-templated mesoporous silica', *Microporous Materials*, 1997, **10**(4-6), 283–286, doi: 10.1016/S0927-6513(97)00028-X.
16. T. Yanagisawa, T. Shimizu, K. Kuroda, and C. Kato: 'The preparation of alkyltrimethylammonium-kanemite complexes and their conversion to microporous materials', *Bull. Chem. Soc. Jpn.*, 1990, **63**(4), 988–992, doi: 10.1246/bcsj.63.988.
17. C. T. Kresge, M. E. Leonowicz, W. J. Roth, J. C. Vartuli, and J. S. Beck: 'Ordered mesoporous molecular sieves synthesized by

- a liquid-crystal template mechanism', *Nature*, 1992, **359**(6397), 710–712, doi: 10.1038/359710a0.
18. D. Zhao: 'Triblock Copolymer Syntheses of Mesoporous Silica with Periodic 50 to 300 Angstrom Pores', *Science*, 1998, **279**(5350), 548–552, doi: 10.1126/science.279.5350.548.
  19. F. Kleitz, S. Hei Choi, and R. Ryoo: 'Cubic Ia3d large mesoporous silica: Synthesis and replication to platinum nanowires, carbon nanorods and carbon nanotubes', *Chem. Commun.*, 2003, (17), 2136, doi: 10.1039/b306504a.
  20. J. Jammaer, A. Aerts, J. D'Haen, J. W. Seo, and J. A. Martens: 'Convenient synthesis of ordered mesoporous silica at room temperature and quasi-neutral pH', *J. Mater. Chem.*, 2009, **19**(44), 8290, doi: 10.1039/b915273c.
  21. C. Gérardin, J. Reboul, M. Bonne, and B. Lebeau: 'Ecodesign of ordered mesoporous silica materials', *Chem. Soc. Rev.*, 2013, **42**(9), 4217, doi: 10.1039/c3cs35451b.
  22. A. Monnier, F. Schuth, Q. Huo, D. Kumar, D. Margolese, R. S. Maxwell, G. D. Stucky, M. Krishnamurty, P. Petroff, A. Firouzi, M. Janicke, and B. F. Chmelka: 'Cooperative Formation of Inorganic-Organic Interfaces in the Synthesis of Silicate Mesostructures', *Science*, 1993, **261**(5126), 1299–1303, doi: 10.1126/science.261.5126.1299.
  23. Y. Deng, J. Wei, Z. Sun, and D. Zhao: 'Large-pore ordered mesoporous materials templated from non-Pluronic amphiphilic block copolymers', *Chem. Soc. Rev.*, 2013, **42**(9), 4054–4070, doi: 10.1039/c2cs35426h.
  24. Y. Wan and Zhao: 'On the Controllable Soft-Templating Approach to Mesoporous Silicates', *Chem. Rev.*, 2007, **107**(7), 2821–2860, doi: 10.1021/cr068020s.
  25. A. Sayari, B.-H. Han, and Y. Yang: 'Simple Synthesis Route to Monodispersed SBA-15 Silica Rods', *J. Am. Chem. Soc.*, 2004, **126**(44), 14348–14349, doi: 10.1021/ja0478734.
  26. J. P. Thielemann, F. Girgsdies, R. Schlögl, and C. Hess: 'Pore structure and surface area of silica SBA-15: Influence of

- washing and scale-up', *Beilstein J. Nanotechnol.*, 2011, **2**, 110–118, doi: 10.3762/bjnano.2.13.
27. P. Alexandridis: 'Amphiphilic copolymers and their applications', *Current Opinion in Colloid & Interface Science*, 1996, **1**(4), 490–501, doi: 10.1016/S1359-0294(96)80118-X.
  28. I. Schmolka: 'Polyoxyethylene-polyoxypropylene aqueous gels', US3740421A, USA, 19 September 1966.
  29. S. Förster and M. Konrad: 'From self-organizing polymers to nano- and biomaterials', *J. Mater. Chem.*, 2003, **13**(11), 2671–2688, doi: 10.1039/B307512P.
  30. V. Meynen, P. Cool, and E. F. Vansant: 'Verified syntheses of mesoporous materials', *Microporous and Mesoporous Materials*, 2009, **125**(3), 170–223, doi: 10.1016/j.micromeso.2009.03.046.
  31. J. R. Matos, M. Kruk, L. P. Mercuri, M. Jaroniec, L. Zhao, T. Kamiyama, O. Terasaki, T. J. Pinnavaia, and Y. Liu: 'Ordered Mesoporous Silica with Large Cage-Like Pores: Structural Identification and Pore Connectivity Design by Controlling the Synthesis Temperature and Time', *J. Am. Chem. Soc.*, 2003, **125**(3), 821–829, doi: 10.1021/ja0283347.
  32. T.-W. Kim, F. Kleitz, B. Paul, and R. Ryoo: 'MCM-48-like Large Mesoporous Silicas with Tailored Pore Structure: Facile Synthesis Domain in a Ternary Triblock Copolymer–Butanol–Water System', *J. Am. Chem. Soc.*, 2005, **127**(20), 7601–7610, doi: 10.1021/ja042601m.
  33. J. Fan, C. Yu, J. Lei, Q. Zhang, T. Li, B. Tu, W. Zhou, and D. Zhao: 'Low-Temperature Strategy to Synthesize Highly Ordered Mesoporous Silicas with Very Large Pores', *J. Am. Chem. Soc.*, 2005, **127**(31), 10794–10795, doi: 10.1021/ja052619c.
  34. Y. Deng, T. Yu, Y. Wan, Y. Shi, Y. Meng, D. Gu, L. Zhang, Y. Huang, C. Liu, X. Wu, and D. Zhao: 'Ordered Mesoporous Silicas and Carbons with Large Accessible Pores Templated from Amphiphilic Diblock Copolymer Poly(ethylene oxide)-*b*-polystyrene', *J. Am. Chem. Soc.*, 2007, **129**(6), 1690–1697, doi: 10.1021/ja067379v.

## 7 References

35. A. Sayari, Y. Yang, M. Kruk, and M. Jaroniec: 'Expanding the Pore Size of MCM-41 Silicas: Use of Amines as Expanders in Direct Synthesis and Postsynthesis Procedures', *J. Phys. Chem. B*, 1999, **103**(18), 3651–3658, doi: 10.1021/jp984504j.
36. K.-C. Kao and C.-Y. Mou: 'Pore-expanded mesoporous silica nanoparticles with alkanes/ethanol as pore expanding agent', *Microporous and Mesoporous Materials*, 2013, **169**, 7–15, doi: 10.1016/j.micromeso.2012.09.030.
37. M. Kruk and L. Cao: 'Pore Size Tailoring in Large-Pore SBA-15 Silica Synthesized in the Presence of Hexane', *Langmuir*, 2007, **23**(13), 7247–7254, doi: 10.1021/la0702178.
38. X. Zhou, S. Qiao, N. Hao, X. Wang, C. Yu, L. Wang, D. Zhao, and G. Q. Lu: 'Synthesis of Ordered Cubic Periodic Mesoporous Organosilicas with Ultra-Large Pores', *Chem. Mater.*, 2007, **19**(7), 1870–1876, doi: 10.1021/cm062989f.
39. M. Kruk: 'Access to Ultralarge-Pore Ordered Mesoporous Materials through Selection of Surfactant/Swelling-Agent Micellar Templates', *Acc. Chem. Res.*, 2012, **45**(10), 1678–1687, doi: 10.1021/ar200343s.
40. E. Bloch, T. Phan, D. Bertin, P. Llewellyn, and V. Hornebecq: 'Direct synthesis of mesoporous silica presenting large and tunable pores using BAB triblock copolymers: Influence of each copolymer block on the porous structure', *Microporous and Mesoporous Materials*, 2008, **112**(1-3), 612–620, doi: 10.1016/j.micromeso.2007.10.051.
41. P. Schmidt-Winkel, Lukens, Wayne W., D. Zhao, P. Yang, B. F. Chmelka, and G. D. Stucky: 'Mesocellular Siliceous Foams with Uniformly Sized Cells and Windows', *J. Am. Chem. Soc.*, 1999, **121**(1), 254–255, doi: 10.1021/ja983218i.
42. J. Sun, H. Zhang, D. Ma, Y. Chen, X. Bao, A. Klein-Hoffmann, N. Pfänder, and D. S. Su: 'Alkanes-assisted low temperature formation of highly ordered SBA-15 with large cylindrical mesopores', *Chem. Commun.*, 2005, (42), 5343, doi: 10.1039/b509713d.

43. W. Shan, W. Wang, and H. Ru: 'Siliceous mesocellular foams modified via a partitioned cooperative self-assembly process using hexane as pore swelling agent', *Journal of Non-Crystalline Solids*, 2015, **425**, 183–189, doi: 10.1016/j.jnoncrysol.2015.06.007.
44. L. Cao, T. Man, and M. Kruk: 'Synthesis of Ultra-Large-Pore SBA-15 Silica with Two-Dimensional Hexagonal Structure Using Triisopropylbenzene As Micelle Expander', *Chem. Mater.*, 2009, **21**(6), 1144–1153, doi: 10.1021/cm8012733.
45. L. Huang and M. Kruk: 'Synthesis of ultra-large-pore FDU-12 silica using ethylbenzene as micelle expander', *Journal of Colloid and Interface Science*, 2012, **365**(1), 137–142, doi: 10.1016/j.jcis.2011.09.044.
46. L. Cao and M. Kruk: 'Facile method to synthesize platelet SBA-15 silica with highly ordered large mesopores', *Journal of Colloid and Interface Science*, 2011, **361**(2), 472–476, doi: 10.1016/j.jcis.2011.05.076.
47. L. Huang and M. Kruk: 'Versatile Surfactant/Swelling-Agent Template for Synthesis of Large-Pore Ordered Mesoporous Silicas and Related Hollow Nanoparticles', *Chem. Mater.*, 2015, **27**(3), 679–689, doi: 10.1021/cm5028749.
48. J. S. Lettow, Y. J. Han, P. Schmidt-Winkel, P. Yang, D. Zhao, G. D. Stucky, and J. Y. Ying: 'Hexagonal to Mesocellular Foam Phase Transition in Polymer-Templated Mesoporous Silicas', *Langmuir*, 2000, **16**(22), 8291–8295, doi: 10.1021/la000660h.
49. W. Wang, W. Shan, X. Yue, and H. Ru: 'Partitioned cooperative self-assembly process: Taking the mesopore swelling strategy one step further for the preparation of mesocellular foams', *J. Mater. Chem.*, 2012, **22**(8), 3462, doi: 10.1039/c2jm14866h.
50. D. Zhao, Y. Wan, and W. Zhou: 'Ordered mesoporous materials'; 2013, Weinheim, Wiley-VCH.
51. G. Zhou, Y. Chen, J. Yang, and S. Yang: 'From cylindrical-channel mesoporous silica to vesicle-like silica with well-

- defined multilamella shells and large inter-shell mesopores', *J. Mater. Chem.*, 2007, **17**(27), 2839, doi: 10.1039/b703055j.
52. C. V. Kulkarni, W. Wachter, G. Iglesias-Salto, S. Engelskirchen, and S. Ahualli: 'Monoolein: A magic lipid?', *Phys. Chem. Chem. Phys.*, 2011, **13**(8), 3004–3021, doi: 10.1039/C0CP01539C.
53. G. Stucky, Y. Sakamoto, M. Kaneda, O. Terasaki, D. Y. Zhao, J. M. Kim, H. J. Shin, and R. Ryoo: 'Direct imaging of the pores and cages of three-dimensional mesoporous materials', *Nature*, 2000, **408**(6811), 449–453, doi: 10.1038/35044040.
54. P. T. Tanev and T. J. Pinnavaia: 'Biomimetic Templating of Porous Lamellar Silicas by Vesicular Surfactant Assemblies', *Science*, 1996, **271**(5253), 1267–1269, doi: 10.1126/science.271.5253.1267.
55. S. S. Kim: 'Ultrastable Mesostructured Silica Vesicles', *Science*, 1998, **282**(5392), 1302–1305, doi: 10.1126/science.282.5392.1302.
56. P. Kipkemboi, A. Fogden, V. Alfredsson, and K. Flodström: 'Triblock Copolymers as Templates in Mesoporous Silica Formation: Structural Dependence on Polymer Chain Length and Synthesis Temperature', *Langmuir*, 2001, **17**(17), 5398–5402, doi: 10.1021/la001715i.
57. C. J. Brinker, Y. Lu, H. Fan, A. Stump, T. L. Ward, and T. Rieker: 'Aerosol-assisted self-assembly of mesostructured spherical nanoparticles', *Nature*, 1999, **398**(6724), 223–226, doi: 10.1038/18410.
58. Y. F. Zhu, J. L. Shi, and W. H. Shen: 'Synthesis and Characterization of Stable Mesoporous Multilamellar Silica Vesicles', *SSP*, 2007, **121-123**, 473–478, doi: 10.4028/www.scientific.net/SSP.121-123.473.
59. P. Yuan, S. Yang, H. Wang, M. Yu, X. Zhou, G. Lu, J. Zou, and C. Yu: 'Structure transition from hexagonal mesostructured rodlike silica to multilamellar vesicles', *Langmuir: the ACS journal of surfaces and colloids*, 2008, **24**(9), 5038–5043, doi: 10.1021/la8000569.

60. T. Lu, X. Yao, Qing Max Lu, Gao Qing Max, and Y. He: 'Controlled evolution from multilamellar vesicles to hexagonal mesostructures through the addition of 1,3,5-trimethylbenzene', *Journal of Colloid and Interface Science*, 2009, **336**(1), 368–373, doi: 10.1016/j.jcis.2009.03.042.
61. Y. Yao, J. Feng, L. Han, and S. Che: 'Hierarchical multi-lamellar silica vesicle clusters synthesized through self-assembly and mineralization', *RSC Adv*, 2015, **5**(124), 102256–102260, doi: 10.1039/C5RA19123H.
62. K.-Z. Hossain and A. Sayari: 'Synthesis of onion-like mesoporous silica from sodium silicate in the presence of  $\alpha,\omega$ -diamine surfactant', *Microporous and Mesoporous Materials*, 2008, **114**(1-3), 387–394, doi: 10.1016/j.micromeso.2008.01.026.
63. J. Jammaer, T. S. van Erp, A. Aerts, C. E. A. Kirschhock, and J. A. Martens: 'Continuous Synthesis Process of Hexagonal Nanoplates of P 6 m Ordered Mesoporous Silica', *J. Am. Chem. Soc.*, 2011, **133**(34), 13737–13745, doi: 10.1021/ja205627t.
64. R. Takahashi, K. Nakanishi, and N. Soga: 'Aggregation Behavior of Alkoxide-Derived Silica in Sol-Gel Process in Presence of Poly(ethylene oxide)', *Journal of Sol-Gel Science and Technology*, 2000, **17**(1), 7–18, doi: 10.1023/A:1008753718586.
65. O. P. Tkachenko, K. V. Klementiev, E. Löffler, I. Ritzkopf, F. Schüth, M. Bandyopadhyay, S. Grabowski, H. Gies, V. Hagen, M. Muhler, L. Lu, R. A. Fischer, and W. Grünert: 'The structure of zinc and copper oxide species hosted in porous siliceous matrices', *Phys. Chem. Chem. Phys.*, 2003, **5**(19), 4325–4334, doi: 10.1039/B303429A.
66. M. Lindén, S. A. Schunk, and F. Schüth: 'In Situ X-Ray Diffraction Study of the Initial Stages of Formation of MCM-41 in a Tubular Reactor', *Angewandte Chemie International Edition*, 1998, **37**, doi: 10.1002/(SICI)1521-3773(19980403)37:6<821::AID-ANIE821>3.0.CO;2-I.
67. R. Pitchumani, J. J. Heiszwolf, A. Schmidt-Ott, and M.-O. Coppens: 'Continuous synthesis by spray drying of highly stable mesoporous silica and silica–alumina catalysts using

- industrial raw materials', *Microporous and Mesoporous Materials*, 2009, **120**(1-2), 39–46, doi: 10.1016/j.micromeso.2008.07.045.
68. A. Taguchi and F. Schüth: 'Ordered mesoporous materials in catalysis', *Microporous and Mesoporous Materials*, 2005, **77**(1), 1–45, doi: 10.1016/j.micromeso.2004.06.030.
69. M. Varkolu, V. Velpula, S. Ganji, D. R. Burri, and S. R. Rao Kamaraju: 'Ni nanoparticles supported on mesoporous silica (2D, 3D) architectures: Highly efficient catalysts for the hydrocyclization of biomass-derived levulinic acid', *RSC Adv*, 2015, **5**(70), 57201–57210, doi: 10.1039/C5RA10857H.
70. J. Ross, A. van Keulen, M. Hegarty, and K. Seshan: 'The catalytic conversion of natural gas to useful products', *Catalysis Today*, 1996, **30**(1-3), 193–199, doi: 10.1016/0920-5861(96)00035-1.
71. BP: 'BP Statistical review of world energy 2015'; June 2015.
72. J. H. Lunsford: 'Catalytic conversion of methane to more useful chemicals and fuels: A challenge for the 21st century', *Catalysis Today*, 2000, **63**(2-4), 165–174, doi: 10.1016/S0920-5861(00)00456-9.
73. P. Weiland: 'Biogas production: Current state and perspectives', *Appl Microbiol Biotechnol*, 2010, **85**(4), 849–860, doi: 10.1007/s00253-009-2246-7.
74. R. Horn and R. Schlögl: 'Methane Activation by Heterogeneous Catalysis', *Catal Lett*, 2015, **145**(1), 23–39, doi: 10.1007/s10562-014-1417-z.
75. A. Holmen: 'Direct conversion of methane to fuels and chemicals', *Catalysis Today*, 2009, **142**(1-2), 2–8, doi: 10.1016/j.cattod.2009.01.004.
76. G. Keller and M. Bhasin: 'Synthesis of ethylene via oxidative coupling of methane I. Determination of active catalysts', *Journal of Catalysis*, 1982, **73**(1), 9–19, doi: 10.1016/0021-9517(82)90075-6.
77. E. V. Kondratenko and M. Baerns: 'Oxidative Coupling of Methane', in 'Ertl, et al. (Ed.) 2008 – Handbook of Heterogeneous Catalysis'.

78. Y. Su: 'Upper bound on the yield for oxidative coupling of methane', *Journal of Catalysis*, 2003, **218**(2), 321–333, doi: 10.1016/S0021-9517(03)00043-5.
79. U. Zavyalova, M. Holena, R. Schlögl, and M. Baerns: 'Statistical Analysis of Past Catalytic Data on Oxidative Methane Coupling for New Insights into the Composition of High-Performance Catalysts', *ChemCatChem*, 2011, **3**(12), 1935–1947, doi: 10.1002/cctc.201100186.
80. Alexander H. Tulló: 'Siluria's Oxidative Coupling Nears Reality'; July 7, 2014.
81. X. Fang, S. Li, J. Lin, and Y. Chu: 'Oxidative Coupling of Methane on W-Mn Catalysts', *Journal of Molecular Catalysis (China)*, 1992, **6**, 427.
82. S. Arndt, T. Otremba, U. Simon, M. Yildiz, H. Schubert, and R. Schomäcker: 'Mn–Na<sub>2</sub>WO<sub>4</sub>/SiO<sub>2</sub> as catalyst for the oxidative coupling of methane. What is really known?', *Applied Catalysis A: General*, 2012, **425-426**, 53–61, doi: 10.1016/j.apcata.2012.02.046.
83. H. R. Godini, A. Gili, O. Görke, S. Arndt, U. Simon, A. Thomas, R. Schomäcker, and G. Wozny: 'Sol-gel method for synthesis of Mn–Na<sub>2</sub>WO<sub>4</sub>/SiO<sub>2</sub> catalyst for methane oxidative coupling', *Catalysis Today*, 2014, **236**, 12–22, doi: 10.1016/j.cattod.2014.01.005.
84. D. J. Wang, M. P. Rosynek, and J. H. Lunsford: 'Oxidative Coupling of Methane over Oxide-Supported Sodium-Manganese Catalysts', *Journal of Catalysis*, 1995, **155**(2), 390–402, doi: 10.1006/jcat.1995.1221.
85. S. Pak, P. Qiu, and J. H. Lunsford: 'Elementary Reactions in the Oxidative Coupling of Methane over Mn/Na<sub>2</sub>WO<sub>4</sub>/SiO<sub>2</sub> and Mn/Na<sub>2</sub>WO<sub>4</sub>/MgO Catalysts', *Journal of Catalysis*, 1998, **179**(1), 222–230, doi: 10.1006/jcat.1998.2228.
86. A. Palermo, J. P. Holgado Vazquez, A. Lee, M. Tikhov, and R. Lambert: 'Critical influence of the amorphous silica-to-cristobalite phase transition on the performance of Mn/Na<sub>2</sub>WO<sub>4</sub>/SiO<sub>2</sub> catalysts for the oxidative coupling of

- methane', *Journal of Catalysis*, 1998, **177**(2), 259–266, doi: 10.1006/jcat.1998.2109.
87. A. Palermo, J. P. Holgado Vazquez, and R. M. Lambert: 'New efficient catalysts for the oxidative coupling of methane', *Catalysis Letters*, 2000, **68**(3/4), 191–196, doi: 10.1023/A:1019072512423.
88. S.-f. Ji, T.-c. Xiao, S.-b. Li, C.-z. Xu, R.-l. Hou, K. S. Coleman, and M. L. Green: 'The relationship between the structure and the performance of Na-W-Mn/SiO<sub>2</sub> catalysts for the oxidative coupling of methane', *Applied Catalysis A: General*, 2002, **225**(1-2), 271–284, doi: 10.1016/S0926-860X(01)00864-X.
89. S. Ji: 'Surface WO<sub>4</sub> tetrahedron: The essence of the oxidative coupling of methane over M-W-Mn/SiO<sub>2</sub> catalysts', *Journal of Catalysis*, 2003, **220**(1), 47–56, doi: 10.1016/S0021-9517(03)00248-3.
90. J. Wang, L. Chou, B. Zhang, H. Song, J. Zhao, J. Yang, and S. Li: 'Comparative study on oxidation of methane to ethane and ethylene over Na<sub>2</sub>WO<sub>4</sub>-Mn/SiO<sub>2</sub> catalysts prepared by different methods', *Journal of Molecular Catalysis A: Chemical*, 2006, **245**(1-2), 272–277, doi: 10.1016/j.molcata.2005.09.038.
91. U. Simon, O. Görke, A. Berthold, S. Arndt, R. Schomäcker, and H. Schubert: 'Fluidized bed processing of sodium tungsten manganese catalysts for the oxidative coupling of methane', *Chemical Engineering Journal*, 2011, **168**(3), 1352–1359, doi: 10.1016/j.cej.2011.02.013.
92. B. Beck, V. Fleischer, S. Arndt, M. G. Hevia, A. Urakawa, P. Hugo, and R. Schomäcker: 'Oxidative coupling of methane—A complex surface/gas phase mechanism with strong impact on the reaction engineering', *Catalysis Today*, 2014, **228**, 212–218, doi: 10.1016/j.cattod.2013.11.059.
93. R. Koirala, R. Büchel, S. E. Pratsinis, and A. Baiker: 'Oxidative coupling of methane on flame-made Mn-Na<sub>2</sub>WO<sub>4</sub>/SiO<sub>2</sub>: Influence of catalyst composition and reaction conditions', *Applied Catalysis A: General*, 2014, **484**, 97–107, doi: 10.1016/j.apcata.2014.07.013.

94. M. Yildiz, U. Simon, T. Otremba, Y. Aksu, K. Kailasam, A. Thomas, R. Schomäcker, and S. Arndt: 'Support material variation for the  $Mn_xO_y-Na_2WO_4/SiO_2$  catalyst', *Catalysis Today*, 2014, **228**, 5–14, doi: 10.1016/j.cattod.2013.12.024.
95. T. Serres, C. Aquino, C. Mirodatos, and Y. Schuurman: 'Influence of the composition/texture of Mn–Na–W catalysts on the oxidative coupling of methane', *Applied Catalysis A: General*, 2015, **504**, 509–518, doi: 10.1016/j.apcata.2014.11.045.
96. T. W. Elkins and H. E. Hagelin-Weaver: 'Characterization of  $Mn-Na_2WO_4/SiO_2$  and  $Mn-Na_2WO_4/MgO$  catalysts for the oxidative coupling of methane', *Applied Catalysis A: General*, 2015, **497**, 96–106, doi: 10.1016/j.apcata.2015.02.040.
97. M. Yildiz, Y. Aksu, U. Simon, K. Kailasam, O. Goerke, F. Rosowski, R. Schomäcker, A. Thomas, and S. Arndt: 'Enhanced catalytic performance of  $Mn_xO_y-Na_2WO_4/SiO_2$  for the oxidative coupling of methane using an ordered mesoporous silica support', *Chem. Commun.*, 2014, **50**(92), 14440–14442, doi: 10.1039/C4CC06561A.
98. H. Schnablegger and Y. Singh: 'The SAXS Guide: Getting acquainted with the principle', 3rd edn; 2013, Austria, Anton Paar GmbH.
99. G. Q. Lu and X. S. Zhao: 'Nanoporous materials: Science and engineering / edited by G.Q. Lu, X.S. Zhao'; 2004, London, Imperial College Press.
100. S. Brunauer, P. H. Emmett, and E. Teller: 'Adsorption of Gases in Multimolecular Layers', *J. Am. Chem. Soc.*, 1938, **60**(2), 309–319, doi: 10.1021/ja01269a023.
101. E. Keng: 'Air and helium pycnometer', *Powder Technology*, 1969, **3**(1), 179–180, doi: 10.1016/0032-5910(69)80070-7.
102. H. Minakuchi, K. Nakanishi, N. Soga, N. Ishizuka, and N. Tanaka: 'Octadecylsilylated porous silica rods as separation media for reversed-phase liquid chromatography', *Analytical chemistry*, 1996, **68**(19), 3498–3501, doi: 10.1021/ac960281m.
103. A. Sachse, A. Galarneau, F. Fajula, F. Di Renzo, P. Creux, and B. Coq: 'Functional silica monoliths with hierarchical uniform

- porosity as continuous flow catalytic reactors', *Microporous and Mesoporous Materials*, 2011, **140**(1-3), 58–68, doi: 10.1016/j.micromeso.2010.10.044.
104. J. Babin, J. Iapichella, B. Lefèvre, C. Biolley, J.-P. Bellat, F. Fajula, and A. Galarneau: 'MCM-41 silica monoliths with independent control of meso- and macroporosity', *New J. Chem.*, 2007, **31**(11), 1907, doi: 10.1039/B711544J.
105. J.-H. Smått, S. Schunk, and M. Lindén: 'Versatile Double-Templating Synthesis Route to Silica Monoliths Exhibiting a Multimodal Hierarchical Porosity', *Chem. Mater.*, 2003, **15**(12), 2354–2361, doi: 10.1021/cm0213422.
106. M. Impéror-Clerc, P. Davidson, and A. Davidson: 'Existence of a Microporous Corona around the Mesopores of Silica-Based SBA-15 Materials Templated by Triblock Copolymers', *J. Am. Chem. Soc.*, 2000, **122**(48), 11925–11933, doi: 10.1021/ja002245h.
107. D. Zhao, J. Sun, Q. Li, and G. D. Stucky: 'Morphological Control of Highly Ordered Mesoporous Silica SBA-15', *Chem. Mater.*, 2000, **12**(2), 275–279, doi: 10.1021/cm9911363.
108. C. Jo, K. Kim, and R. Ryoo: 'Syntheses of high quality KIT-6 and SBA-15 mesoporous silicas using low-cost water glass, through rapid quenching of silicate structure in acidic solution', *Microporous and Mesoporous Materials*, 2009, **124**(1-3), 45–51, doi: 10.1016/j.micromeso.2009.04.037.
109. R. H. Perry and D. W. Green: 'Perry's chemical engineers' handbook', 8th edn; 2008, New York, McGraw-Hill Professional; London : McGraw-Hill [distributor].
110. A. Katiyar, S. Yadav, P. G. Smirniotis, and N. G. Pinto: 'Synthesis of ordered large pore SBA-15 spherical particles for adsorption of biomolecules', *Journal of chromatography. A*, 2006, **1122**(1-2), 13–20, doi: 10.1016/j.chroma.2006.04.055.
111. M. A. Smith, A. Zoelle, Y. Yang, R. M. Rioux, N. G. Hamilton, K. Amakawa, P. K. Nielsen, and A. Trunschke: 'Surface roughness effects in the catalytic behavior of vanadia

- supported on SBA-15', *Journal of Catalysis*, 2014, **312**, 170–178, doi: 10.1016/j.jcat.2014.01.011.
112. T. Amatani, K. Nakanishi, K. Hirao, and T. Kodaira: 'Monolithic Periodic Mesoporous Silica with Well-Defined Macropores', *Chem. Mater.*, 2005, **17**(8), 2114–2119, doi: 10.1021/cm048091c.
113. C. Liang, S. Dai, and G. Guiochon: 'Use of gel-casting to prepare HPLC monolithic silica columns with uniform mesopores and tunable macrochannels', *Chem. Commun.*, 2002, (22), 2680–2681, doi: 10.1039/b207798a.
114. N. A. Melosh, P. Lipic, F. S. Bates, F. Wudl, G. D. Stucky, G. H. Fredrickson, and B. F. Chmelka: 'Molecular and Mesoscopic Structures of Transparent Block Copolymer–Silica Monoliths', *Macromolecules*, 1999, **32**(13), 4332–4342, doi: 10.1021/ma9817323.
115. P. Feng, X. Bu, G. D. Stucky, and D. J. Pine: 'Monolithic Mesoporous Silica Templated by Microemulsion Liquid Crystals', *J. Am. Chem. Soc.*, 2000, **122**(5), 994–995, doi: 10.1021/ja992921j.
116. R. C. Merrill and R. W. Spencer: 'The Gelation of Sodium Silicate. Effect of Sulfuric Acid, Hydrochloric Acid, Ammonium Sulfate, and Sodium Aluminate', *J. Phys. Chem.*, 1950, **54**(6), 806–812, doi: 10.1021/j150480a009.
117. V. V. Potapov, A. A. Serdan, V. N. Kashpura, V. A. Gorbach, N. A. Tyurina, and S. V. Zubakha: 'Polycondensation of orthosilicic acid in hydrothermal solutions at different temperatures, pH values, and ionic strengths', *Glass Phys Chem*, 2007, **33**(1), 44–49, doi: 10.1134/S1087659607010063.
118. X. Y. Bao and X. S. Zhao: 'Morphologies of large-pore periodic mesoporous organosilicas', *The journal of physical chemistry. B*, 2005, **109**(21), 10727–10736, doi: 10.1021/jp050449k.
119. M. G. Colmenares, U. Simon, M. Yildiz, S. Arndt, R. Schomaecker, A. Thomas, F. Rosowski, A. Gurlo, and O. Goerke: 'Oxidative coupling of methane on the Na<sub>2</sub>WO<sub>4</sub>-

- Mn<sub>x</sub>O<sub>y</sub> catalyst supported on ordered mesoporous silica: COK-12 as an inexpensive alternative to SBA-15', *Catalysis Communications*, 2016, doi: 10.1016/j.catcom.2016.06.025.
120. S. Sadjadi, S. Jašo, H. R. Godini, S. Arndt, M. Wollgarten, R. Blume, O. Görke, R. Schomäcker, G. Wozny, and U. Simon: 'Feasibility study of the Mn–Na<sub>2</sub>WO<sub>4</sub>/SiO<sub>2</sub> catalytic system for the oxidative coupling of methane in a fluidized-bed reactor', *Catal. Sci. Technol.*, 2015, **5**(2), 942–952, doi: 10.1039/C4CY00822G.
121. G. D. Nipan: 'Phase states of Na/W/Mn/SiO<sub>2</sub> composites at temperatures of catalytic oxidative coupling of methane', *Inorg Mater*, 2014, **50**(10), 1012–1017, doi: 10.1134/S0020168514100112.
122. S. Mahmoodi, M. R. Ehsani, and S. M. Ghoreishi: 'Effect of promoter in the oxidative coupling of methane over synthesized Mn/SiO<sub>2</sub> nanocatalysts via incipient wetness impregnation', *Journal of Industrial and Engineering Chemistry*, 2010, **16**(6), 923–928, doi: 10.1016/j.jiec.2010.09.007.
123. J. Zhao, F. Gao, Y. Fu, W. Jin, P. Yang, and D. Zhao: 'Biomolecule separation using large pore mesoporous SBA-15 as a substrate in high performance liquid chromatography', *Chem. Commun.*, 2002, (7), 752–753, doi: 10.1039/b110637f.
124. Y. Ma, L. Qi, J. Ma, Y. Wu, O. Liu, and H. Cheng: 'Large-pore mesoporous silica spheres: Synthesis and application in HPLC', *Colloids and Surfaces A: Physicochemical and Engineering Aspects*, 2003, **229**(1-3), 1–8, doi: 10.1016/j.colsurfa.2003.08.010.
125. A. Popat, S. B. Hartono, F. Stahr, J. Liu, S. Z. Qiao, and G. Qing Max Lu: 'Mesoporous silica nanoparticles for bioadsorption, enzyme immobilisation, and delivery carriers', *Nanoscale*, 2011, **3**(7), 2801–2818, doi: 10.1039/c1nr10224a.
126. X. Cui, J.-H. Ahn, W.-C. Zin, W.-J. Cho, and C.-S. Ha: 'Polypropylene glycol as a swelling agent for the synthesis of mesoporous silica (SBA-15) by amphiphilic block copolymer templating', in 'Nanotechnology in Mesostructured Materials,

- Proceedings of the 3rd International Materials Symposium', 117–120; 2003, Elsevier.
127. B.-G. Park, W. Guo, X. Cui, J. Park, and C.-S. Ha: 'Preparation and characterization of organo-modified SBA-15 by using polypropylene glycol as a swelling agent', *Microporous and Mesoporous Materials*, 2003, **66**(2-3), 229–238, doi: 10.1016/j.micromeso.2003.09.013.
  128. M. H. Sørensen, R. W. Corkery, J. S. Pedersen, J. Rosenholm, and P. C. Alberius: 'Expansion of the F127-templated mesostructure in aerosol-generated particles by using polypropylene glycol as a swelling agent', *Microporous and Mesoporous Materials*, 2008, **113**(1-3), 1–13, doi: 10.1016/j.micromeso.2007.10.045.
  129. Q. L. Wu and S. E. Rankin: 'Tuning the Mesopore Size of Titania Thin Films Using a Polymeric Swelling Agent', *J. Phys. Chem. C*, 2011, **115**(24), 11925–11933, doi: 10.1021/jp2021193.
  130. G. Wanka, H. Hoffmann, and W. Ulbricht: 'Phase Diagrams and Aggregation Behavior of Poly(oxyethylene)-Poly(oxypropylene)-Poly(oxyethylene) Triblock Copolymers in Aqueous Solutions', *Macromolecules*, 1994, **27**(15), 4145–4159, doi: 10.1021/ma00093a016.
  131. I. W. Hamley: 'Block copolymers in solution: Fundamentals and applications / Ian Hamley'; 2005, Chichester, John Wiley.
  132. M. Antonietti and S. Förster: 'Vesicles and Liposomes: A Self-Assembly Principle Beyond Lipids', *Adv. Mater.*, 2003, **15**(16), 1323–1333, doi: 10.1002/adma.200300010.
  133. P. Alexandridis, J. F. Holzwarth, and T. A. Hatton: 'Micellization of Poly(ethylene oxide)-Poly(propylene oxide)-Poly(ethylene oxide) Triblock Copolymers in Aqueous Solutions: Thermodynamics of Copolymer Association', *Macromolecules*, 1994, **27**(9), 2414–2425, doi: 10.1021/ma00087a009.
  134. P. Linse: 'Micellization of poly(ethylene oxide)-poly(propylene oxide) block copolymers in aqueous solution', *Macromolecules*, 1993, **26**(17), 4437–4449, doi: 10.1021/ma00069a007.

## 7 References

135. G. Zhou, Y. Chen, and S. Yang: 'Comparative studies on catalytic properties of immobilized *Candida rugosa* lipase in ordered mesoporous rod-like silica and vesicle-like silica', *Microporous and Mesoporous Materials*, 2009, **119**(1-3), 223–229, doi: 10.1016/j.micromeso.2008.10.013.
136. Y. Zhu, J. Shi, W. Shen, X. Dong, J. Feng, M. Ruan, and Y. Li: 'Stimuli-Responsive Controlled Drug Release from a Hollow Mesoporous Silica Sphere/Polyelectrolyte Multilayer Core-Shell Structure', *Angew. Chem.*, 2005, **117**(32), 5213–5217, doi: 10.1002/ange.200501500.

# Symbols and abbreviations

<i>a</i>	Lattice parameter
BET	Brunauer-Emmet-Teller
BJH	Barrett-Joyner-Halenda
COK-12	Centrum voor Oppervlaktechnie & Katalyse. Ordered mesoporous silica material.
<i>d</i>	d-spacing
DIW	Deionized water
EDX	Energy-dispersive X-ray spectroscopy
EISA	Evaporation-induced self-assembly
FDU-12	FuDan University. Ordered mesoporous silica material.
<i>g</i>	Packing parameter
GP-COK-12	Granular COK-12 produced by pressing of P- COK-12
ICP-OES	Inductively coupled plasma - optical emission spectroscopy
KIT-6	Korea Advanced Institute of Science and Technology. Ordered mesoporous silica material.
M41S	Family of molecular sieves of Mobil
MCF	Mesocelullar foam
MCM-41	Mobil Composition of Matter. Ordered mesoporous silica material.
MCM-48	Mobil Composition of Matter. Ordered mesoporous silica material.
M-COK-12	Monolithic COK-12
M-COK-12-25X	Monolithic COK-12 upscaled 25 times
MLV	Multilamellar vesicular

NLDFT	Non-local density functional theory
OCM	Oxidative coupling of methane
OMS	Ordered mesoporous silica
P-COK-12	Powder COK-12
P-COK-12-25X	Powder COK-12 upscaled 25 times
PCSA	Partitioned cooperative self-assembly
PEO	Polyethylene oxide
PFD	Process flow diagram
POS	Position
PPG	Polypropylene glycol
PPO	Polypropylene oxide
Q	Flow rate
SAXRD	Small-angle X-ray diffraction
SAXS	Small-angle X-ray scattering
SBA-15	Santa Barbara Amorphous. Ordered mesoporous silica material.
SEM	Scanning electron microscopy
TEM	Transmission electron microscopy
TEOS	Tetraethyl orthosilicate
TIPB	1,3,5 triisopropylbenzene
TMB	1,3,5 trimethylbenzene
$V_H/V_L$	Volume of hydrophobic block/volume of hydrophilic block
XRD	X-ray diffraction

# List of figures

Figure 1.1 Illustrative cross-section of a porous solid <sup>1</sup> . For details see Table 1.1.....	2
Figure 1.2 True liquid crystal templating mechanism (a) and the cooperative self-assembly mechanism (b). In the true liquid templating mechanism, the formation of a mesophase occurs prior to the addition of silica due to a high concentration of the templating molecule. In cooperative self-assembly, the silica-surfactant interactions guide self-assembly even at low surfactant concentrations.....	6
Figure 1.3 Schematic of various block copolymer architectures. Red and blue blocks represent the hydrophobic and hydrophilic blocks. ....	13
Figure 1.4 General structure of Ploxamers. A hydrophobic polypropylene oxide (PPO) block (center) is flanked by two hydrophilic polyethylene oxide (PEO) blocks. Variations in the chain lengths of the PPO and PEO blocks give rise to different mesostructures upon self-assembly. ....	13
Figure 1.5 Adjustment of pore size of ordered mesoporous materials by adjusting the dimensions of the hydrophobic block through surfactant selection (top and middle) and by incorporation of micellar swelling agents (bottom) <sup>39</sup> . Reprinted with permission from M. Kruk: ‘Access to Ultralarge-Pore Ordered Mesoporous Materials through Selection of Surfactant/Swelling-Agent Micellar Templates’, <i>Acc. Chem. Res.</i> , 2012, <b>45</b> (10), 1678-1687. Copyright 2012 American Chemical Society. ....	17
Figure 1.6 Schematic representation of a cross-section of MCF mesostructure, with “ink-bottle” or cage-like pores consisting of large spherical cells connected by narrow windows. ....	19
Figure 1.7 Progression of the morphological transition in P123 materials swollen by 1,3,5-trimethylbenzene (“oil”) <sup>48</sup> . Increasing oil concentration produced enlargement of the pore size until the	

hexagonal mesostructure was lost and interconnected spherical micelles were formed. Reprinted with permission from J.S. Lettow, Y.J. Han, P. Schmidt-winkel, P. Yang, D. Zhao, G.D. Stucky, and J.Y. Ying: 'Hexagonal to Mesocellular Foam Phase Transition in Polymer-Templated Mesoporous Silicas', *Langmuir*, 2000, **16**(22), 8291-8295. Copyright 2000 American Chemical Society.....20

Figure 1.8 Schematic representation of a MLV pore mesostructure, consisting of concentric silica shells and voids in alternation. ....23

Figure 1.9 Schematic representation of the stages of formation of COK-12. (a) Silica species precipitate on the PEO blocks of the spherical P123 micelles which are in solution. (b) At a critical silica concentration, steric stabilization is lifted and (c,d) spherical micelles coalesce into cylinders that increase in size. (e) Further addition of silica species leads to the aggregation of the cylinders and eventually to the formation of a 2-dimensional hexagonally ordered mesostructure<sup>63</sup>. Reprinted with permission from J. Jammaer, T.S. van Erp, A. Aerts, C.E.A. Kirschhock, and J.A. Martens: 'Continuous Synthesis Process of Hexagonal Nanoplates of P6m Ordered Mesoporous Silica', *J. Am. Chem. Soc.*, 2011, **133**(34), 13737-13745. Copyright 2011 American Chemical Society. ....24

Figure 1.10 Simplified scheme of the OCM reaction<sup>77</sup>. ....30

Figure 2.1 Left: Constructive interference. Right: Bragg's law of diffraction, in which two radiation waves of identical wavelength interact with two atoms within a crystalline solid and are scattered. The lower beam traverses an extra length of  $2d\sin\theta$ . Constructive interference occurs when this length is equal to an integer multiple of the wavelength of the incident radiation..... 36

Figure 2.2 Types of adsorption isotherms as classified by IUPAC<sup>1</sup>. See text for details. ....38

Figure 2.3 Schematic representation of multilayer adsorption, pore condensation and hysteresis in a single pore <sup>99</sup> . (A) monolayer formation, (B) multilayer adsorption, (C-D) capillary condensation, (E) pore evaporation by a receding meniscus, (F) desorption. ....	39
Figure 2.4 Types of hysteresis loops as classified by IUPAC <sup>1</sup> . See text for details.....	40
Figure 2.5 Graphical representation of the BET equation. ....	42
Figure 3.1 SEM micrographs of as-calcined P-COK-12. P-COK-12 consists of agglomerates of hexagonal plate-like particles that range from 200 to 500 nm in size. ....	54
Figure 3.2 Left: SAXRD pattern of as-calcined P-COK-12-25X. Three peaks corresponding to $p6m$ hexagonal symmetry are indexed, indicating long-range ordering. Right: d-spacing, $d_{100}=8.39$ nm, $d_{110}=4.91$ nm and $d_{200}=4.32$ nm. ....	55
Figure 3.3 Schematic illustration of a 2D hexagonal $p6m$ symmetry for COK-12. The circles represent pores. The red lines correspond to the (100) family of planes. The lattice parameter $a$ corresponds to the distance between pore centers, and the interplanar spacing $d_{100}$ to the distance between the (100) family of planes. ....	56
Figure 3.4 TEM micrographs of as-calcined P-COK-12. The shape of the particles as well as long-range 2D hexagonal pore ordering can be seen in (a) and (b); (c) view from the top of the pores, (d) pore size (white, 5.0 nm) and wall thickness (yellow, 3.9nm), (e) pore size, lateral view of cylindrical mesopores, (f) distance between pores (9.8 nm). ...	58
Figure 3.5 Nitrogen adsorption-desorption isotherm for as-calcined P-COK-12 with microporosity region. The isotherm is a type IV with H1 hysteresis, characteristic of mesoporous materials.....	59

Figure 3.6 Pore size distribution of as-calcined P-COK-12 as determined by the NLDFT method, revealing a pore radius of 3.0 nm. Inlet: pore size distribution of micropores, with a 0.6 nm radius.....	59
Figure 3.7 Top: SAXRD pattern of as-calcined P-COK-12-25X. Three peaks corresponding to $p6m$ hexagonal symmetry are indexed. Patterns have been normalized to the (100) peak and shifted for comparison, P-COK-12 pattern is shown for comparison. Bottom: d-spacing, $d_{100}=8.39$ nm, $d_{110}=4.97$ nm, $d_{200}=4.32$ nm.....	61
Figure 3.8 TEM micrographs of as-calcined P-COK-12-25X at different magnifications. The shape of the particles as well as long-range 2D hexagonal pore ordering can be seen in (a), (b) view from the top of the pores, (c) pore size (green, 5.3 nm), wall thickness (yellow, 3.4nm) and distance between pores (white, 9.8 nm).....	62
Figure 3.9 Nitrogen adsorption-desorption isotherm for as-calcined P-COK-12-25X. The isotherm is a type IV with H1 hysteresis, characteristic of mesoporous materials. P-COK-12 isotherm is shown for comparison. ....	62
Figure 3.10 Pore size distribution of as-calcined P-COK-12-25X as determined by the NLDFT method, revealing a pore radius of 3.3 nm. Pore size distribution of P-COK-12 is shown for comparison. Data shown in the relevant pore size range. ....	63
Figure 3.11 P-COK-12 slurry (left) and M-COK-12 gel (middle and right) after aging for 24 h.....	66
Figure 3.12 Macroscopic morphology of as-calcined P-COK-12 (left, fine powder) and as-calcined M-COK-12 (right, large hard irregular particles with a broad size distribution). ....	66
Figure 3.13 SEM micrographs of as-calcined M-COK-12 reveal the rod-like morphology of particles up to 2.5 $\mu$ m in length. ....	67

Figure 3.14 Top: SAXRD patterns of as-calcined M-COK-12 and M-COK-12-25X. Three peaks corresponding to $p6m$ hexagonal symmetry are indexed. Patterns have been normalized to the (100) peak and shifted for comparison, Bottom: d-spacing for M-COK-12 $d_{100}=8.23$ nm, $d_{110}=5.06$ nm, $d_{200}=4.43$ nm; for M-COK-12-25X $d_{100}=7.52$ nm, $d_{110}=4.83$ nm, $d_{200}=4.17$ nm.....	68
Figure 3.15 (a) TEM of as-calcined M-COK-12. Pore diameter, wall thickness and distance between pore centers are 6.5, 3.8 and 10.3 nm respectively (b) TEM of as-calcined M-COK-12-25X. Pore diameter, wall thickness and distance between pore centers are 5.1, 3.1 and 8.2 nm, respectively.....	69
Figure 3.16 Nitrogen adsorption-desorption isotherms for as-calcined M-COK-12 and M-COK-12-25X. The isotherms are type IV with H1 hysteresis, characteristic of mesoporous materials. P-COK-12 isotherm is shown for comparison.....	70
Figure 3.17 Detail of micropore region of nitrogen adsorption-desorption isotherm of as-calcined M-COK-12. P-COK-12 isotherm is shown for comparison. A loss in microporosity is observed evidenced by a lower uptake of nitrogen in the low relative pressure range.....	71
Figure 3.18 Pore size distribution of as-calcined M-COK-12 as determined by the NLDFT method, revealing a pore radius of 3.3 nm.....	71
Figure 3.19 SEM micrographs of as-pressed GP-COK-12. Breakage of hexagonal P-COK-12 particles occurs due to pressing (a-2). .....	75
Figure 3.20 Left: SAXRD pattern of as-pressed GP-COK-12. Three peaks corresponding to $p6m$ hexagonal symmetry are indexed. Patterns have been normalized to the (100) peak and shifted for comparison, P-COK-12 pattern is shown for comparison. Right: d-spacing $d_{100}=8.70$ nm, $d_{110}=5.1$ nm, $d_{200}=4.32$ nm.....	76

Figure 3.21 TEM micrographs of as-pressed GP-COK-12 showing (a) ordered (top arrow) and disordered (bottom arrow) regions, (b) ordered region (c) loss of ordering due to pressing. ....	77
Figure 3.22 Nitrogen adsorption-desorption isotherm of as-pressed GP-COK-12. The isotherm is a type IV with H1 hysteresis, characteristic of mesoporous materials. ....	78
Figure 3.23 Pore size distribution of as-pressed GP-COK-12 as determined by the NLDFT method, revealing a pore radius of 3.3 nm. Data shown in the relevant pore size range.....	78
Figure 3.24 SEM micrographs of fresh catalysts: (a) P-CAT, (b) G-CAT, (c) GP-CAT, (d) Silica-CAT. There is an increase in the amount of large crystallites on the surface of Silica-CAT, which have been identified as the Mn <sub>2</sub> O <sub>3</sub> phase. ....	80
Figure 3.25 Elemental mapping on fresh catalyst surface by energy-dispersive X-ray spectroscopy (atomic percentage), Na (pink), W (green), Mn (red). Bar represents 10 μm. ....	81
Figure 3.26 XRD patterns of fresh catalysts. The main phase in all catalysts is cristobalite, which appears as a result of phase transformation from amorphous silica due to the presence of sodium ions which decrease the phase transformation temperature. For all catalysts except M-CAT, sodium tungstate was identified as the main Na-W phase. In the case of M-CAT, sodium is present in the form of sodium manganese oxide, while tungstate appears as tungsten trioxide. Manganese also appears in the form of bixbyite (or braunite) for all catalysts. Patterns have been normalized to the cristobalite peak for comparison.....	83
Figure 3.27 Nitrogen adsorption-desorption isotherms of fresh catalysts. A loss of surface area due to the collapse of the mesostructure of the support is observed.....	84

Figure 3.28 SEM micrographs of used catalysts after 15 hours and up to 775°C on stream: (a) P-CAT, (b) G-CAT, (c) GP-CAT, (d) Silica-CAT. Catalyst particles are mixed with quartz sand as a diluting agent (background in a, b and c)..... 86

Figure 3.29 Elemental mapping on used catalyst surface after 15 hours and up to 775°C on stream by energy-dispersive X-ray spectroscopy (atomic percentage), Na (pink), W (green), Mn (red). Agglomeration of catalytic elements on the catalyst surface as a consequence of melting during OCM occurs. For P-CAT: bar corresponds to 5 µm. For G-CAT, GP-CAT and Silica-CAT: bar corresponds to 10 µm. .... 87

Figure 3.30 XRD patterns of used P-CAT after 15 hours and up to 775°C on stream. Manganese tungsten oxide appears as a new phase and a sodium phase cannot be identified, probably due to diffusion of sodium ions to the different silica matrices (dilutant, reactor and bulk catalyst). An intense quartz peak corresponding to the dilutant with a preferred orientation can be observed. .... 88

Figure 3.31 Conversion and selectivity to C<sub>2</sub> products of Silica-CAT, P-CAT, GP-CAT and G-CAT. An increase of 25°C is carried out each 5h. CH<sub>4</sub>:N<sub>2</sub>:O<sub>2</sub> ratio was 4:4:1 with a flow rate of 60 ml/min..... 91

Figure 3.32 Conversion of methane and total selectivity to C<sub>2</sub> products at lower reaction temperature. CH<sub>4</sub>:N<sub>2</sub>:O<sub>2</sub> ratio was fixed at 85:10:5 with a flow rate of 60 ml/min without dilution of the catalyst bed. Conversion of methane occurs at temperatures as low as 550°C for M-CAT..... 93

Figure 3.33 Conversion of methane and total selectivity to C<sub>2</sub> products at prolonged time on stream. Reaction carried out at 750°C with a CH<sub>4</sub>:N<sub>2</sub>:O<sub>2</sub> ratio of 4:4:1 and 60 ml/min flow rate without dilution of the catalyst bed. Deactivation of the catalysts after prolonged time on stream is observed. .... 94

Figure 4.1 SEM micrographs of selected as-calcined MCF-COK-12. (a) MCF-COK-12-2.0 (*p6m* mesostructure). (b) MCF-COK-12-4.0 (MCF morphology). Little difference is observed between (a) and (b), despite the difference in mesostructure. .... 101

Figure 4.2 Top: SAXRD pattern of as-calcined MCF-COK-12. Patterns have been normalized to the (100) peak and shifted for comparison. With increasing hexane concentration, a shift of the (100) peak to lower  $2\theta$  values is observed. Bottom: d-spacing (shown for the (100) family of planes). See Table 4.3 for more information. .... 102

Figure 4.3 TEM micrographs of as-calcined MCF-COK-12. (a) Standard P-COK-12, (b) MCF-COK-12-2.0 and (c) MCF-COK-12-5.4. An increase in the pore size accompanied by a decrease in ordering is observed. .... 104

Figure 4.4 Nitrogen adsorption-desorption isotherms of as-calcined MCF-COK-12. The isotherms are type IV with H1 hysteresis until a shift to H2 hysteresis is observed for MCF-COK-12-4.0. Type H2 hysteresis is associated to materials with “ink-bottle” pores. .... 105

Figure 4.5 Pore (samples with H1 hysteresis) and Cell size distribution (samples with H2 hysteresis) of as-calcined MCF-COK-12 as determined by the NLDFT method. .... 106

Figure 4.6 Window size distribution of as-calcined MCF-COK-12 (samples with H2 hysteresis) as determined by the NLDFT method. Data is shown for the relevant size range. .... 106

Figure 4.7 SEM micrographs of as-calcined MLV-COK-12: (a,b) MLV-COK-12-0.10: lowest PPG concentration, morphology identical to P-COK-12. (c,d) MLV-COK-12-2.50: highest PPG concentration, collapsed spheres. .... 111

Figure 4.8 Top: SAXRD pattern of as-calcined MLV-COK-12. Patterns have been normalized to the (100) peak and shifted for comparison. P-

COK-12 pattern is shown for comparison. At the highest PPG concentration, long-range ordering is lost. Bottom: d-spacing (shown for the (100) family of planes). See Table 4.4 for more information.. 112

Figure 4.9 TEM micrographs with pore detail of as-calcined MLV-COK-12. (a) Standard P-COK-12 (b) MLV-COK-12-0.10 (c) MLV-COK-12-0.25 (d) MLV-COK-12-0.50 (e) MLV-COK-12-0.75 (f) MLV-COK-12-1.00 (g) MLV-COK-12-1.50 (h) MLV-COK-12-2.50. Bar represents 50 nm..... 114

Figure 4.10 Nitrogen adsorption-desorption isotherms of as-calcined MLV-COK-12. The isotherms are type IV with H1 hysteresis until a shift to H2 hysteresis is observed for MLV-COK-12-0.50. P-COK-12 isotherm is shown for comparison. .... 115

Figure 4.11 Pore size distribution of as-calcined MLV-COK-12 as determined by the NLDFT method. Solid line represents pore size distribution. Dashed line represents cumulative pore volume. A loss of mesoporosity was observed with increasing PPG concentration..... 116

Figure 4.12 Phase diagrams of PEO-PPO-PEO systems in aqueous solution. Left: P123 (PEO<sub>20</sub>PPO<sub>70</sub>PEO<sub>20</sub>) phase diagram. Right: L121 (PEO<sub>5</sub>PPO<sub>68</sub>PEO<sub>5</sub>) phase diagram. The appearance of a lamellar phase can be observed for L121<sup>130</sup>. Reprinted with permission from G. Wanka, H. Hoffmann, and W. Ulbricht: 'Phase Diagrams and Aggregation Behavior of Poly(oxyethylene)-Poly(oxypropylene)-Poly(oxyethylene) Triblock Copolymers in Aqueous Solutions', *Macromolecules*, 1994, **27**(15), 4145-4159. Copyright 1994 American Chemical Society..... 119

Figure 5.1 Conceptual process flow diagram for the continuous COK-12 production unit of the Chair of Advanced Ceramics at the Technische Universität Berlin. Precursor solution preparation takes place in vessels S-1 and S-2, solutions are pumped to the mixing point M-1 with rotary pumps P-1 and P-2. Flow rates are set by rotameters R-1 and R-2. After mixing, the COK-12 slurry is collected in vessel S-3.

After slurry collection, the batch processes of filtration, washing, drying and calcination take place. ....123

Figure 5.2 Equipment for the continuous synthesis of COK-12. (a) thermostat, (b) overview of the setup and pumps, (c) solution preparation vessel S-1 for sodium silicate solution, (d) solution preparation vessel S-2 for buffered P123 solution, (e) rotameters, (f) collection vessel.....125

Figure 5.3 Subsequent batch processes of continuous COK-12 synthesis. (a) vacuum filtration/washing, (b) drying in drying cabinet, (c) calcination in furnace.....125

Figure 5.4 Calibration curves of flow rate meters. ....129

Figure 5.5 Top: SAXRD pattern of as-calcined P-COK-12-CONT with variations in time of aging, with a  $Q_{P123}/Q_{sodasil}$  ratio of 2.8 and  $Q_{P123}$  of 72 ml/min. Three peaks corresponding to  $p6m$  hexagonal symmetry are observed. Patterns have been normalized to the (100) peak and shifted for comparison. Inlet: detail of second and third peaks (110) and (200). Bottom: d-spacing (shown for the (100) family of planes).....134

Figure 5.6 TEM micrographs of as-calcined P-COK-12-CONT with variations in time of aging (a) 0 h aging, (b) 1 h aging, (c) 6 h aging, (d) 24 h aging. The shape of the particles as well as long-range 2D hexagonal pore ordering can be seen. ....135

Figure 5.7 Nitrogen adsorption-desorption isotherms for as-calcined P-COK-12-CONT with variations in time of aging with a  $Q_{P123}/Q_{sodasil}$  ratio of 2.8 and  $Q_{P123}$  of 72 ml/min. The isotherms are type IV with H1 hysteresis, characteristic of mesoporous materials. P-COK-12 isotherm is shown for comparison. ....136

Figure 5.8 Pore size distribution of as-calcined P-COK-12-CONT with variations in time of aging with a  $Q_{P123}/Q_{sodasil}$  ratio of 2.8 and  $Q_{P123}$  of 72 ml/min as determined by the NLDFT method. Pore size

distribution of P-COK-12 is shown for comparison. Data is shown only for the relevant pore size range. .... 136

Figure 5.9 SAXRD pattern of as-calcined P-COK-12-CONT with variations in flow rate. Three peaks corresponding to  $p6m$  hexagonal symmetry are observed. Patterns have been normalized to the (100) peak and shifted for comparison. Inlet: detail of second and third peaks (110) and (200). Right: d-spacing (shown for the (100) family of planes). .... 138

Figure 5.10 TEM micrographs of as-calcined P-COK-12-CONT with varying flow rate. An increase in ordering is visible for the sample with the highest flow rate. (a) P-COK-12-CONT-20. (b) P-COK-12-CONT-40. .... 139

Figure 5.11 Nitrogen adsorption-desorption isotherms for as-calcined P-COK-12-CONT with variations in flow rate (flow rate of sodium silicate stream from 9.1 to 31.8 ml/min and of P123 stream from 25.2 to 83.0 ml/min). See Table 5.7 for flow rate details. The isotherms are type IV with H1 hysteresis, characteristic of mesoporous materials. P-COK-12 isotherm is shown for comparison. .... 140

Figure 5.12 Pore size distribution of as-calcined P-COK-12-CONT with variations in flow rate as determined by the NLDFT method. Pore size distribution of P-COK-12 is shown for comparison. Data is shown only for the relevant pore size. See Table 5.7 for flow rate details. ... 141

# List of tables

Table 1.1 Classification of pores according to the IUPAC.....	1
Table 1.2 Ordered mesoporous silica materials, mesostructure and surfactant used <sup>21</sup> .....	4
Table 1.3 Main synthesis routes for mesoporous materials with corresponding surfactants and main products <sup>24</sup> .....	7
Table 1.4 Mesoporous silica materials produced by incorporation of swelling agents.....	18
Table 3.1 Conditions for powder COK-12 materials synthesis.....	49
Table 3.2 Conditions for monolithic COK-12 materials synthesis.....	49
Table 3.3 Synthesis conditions for upscaled COK-12 materials synthesis.....	50
Table 3.4 COK-12 catalyst supports prepared for this study.....	51
Table 3.5 Catalysts prepared and tested throughout this study.....	52
Table 3.6 Properties of as-calcined P-COK-12 and P-COK-12-25X. Upscaling of the synthesis up to 25 times did not produce significant changes in the properties of the material.....	65
Table 3.7 Sodium content in relation to silica of P-COK-12 and M.COK-12 determined by ICP-OES.....	70
Table 3.8 Properties of as-calcined M-COK-12 and M-COK-12-25X presented in comparison to P-COK-12.....	72

Table 3.9 Properties of GP-COK-12. Pressing of P-COK-12 to produce GP-COK-12 results in a loss of mesoscale ordering, pore volume and surface area. ....	79
Table 3.10 Elemental composition of fresh catalysts determined by ICP-OES.....	82
Table 3.11 Specific surface area and density of fresh catalysts. ....	85
Table 3.12 Description of catalytic testing experiments and catalysts used for each experiment. ....	89
Table 3.13 Catalytic activity tests: maximum methane conversion and selectivity to C <sub>2</sub> products at 775°C after 15 h.....	92
Table 4.1 Conditions for MCF synthesis with hexane as a swelling agent.....	98
Table 4.2 Conditions for MLV synthesis with polypropylene glycol (PPG) as a swelling agent. ....	99
Table 4.3 Properties of as-calcined MCF-COK-12 synthesized using hexane as a micellar swelling agent.....	107
Table 4.4 Properties of as-calcined MLV-COK-12 synthesized using polypropylene glycol (PPG) as a micellar swelling agent.....	117
Table 5.1 Equipment and specifications for the continuous COK-12 production unit. ....	124
Table 5.2 Synthesis conditions for continuous COK-12 synthesis.....	126
Table 5.3 Experimental conditions for continuous COK-12 synthesis with varying aging time.....	127

Table 5.4 Estimated and real flow rate meter positions and flow rates of feed streams. ....	130
Table 5.5 Experimental conditions for continuous COK-12 synthesis with varying flow rate.....	131
Table 5.6 Properties of as-calcined P-COK-12-CONT with variations in time of aging.....	137
Table 5.7 Properties of as-calcined P-COK-12-CONT with variations in flow rate. ....	141



### **Ordered Mesoporous Silica COK-12: Mesoscale Tailoring, Upscaling, Continuous Synthesis and Application in the Oxidative Coupling of Methane**

Ordered mesoporous silica (OMS) materials have expanding applications in various fields of research. In comparison with the most widely known OMS, the synthesis of COK-12, which takes place at room temperature under mild conditions, is more time efficient, inexpensive and environmentally friendly, yielding a material analogous to the well-known SBA-15. This work encompasses investigations regarding the production of COK-12, in terms of upscaling of the synthesis and tailoring of the size and shape of its characteristic hexagonal pore structure by incorporation of micellar swelling agents. Furthermore, COK-12 was used as a support for the  $\text{Na}_2\text{WO}_4\text{-Mn/SiO}_2$  catalyst for the oxidative coupling of methane reaction, showing promising results comparable to the enhanced activity of the catalyst supported on the SBA-15. The advantage of using COK-12 over other OMS materials is that the facile nature of COK-12 synthesis makes it a viable candidate for industrial production of the  $\text{Na}_2\text{WO}_4\text{-Mn/SiO}_2$  catalyst.

ISBN 978-3-7983-2988-1 (print)

ISBN 978-3-7983-2989-8 (online)



ISBN 978-3-7983-2988-1

<http://verlag.tu-berlin.de>